Universität Stuttgart

Institut für Wasser- und Umweltsystemmodellierung

Mitteilungen

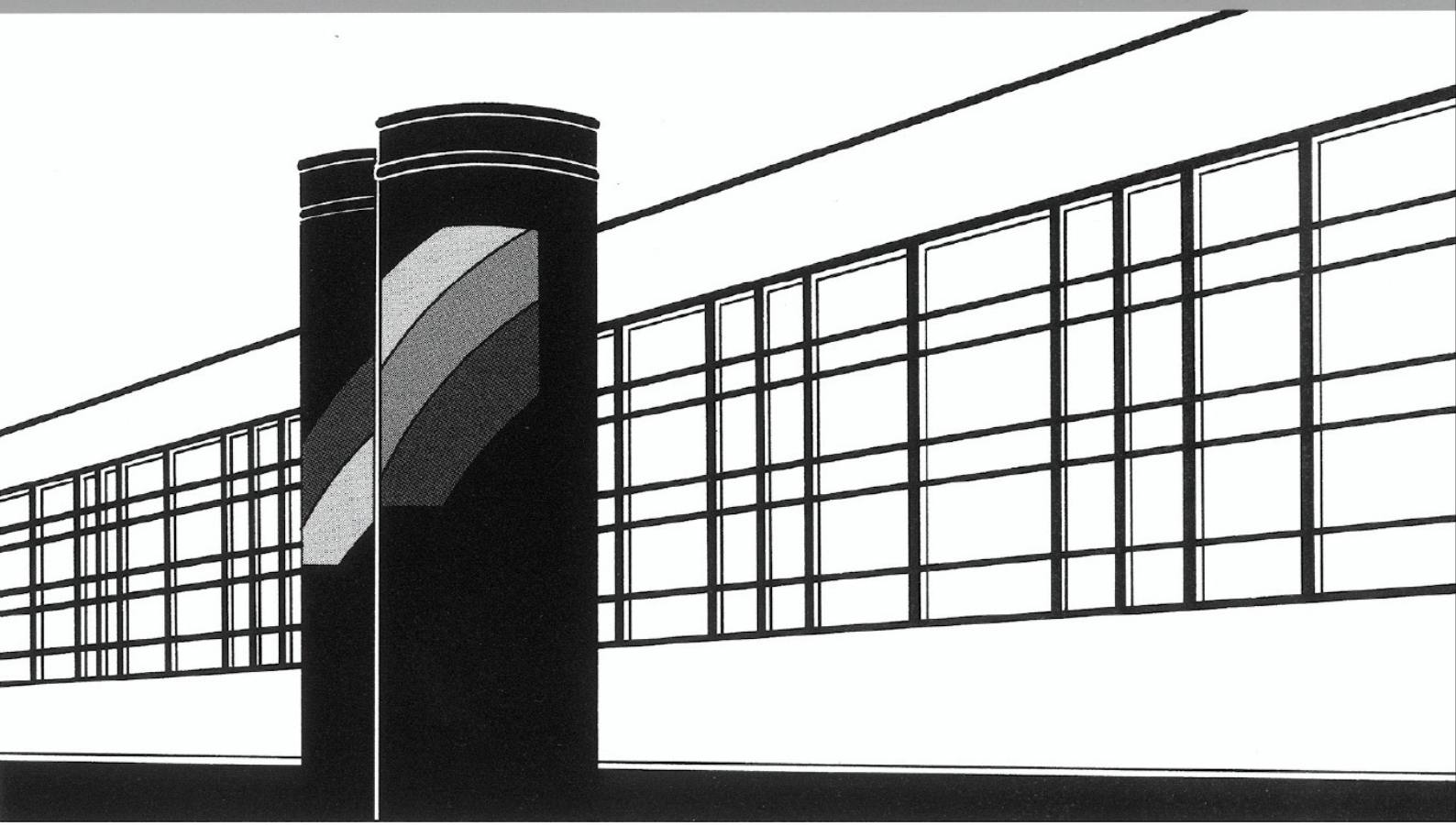

Heft 239 Nicolas Schwenck

An XFEM-Based Model for Fluid Flow in Fractured Porous Media

An XFEM-Based Model for Fluid Flow in Fractured Porous Media

von der Fakultät Bau- und Umweltingenieurwissenschaften der Universität Stuttgart
zur Erlangung der Würde eines
Doktor-Ingenieurs (Dr.-Ing.) genehmigte Abhandlung

vorgelegt von

Nicolas Schwenck

aus Hildesheim

Hauptberichter:	PD Dr. rer. nat. Bernd Flemisch, Universität Stuttgart
Mitberichter:	Prof. Dr. Scient. Inga Berre, Universitetet i Bergen
Mitberichter:	Prof. Dr.-Ing. Rainer Helmig, Universität Stuttgart

Tag der mündlichen Prüfung: 10. Februar 2015

Institut für Wasser- und Umweltsystemmodellierung der Universität Stuttgart

2015

Heft 239

An XFEM-Based Model for Fluid Flow in Fractured Porous Media

von
Dr.-Ing.
Nicolas Schwenck

Eigenverlag des Instituts für Wasser- und Umweltsystemmodellierung
der Universität Stuttgart

D93 An XFEM-Based Model for Fluid Flow in Fractured Porous Media

Bibliografische Information der Deutschen Nationalbibliothek
Die Deutsche Nationalbibliothek verzeichnet diese Publikation in der Deutschen Nationalbibliografie; detaillierte bibliografische Daten sind im Internet über http://www.d-nb.de abrufbar

Nicolas Schwenck:
An XFEM-Based Model for Fluid Flow in Fractured Porous Media, Universität Stuttgart. - Stuttgart: Institut für Wasser- und Umweltsystemmodellierung, 2015

(Mitteilungen Institut für Wasser- und Umweltsystemmodellierung, Universität Stuttgart: H. 239)
Zugl.: Stuttgart, Univ., Diss., 2015
ISBN 978-3-942036-43-6

NE: Institut für Wasser- und Umweltsystemmodellierung <Stuttgart>: Mitteilungen

Gegen Vervielfältigung und Übersetzung bestehen keine Einwände, es wird lediglich um Quellenangabe gebeten.

Herausgegeben 2015 vom Eigenverlag des Instituts für Wasser- und Umweltsystem-modellierung

Druck: Document Center S. Kästl, Ostfildern

Danksagung

Diese Arbeit enstand während meiner Zeit am LH^2 und wurde teilweise durch die IRTG NUPUS (DFG-finanziert) gefördert.

Thanks to the dissertation comittee members for agreeing to review my work. Bernd, vielen Dank für die Annahme als Dein erster Doktorand und die Betreuung. Ich konnte mich immer auf Dich als Ruhepol verlassen. Ich möchte Rainer danken, dass er NUPUS ins Leben gerufen hat. Durch NUPUS konnte ich an einer exzellenten Forschungs- und Ausbildungsumgebung teilhaben. Besonders bedanke ich mich bei Barbara, dass sie sich viel Zeit für die Betreuung genommen hat und durch konstruktive Kritik und den Druck, etwas wissenschaftlich Wertvolles zu leisten, charakterbildenden Einfluss ausübte.

Ein besonderer Dank gilt Steffen Müthing, der die DUNE-Module multidomaingrid und multidomain entwickelt hat und mir immer direkt weitergeholfen hat, wenn ich Fragen zu oder Probleme mit meiner Implementierung hatte.

Ich bedanke mich bei den Studenten, die einen Teil zu dieser Arbeit beigetragen haben: Tobias Meyer, Markus Köppel, Marwa Oueslati, William Crawford-Jones, und Katharina Türk, sowie den HiWis, die ich mir von Kollegen immer mal wieder für kurze Zeiträume ausleihen durfte.

Thanks a lot to Inga, Jan, Tor Harald and the other group members of the *Matematisk institutt, UoB* for a wonderful hospitality including a BBQ, a cooking night, hiking, a sailing trip and beer at the bus stop, but also the extraordinary supervision during my stay in Bergen; I really felt I was part of the group. Tusen takk!

Ein dickes Dankeschön geht auch an die Umweltschutztechniker-Gang für eine fantastische zweite Stuttgart-Hälfte und so viele neue Freundschaften; insbesondere aber an Philipp, Katherina und Benjamin für die Überzeugungsarbeit, am Tiefpunkt nicht hinzuschmeißen.

Vielen Dank Frau Lawday, für gemeinsame Sportabende, gemeinsames Feiern, egal ob Geburstage, Hochzeit oder Christbaum loben, aber auch ein immer helfendes und verlässliches Sekretariat zusammen mit Maria, die immer Zeit für Sonnenspaziergänge und ein offenes Ohr in Krisenzeiten hatte. Danke dafür.

I am very grateful for the working atmosphere in NUPUS and LH^2, which always was an essential part of my everyday work and kept me going.

„Zwerge auf den Schultern von Riesen“

Bernhard von Chartres

Contents

Abstract

Many fields of applications for porous media flow include geometrically anisotropic inclusions and strongly discontinuous material coefficients which differ in orders of magnitude. If the extension of those heterogeneities is small in normal direction compared to the tangential directions, e.g., long and thin, those features are called fractures. Examples which include such fractured porous-media systems in earth sciences include reservoir engineering, groundwater-resource management, carbon capture and storage (CCS), radioactive-waste reposition, coal bed methane migration in mines, geothermal engineering and hydraulic fracturing.

The analysis and prediction of flow in fractured porous-media systems is important for all the aforementioned applications. Experiments are usually too expensive and time consuming to satisfy the demand for fast but accurate decision making information. Many different conceptual and numerical models to treat fractured porous-media systems can be found in the literature. However, even in the time of large supercomputers with massive parallel computing power, the computational efficiency, and therefore the economic efficiency, plays a dominating role in the evaluation of simulation software.

In this thesis an efficient method to simulate flow in fractured porous media systems is presented. Darcy flow in fractures and matrix is assumed. The presented method is suited best for flow regimes depending on both, the fractures and the surrounding rock matrix and is able to account for highly conductive but also almost impermeable fractures with respect to the surrounding matrix.

The newly developed method is based on a co-dimension one conceptual model for the fracture network which is embedded in the surrounding matrix. The basis

for this model reduction is given in Martin et al. (2005). Numerically the fracture network is resolved by its own grid and coupled to the independent matrix grid. The discretization on this matrix grid allows jumps in the solution across the geometrical position of the fractures within elements by discontinuous basis functions. This discretization method is known as eXtended Finite Element Method (XFEM). A similar approach was simultaneously developed in D'Angelo and Scotti (2012).

The main novelty of this work is the extension of the aforementioned conceptual model, which only accounts for a single fracture ending on the boundary of the matrix domain, towards more complex fracture networks and suitable boundary conditions. This work can be structured into the development and implementation of three conceptual models (see 1–3 below) and their respective validation. It is followed by an evaluation of quality and efficiency with respect to established models (see 4 below). The implementation is carried out using DUNE, a toolbox for solving partial differential equations.

1. The first extension is the treatment of fractures, which end inside the domain. This includes the conceptual coupling at the fracture tips as well as the numerical treatment within the XFEM of the matrix elements, in which the fracture ends. The validation shows, that the proposed treatment is efficient and for most validation cases produces the desired accuracy.

2. In the second part, a conceptual model for intersecting fractures is developed and the implementation within the XFEM is presented. The validation shows that the proposed model and implementation can capture the complex physics of fracture crossings very accurately.

3. Of special interest are the boundary conditions for lower-dimensional fractures intersecting the matrix boundary. The established models very often use for simplicity constant values across lower-dimensional intersections. This is physically not always correct, because in reality lower-dimensional objects do not exist and if a gradient on the rock matrix boundary exists, there is also a gradient on the fracture boundary. Therefore, a sophisticated interpolation method is proposed. It is easy to apply because very often discrete measured

data is given to the model as input anyway and the proposed interpolation of values at the boundary is separated from the flow problem inside the domain. The concepts and results of the crossing model (2) and the boundary-condition interpolation (3) are published in Schwenck et al. (2014).

4. To show the performance of the newly developed model including the three major aspects mentioned above, it is compared against several established models and implementations within the simulation framework DuMu^{x}. The results of this comparison are published in Schwenck et al. (2015).

The model presented here combines the advantages of lower-dimensional models and non-matching grids while keeping the ability to represent the fracture geometry and its influence on the matrix flow field exactly. Therefore, it is an efficient alternative to established models.

Kurzfassung

Beispiele für poröse Medien sind ein Schwamm, menschliches Gewebe oder der Erdboden. Strömungen durch solche porösen Medien sind sehr stark beeinflusst durch die räumliche Struktur des jeweiligen porösen Mediums. Parameter, die diese Strukturen von einer volumengemittelten Perspektive aus beschreiben, können um mehrere Größenordnungen verschieden sein. Ist solch eine Struktur besonders dünn im Vergleich zu ihrer sonstigen Ausdehnung wird sie als Kluft bezeichnet. Anwendungsbeispiele solch geklüftet-porösen Medien im Bereich der Geowissenschaften sind Erdölförderung, Grundwassermanagement, CO_2-Speicherung, Atommülllagerung, Methanausbreitung in Kohleflözen, geothermische Energiegewinnung und Fracking.

Die Untersuchung von und die Vorhersage für Strömungen in porösen Medien ist bedeutend für all die oben genannten Beispielanwendungen. Experimente durch die vergleichbare Erkenntnisse gewonnen werden könnten sind in der Regel zu teuer oder dauern zu lange, so dass sie nicht immer herangezogen werden können um fundierte Entscheidungshilfen zu liefern. Es gibt viele verschiedene konzeptuelle und numerische Modelle, die sich mit der Simulation von geklüftet-porösen Medien beschäftigen. Obwohl die verfügbaren Computer immer effizienter werden und bessere Rechenleistung zur Verfügung stellen, dominiert die Effizienz bezüglich der Rechenzeit und damit die ökonomische Effizienz, die Entwicklung und den Einsatz fast aller Simulationsmodelle.

In dieser Arbeit wird solch ein effizientes Simulationsmodell, spezialisiert auf geklüftet-porösen Medien, vorgestellt. Vorausgesetzt wird Darcy-Strömung sowohl in den Klüften als auch in der umgebenden Matrix. Die hier vorgestellte Methode eignet sich am besten für Fälle, in denen das gesamte Strömungsbild weder von den

Klüften noch der Matrix dominiert ist, sondern beide einen bedeutenden Einfluss ausüben. Außerdem kann das hier vorgestellte Modell, im Gegensatz zu etablierten Modellen, sowohl sehr durchlässige als auch sehr undurchlässige Klüfte simulieren.

Das in dieser Arbeit entwickelte konzeptuelle Modell ist ein Modell für Klüfte, die eine Kodimension von eins zur sie umgebenden Matrix haben. Klüfte und Matrix sind voll gekoppelt. Der Teil der Dimensionsreduktion der Klüfte basiert auf der Arbeit von Martin et al. (2005). Das numerische Modell ist so ausgelegt, dass es unabhängige Gitter für Kluftnetzwerk und Matrix erlaubt. Eine Besonderheit des numerischen Modells für den Matrixanteil ist, dass es durch Einführen zusätzlicher Freiheitsgrade und unstetiger Basisfunktionen, Unstetigkeiten in der Lösung an den geometrischen Positionen von Klüften zulässt. Diese Methode wird eXtended Finite Element Method (XFEM) genannt. Ein ähnlicher Ansatz wurde zeitgleich zu dieser Arbeit in D'Angelo and Scotti (2012) entwickelt.

Der Hauptbeitrag dieser Arbeit ist die Erweiterung des oben genannten Modellkonzepts, welches nur am globalen Rand des Simulationsgebietes endende Einzelklüfte, berücksichtigt. Die Erweiterung beinhaltet komplexere Kluftnetzwerke und passende Randbedingungen. Sie lässt sich wie folgt gliedern: Entwicklung und Implementierung von drei konzeptuellen Modellen (siehe unten 1–3) und ihre Validierung (siehe unten 4), gefolgt von einer Bewertung der Qualität und Effizienz bezüglich vorhandener Modelle. Die Implementierung wurde mit Hilfe von DUNE umgesetzt. DUNE ist eine Programmierumgebung zum Lösen von partiellen Differentialgleichungen.

1. Die erste Erweiterung ist die Behandlung von Kluftenden. Sie beinhaltet die numerische Behandlung im Rahmen der XFEM, aber auch die Entwicklung eines konzeptuellen Models für die Strömung im Kluftende. Die Validierung zeigt, dass das vorgestellte Modell effizient ist und für die meisten Fälle die gewünschte Genauigkeit liefert.

2. Im zweiten Teil wird ein neues Modellkonzept für Kluftkreuzungen entwickelt und eine passende XFEM Implementierung vorgestellt. Auch hier zeigt die Validierung numerisch stabile Ergebnisse, die im niederdimensionalen Modell trotzdem die komplexe, equidimensionale Physik wiedergeben.

3. Ein weiterer Schwerpunkt liegt auf dem Umsetzen von physikalisch sinnvollen Randbedingungen für niederdimensionale geklüftet-poröse Medien bei nur wenig gegebenen Messwerten. Vorhandene Modelle benutzen sehr häufig am Rand konstante Werte oder kontinuierliche, lineare Interpolationen über niederdimensionale Klüfte hinweg. Dies ist physikalisch nicht immer korrekt, denn wenn ein Gradient am Rand der Matrix vorliegt, wirkt sich dieser auch am Rand der Kluft aus. In dieser Arbeit wird eine neue Möglichkeit zur Interpolation von Druckwerten am Rand vorgestellt, welche die Physik von Anwendungen besser wiederspiegelt. Außerdem ist diese Interpolation leicht in bestehende Modelle zu integrieren, da das das Problem am Rand separat vom Problem innerhalb des Gebietes gelöst werden kann. Die Konzepte und Ergebnisse des Kreuzungsmodells (2) und der Randbedingungsinterpolation (3) sind in Schwenck et al. (2014) veröffentlicht.

4. Um die gesamte Leistungsfähigkeit des neuen Modells mit seinen drei Teilen zu ermitteln, wird es anhand von verschiedenen Beispielen mit vorhandenen und etablierten Modellen aus dem Simulator DuMu$^{\text{x}}$ verglichen. Diese Ergebnisse sind in Schwenck et al. (2015) veröffentlicht.

Das hier vorgestellte Modell vereint die Vorteile von niederdimensionalen Kluftmodellen mit den Vorteilen von Modellen, die auf unabhängigen Gittern basieren. Es kann trotz der Modellreduktion den Einfluss komplizierte Kluftgeometrien auf die Strömung exakt abbilden und ist deshalb eine effiziente Alternative zu vorhanden Modellen.

1 Introduction

Flow through a porous medium such as a sponge, a tissue or the subsurface, is highly affected by the geometrical structure of the porous medium itself. The structural parameters often vary by several orders of magnitude over small distances. The scale of typical applications which are simulated is comparably large to the geometrical structure of the porous medium. Thus, these aspects bear complex challenges in developing efficient and consistent numerical models and simulation tools. Those models and tools should provide two competing features. On the one hand, they should capture important flow features which are influenced by the geometrical micro structure of the porous medium. On the other hand, they should not only be able to simulate large scale applications on high-end supercomputers but for example also on desktop computers in an engineering consulting company. The goal of this work is to develop such a simulation tool for single-phase flow in fractured porous-media systems.

Fractures are special heterogeneities which can represent extreme cases of highly varying structural parameters over a very short distance and are thus especially hard to treat conceptually and numerically. Several examples are given below, section 1.1. The first step to simulate real world problems is the development of a conceptual model. Due to the nature of fractures, structural parameters vary over a short distance, lower-dimensional models are often appropriate for their description. In this work, a mixed lower-/full-dimensional model for fractured porous-media systems is developed.

The second step towards a simulation tool, after a conceptual model was developed, is to apply a numerical model to the conceptual model. Grid based methods usually

need to resolve the physical problem domain, i.e., the fractures, with the grid. This is computationally costly and the goal of this work is to develop a numerical model, which can be applied to the conceptual model, to simulate the physical problem without resolving the fractures with a grid. The numerical method applied in this work to achieve the grid independence is the eXtended Finite Element Method (XFEM).

1.1 Application Examples and Resulting Challenges

While the conceptual models are usually developed on a coarse scale, the often called Darcy-scale, cf. section 1.2, the scale of interest for the simulation engineer can vary significantly between different applications. In the following, an overview of applications which involve fractured porous media, is given.

Fractured porous-media systems appear in many fields of application in earth science. Examples include groundwater-resource management (Qian et al. 2014), radioactive-waste reposition (Rechard et al. 2014, Joyce et al. 2014), coal bed methane migration in mines (Liu et al. 2011) or landslides (Dogan et al. 2009), and geothermal engineering (Fox et al. 2013). The recent development of new production techniques for oil leads to a combined application field in the context of reservoir engineering, CO_2-enhanced oil recovery (Torabi et al. 2012). Another example of a combined application field can be found in the context of carbon capture and storage (CCS), where CO_2 is used to replace the brine in geothermal systems and enhance the energy recovery, (Borgia et al. 2012). This approach, however, has not yet been tested in the field.

The concept of fractured porous media can also be applied to biomedical-engineering applications, e.g., flow and transport in the capillary bed (Erbertseder et al. 2012), where capillaries can be treated as fractures in the matrix, the surrounding tissue. Also technical applications are of interest, e.g., PEM fuel cells (Acosta et al. 2006), where the gas channels can be treated as fractures in the surrounding porous gas diffusion layers. In contrast to the aforementioned earth science applications where

the fractures are co-dimension one objects, the fuel cell and capillary models in most cases require co-dimension two approaches.

This work focuses on subsurface applications and the following parameter values are always related to such applications. A more detailed description of fractured porous-media systems in earth science can be found in (Dietrich et al. 2005, Berkowitz 2002, Bear et al. 1993). Typical field scales or simulation sizes of interest can range from tenths of meters to kilometers. REVs can usually be found in the range of centimeters to meters. In these cases fractures with a length shorter than one meter and a corresponding aperture of micrometers to millimeters are upscaled and fractures longer than one meter with an aperture of up to centimeters are treated discretely. An overview of relevant and often occurring sets of fracture sizes and matrix permeabilities is given for example in Belayneh et al. (2006).

Another key aspect for the transition from model concepts (fine and coarse-scale) towards a scale for the size of actual problems (field scale) is that, in most cases, the exact geometrical structure on a scale larger than the Darcy scale is unknown. It is usually approximated by taking small samples of the subsurface structure at specific probing sites. This can be done by analyzing cores or bore-hole images or by doing seismic surveys over a larger scale and then estimating the geometrical field scale structure. Because of the resulting uncertainty, stochastic modeling (Assteerawatt 2008), should be taken into account.

Altogether, the size of the problems and the uncertainty in parameters leads to the necessity of efficient computational simulation tools to be able to understand and possibly predict the solution of applications specific flow behavior in fractured porous media systems.

1.2 Porous Media Flow

In this section, the fundamental definitions for porous media flows are presented. A porous medium consists of a solid phase and arbitrarily distributed void space, also called pore space. Flow can only occur in the pore space. In the following,

only stationary flow for incompressible Newtonian fluids without gravity effects is considered. The solid phase is assumed to be rigid, i.e., it does not change over time. Flow models on the pore scale usually use the Navier-Stokes equations as basis. The scale of interest for the applications relevant to this work is that large, that there exists not enough computational power to solve the pore-scale problem directly. Moreover, the pore-scale geometry is usually unknown. To simplify the pore scale models, the idea of volume averaging can be used to derive models on a larger scale. This scale is based on Darcy's law and is therefore called Darcy scale. Darcy's law is named after Henry Darcy who postulated it after experiments in 1856 (Darcy 1856). Its main assumptions are slow, or creeping, flow where inertial forces can be neglected, and the existence of so-called representative elementary volumes, REVs.

Formally, several requirements have to be met for Darcy's law to be valid. A detailed derivation and overview is given in (Hubbert 1957). For this work, the most important requirement is the existence of a representative elementary volume (REV), which is for example defined in (Bear 1988, Süß 2005). To find an REV, pore-scale parameters are averaged over a volume, resulting in new, Darcy-scale parameters. If the averaging volume size is changed and the Darcy-scale parameters stay constant, the volume used for the averaging is called REV, figure 1.1. A property of the Darcy-scale parameters is, that they can vary in space but are constant within an REV. If an REV exists, the size of it is problem specific and bounded below and above, but nevertheless, within the boundaries, arbitrary.

Another important aspect for the validity of Darcy's law is the Reynolds number. The Reynolds number for porous media problems, $\mathrm{Re} = u_\mathrm{D}\, d/\nu$, is typically calculated with the grain size d as characteristic length, the Darcy velocity u_D as characteristic velocity and the characteristic kinematic viscosity ν. Darcy's law is applicable if the Reynolds number is well below one, e.g., (Nield and Bejan 2006).

Depending on the process, the fluid properties as well as the fluid velocity can differ by orders of magnitude; Examples include CCS with super-critical CO_2 or groundwater remediation with dense non-aqueous phase liquids (DNAPL). In addition, the order of magnitude of the soil properties varies strongly depending

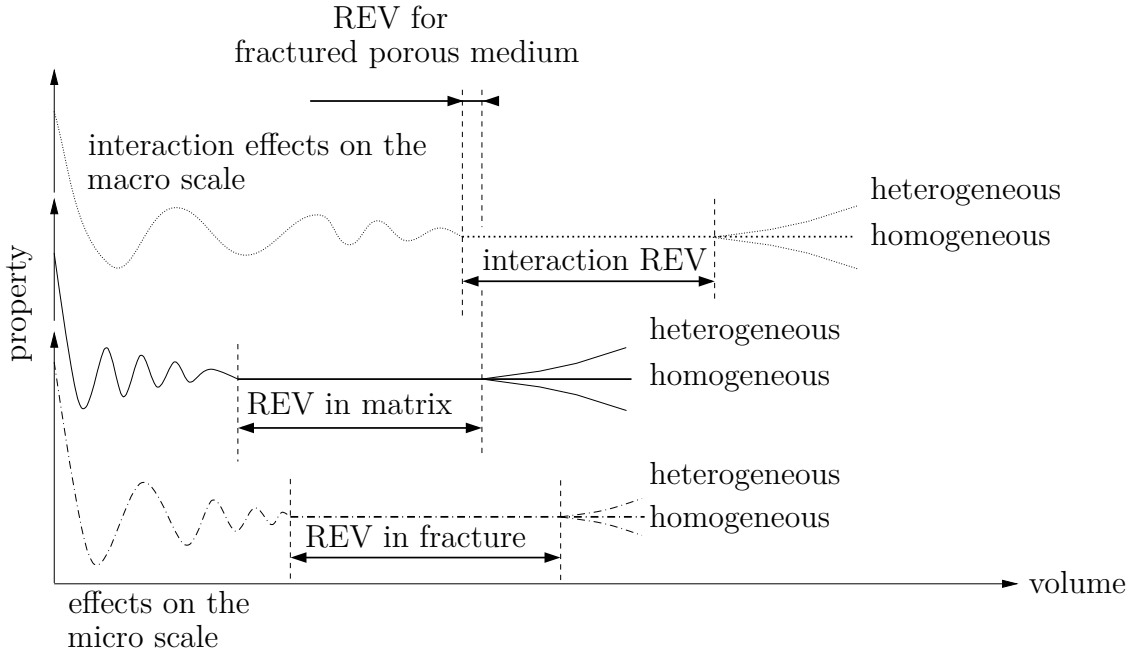

Figure 1.1: REV consideration bounds, modified after Assteerawatt (2008), Süß (2005), Bear (1988)

on the application. Examples of soil properties are grain size on the pore scale or intrinsic permeability on the Darcy scale. Those different characteristic quantities for different applications lead to the necessity to validate Darcy's law for every application and process.

Structural parameters do not only vary with respect to the problem, but can also vary in space on each scale for a single application. A region with a significant change of a parameter compared to its surroundings is called heterogeneity. Heterogeneities, where the characteristic length is significantly smaller than the REV size, are upscaled and averaged and thereby in the course of this work represented by the porous-medium (Darcy-scale) parameters porosity and permeability. The special case with the characteristic length of the heterogeneity in the order of the size of the REV or larger, is discussed in the following section.

1.3 Porous-Media Flow with Fractures

This section extends the fundamental definitions given in the previous section towards the special case of fractured porous media systems. Characteristic properties of fractured porous-media systems are geometrical anisotropic inclusions and strongly discontinuous material coefficients which can differ in orders of magnitude for the fractures and the matrix at the scale of interest.

The definition of a fracture in the course of this work is: If the transversal extension of a heterogeneity is very small in comparison to its lateral extension, this heterogeneity is called a fracture. Areas which are not fractures are called rock matrix. This simple geometrical definition leads to a new question: "What does small in one direction for a heterogeneity mean?". A threshold value, which determines whether a heterogeneity has to be treated as a fracture, can be defined. The choice of this threshold value is constrained, but within the constraints arbitrary. The constraint is, it must be guaranteed that the solution is independent of the choice of the threshold value. This is a decision for application specialists and one of the challenges in simulating fractured porous media. In this work, there is no absolute rule presented at what size a heterogeneity's normal extension is small enough for it to be treated as lower-dimensional fracture. However, in the presented examples the co-dimension one model solutions are compared against equidimensional reference solutions. From those examples, a rough estimate can be found to answer the initial question.

The definition for an REV is also affected if fractures can be found in the system. Fractures limit the REV size (Assteerawatt 2008), and they can even make it impossible to define REVs on specific scales. The existence of REVs must hold for averaging approaches. If fractures exist and no REV for an averaging approach can be found, a different concept is required. Averaging approaches do not only require REVs existent in the different domains but also on a usually larger scale, here called interaction scale. This scale considers for example fracture network geometry effects. The REV on this scale can easily be too large so that no common REV size for matrix, fracture and interaction and thus, the fractured porous medium, can be found, cf. figure 1.1. Treating the fractures individually, though, with REVs existent

for matrix and fractures separately, is another viable option and is used for the model presented here.

If a fracture has very different structural properties than its surroundings, especially much less solid phase and thus higher porosity, permeability and fluid velocity, a different conceptual model for the flow within the fracture should be chosen, e.g., solving a free flow problem based on (Navier-)Stokes equations. In most cases, however, this is computationally too costly and for the fractures also a simplified model is applied. One of those simplified and commonly used models is the Hele-Shaw model. Hele-Shaw flow is a velocity solution of the Navier-Stokes equations for laminar flow between parallel and (infinitely) close plates. To calculate the absolute discharge Q, integration in thickness direction y for a depth of ℓ_z gives the "cubic law" and can be used as an alternative to Darcy's law for fracture flow. Basically, it can be translated into a relation of the permeability, k_x, to the fracture width, d. In this work, Darcy's law is used because of its greater flexibility, i.e., the permeability can be chosen independently of the aperture.

Furthermore, in the course of this work, it is assumed that the geometrically defined fractures can either have significantly larger tangential permeabilities than the permeability of the matrix or can be almost impermeable, i.e., the matrix permeability is significantly larger than the fracture permeability. This definition differs from the geological definition of a fracture and is entirely based on the influence of the heterogeneities on the flow behavior instead of the geological definition. The geological definition is based on the strain effects where shear fractures are called faults and extension fractures are called joints (Bourbiaux et al. 2002). In this work such geo-mechanical rock history is not considered.

Depending on the fracture-matrix permeability ratios, fracture geometry, fracture density and fracture connectivity, different flow regimes can be identified (Matthäi and Belayneh 2004). Here, fracture density is a measure for the number of fractures in the control region and fracture connectivity a measure of how well the fractures are interconnected. The flow regime can be dominated by flow through fractures, or by flow through the matrix or it can depend on both. In this work the focus is on systems which are neither dominated by the fractures nor the matrix, but

both regions show significant influence on the global and local flow regimes and the fracture density is sparse such that averaging approaches are not possible.

The connection between the conceptual model and the simulation tool is the numerical method or discretization. After fundamental definitions for porous media flow in general and fractured porous media flow as a special case have been given, it is obvious that the REV size affects the discretization or the grid. The cell or element size should be chosen finer than the REV size, but the results are not to be interpreted on this fine scale, especially not near the boundaries, (Roth 2007). The fine grid scale can be used, though, to avoid numerical diffusion. Under the assumption of structural parameters being the same for each cell and that they vary over different REVs, the grid resolution should not be chosen larger than the REV size to avoid loss of input information. "This issue is of course not limited to the transition from the pore-scale to the continuum, but applies to all transitions between scales that involve some kind of averaging and also to measuring processes, where the measuring volume takes the role of the REV." (Roth 2007). This leads to different conceptual and numerical models for fractured porous media systems, which are presented in the following section.

1.4 Conceptual Fracture Models and Discretization

Fractured porous-media systems are complex to simulate and have been of great interest for modelers for a long time. Over the years, several different approaches have been developed with different priorities, each with their specific advantages and disadvantages. In the following, the three most important groups of conceptual models for fractured porous media systems with their respective advantages and disadvantages are presented. The numerical model has to be chosen appropriately to solve the problem defined by the conceptual model.

Discrete fractures

In discrete fracture approaches (DFM), the geometrical structure of the fractures, i.e., orientation and aperture, is discretely resolved within the conceptual model. In classical DFM models, the numerical model is chosen such that the fractures are also resolved by the grid. The fractures can be modeled with equidimensional discretization techniques (Gebauer et al. 2002), which require a huge number of degrees of freedom. Modeling the fractures as co-dimension one objects is an alternative approach (Hægland et al. 2009, Neunhäuserer 2003), but even with the reduction of degrees of freedom through lower-dimensional fractures, a very fine resolution of the matrix perpendicular to the fractures is necessary to get good solutions (Weatherill et al. 2008). This approach usually requires an expensive mesh-generation process which still cannot avoid extremely badly-shaped elements, thus, resulting in poor accuracy and possibly unphysical simulation results. In ongoing research, the discrete fracture approach is improved, e.g., (Basquet et al. 2005, Sandve et al. 2012) and also numerical models with non-matching grids are developed. The conceptual model in this thesis falls into the category of lower-dimensional DFM. The numerical model, however, allows independent grids for fractures and matrix.

Upscaling and multi-continua

Upscaling in this context means that new effective macro-scale parameters are determined. This macro scale is the scale of interest to the modeler. Those macro-scale parameters can be estimated through an engineering guess or by solving, sometimes simplified, fine-scale problems in subdomains. Those upscaling parameters are usually only determined once to improve the efficiency of the model. The fine scale solution is then averaged over the fracture-matrix system. The simplest approach assumes one macro-scale continuum, but also two coupled continua can be used to represent the different macro-scale parameters of fractures and matrix. Fractures can still occur with different characteristic lengths (Barthélémy 2009), but in those cases it is necessary to use multiple-interacting-continua models (MINC) (Pruess 1992, Karimi-Fard et al. 2006, Tatomir et al. 2011). For multiple-continua models, transfer functions between the interacting continua have to be determined. In recent research, general descriptions for such transfer functions were discovered (Schmid and Geiger 2012). All of those approaches demand the existence of REVs on the macro scale. Upscaling and multi-continua models are in most cases computationally cheaper than DFM models at the cost of loosing information of the solution on the fine scale. To represent the fine-scale properties best, the macro-scale parameters are often more complex than the fine-scale properties, e.g., a full anisotropic tensor permeability on the macro scale and a scalar permeability (varying in space) on the fine scale. This can lead to the necessity of more sophisticated numerical schemes. For example in the context of finite volume methods a TPFA method could be accurate enough on the fine scale, whereas an MPFA method on the macro scale would be appropriate.

Multi-scale

Although these methods are called multi-scale methods, most of them only use two scales, a coarse and a sub-grid scale. They are similar to upscaling techniques. The variational multi-scale method tries to capture small-scale effects on larger scales accurately and efficiently without actually resolving all the sub-grid-scale features

in detail (Hou and Wu 1997). This is achieved by finding new basis functions for the coarse scale through solving a sub-grid scale problem. In contrast to upscaling techniques, the solution of the fine-scale and the coarse-scale problems is usually carried out iteratively and repetitively over advancing simulation time. Therefore, dynamic effects can be better resolved with the multi-scale method at the cost of a higher computational effort. The theoretical framework of variational multi-scale methods is described, e.g., in (Hughes et al. 1998, Nordbotten 2009), while a more implementation-oriented discussion of a multi-scale finite-element method can be found in (Hou and Wu 1997). The multi-scale idea is also used within finite-volume approaches, e.g., (Jenny et al. 2005). Multi-scale finite-volume methods can also be seen in disguise of domain-decomposition preconditioners (Nordbotten and Bjørstad 2008). Regarding the numerical method, similar methods as for upscaling techniques are appropriate.

Summary of advantages and disadvantages

Discrete fracture models have the advantage of only requiring REVs for the fracture and the matrix regions separately. They do not need one single REV covering fractures and matrix. Therefore, DFMs can be used to create reference solutions. Those reference solutions can be used to determine if REVs can be found on scales which cover fracture and matrix regions. This information is important for different upscaling and multi-scale approaches. The combination of discrete fractures and a very fine mesh can in addition be used to produce reference solutions for other model concepts and numerical schemes to measure their accuracy. However, the computational costs are high due to meshing efforts and the large number of degrees of freedom. Keep in mind that unphysical results can be produced, if the mesh is not created carefully or the discretization method is chosen inappropriately.

Upscaling and multi-scale models require the existence of REVs on a coarser scale than it is necessary for DFMs. They are computationally less costly than discrete fracture models. Classical upscaling methods can be used if the fine-scale solution is not specifically of interest but only its influence on the coarse-scale solution.

1.5 Objectives of this Work

The exact geometrical structure of micro-scale fractures is often unknown. In this work, these fractures are therefore averaged and the REV size is chosen large enough in order to be incorporated into the coarse-scale porous medium parameters, (Bourbiaux et al. 2002). However, the flow regime can be significantly influenced by larger scale fractures which should be modeled and accounted for discretely, (Lee et al. 2001). If an REV does not exist, it is questionable to apply the previously discussed multi-scale and upscaling approaches. The discrete fracture models can be used, but even with large supercomputers with massive parallel computing power available, they are computationally, (Wu et al. 2002), and therefore economically costly. This necessitates a model in between those two conventional methods.

Therefore, the conceptual and numerical model developed in this thesis is intended to be used for fractured porous-media systems where the flow is neither dominated by highly conductive fractures nor blocking fractures but the flow regime really depends on the whole system and the fractures are significantly large such that averaging approaches cannot be applied. The main focus is on applications in earth science. In this work, only fractures of co-dimension one with respect to the surrounding matrix are considered and classical Darcy flow in both the matrix and the fractures is assumed.

The goal of this work is to develop a robust and flexible simulation tool for the aforementioned fully coupled fracture-network rock-matrix systems. This new approach does not require a matching of the matrix mesh with the discrete fracture network of co-dimension one. Thus, it is quite attractive for the numerical simulation of geometrically complex networks. The coupling of the matrix model and the fracture model is based on XFEM techniques.

Concepts to increase computational efficiency include simplification approaches, e.g., Vitel and Souche (2007), where a complex meshing is carried out and later the degrees of freedom are reduced; Tunc et al. (2012), where a highly permeable fracture is resolved as two interfaces, so that the neighboring matrices naturally can have non-matching grids at the fault. In contrast to those aforementioned

approaches, the approach presented in this thesis allows to handle an arbitrarily permeable fracture-network grid and a matrix grid independently, i.e., it is possible to use a finely resolved fracture network and a coarser discretized matrix or vice versa.

This work focuses on two main aspects. The first aspect is the development of the numerical method and the theoretical and mathematical analysis. The second focus of this work deals with the efficient implementation of the newly developed scheme. The implementation is based on the "Distributed and Unified Numerics Environment" (DUNE), (Bastian et al. 2008a,b), and integrated into the open-source porous-media simulator DuMu^{x}, (Flemisch et al. 2011).

The performance of a simulation tool has to be measured according to the envisioned use of the model. As a starting point, it is assumed that the partial differential equations being solved represent the physics correctly, i.e., the conceptual model is without error. The simulation tool approximates this conceptual model with the help of numerical methods. One measure of the simulation quality is therefore the error of the discrete solution with respect to the weak solution. From the application-oriented or engineering point of view, the main interest lies in the simulation of field scale problems. The appropriate measure is here, how well the simulation represents reality. In most earth-science applications, it is not easy and most often not even possible to do field-scale experiments, but it is possible to conduct laboratory scale experiments and use these results to validate the performance of the model. A third possibility is to compare the simulation tool, which comprises always a conceptual and a numerical model, against other well accepted conceptual and numerical models, which already have been compared to laboratory-scale experiments and measure the accuracy. Summarizing for all three measures, the performance of a simulation tool is better, the faster the simulation runs with the same accuracy. In this thesis the developed simulation tool is compared against well established conceptual and numerical models.

1.6 Structure of the Thesis

In chapter 2 of this thesis, the conceptual and numerical model for a single fracture ending on the boundary of the matrix domain and its implementation are presented. To begin with, the strong and the weak problem are shown. Then, the existence of a unique solution is proven, the discretization technique is introduced and implementation details are given. Finally, a dimensional analysis is presented. By means of two examples, a validation approach of the model concept and its implementation is carried out in chapter 3.

Chapters 4 to 6 present special cases of the simulation of lower-dimensional models: Fractures ending in the domain are discussed in chapter 4, intersecting fractures in chapter 5 and chapter 6 is about fractures intersecting the global boundaries. Chapters 5 and 6 are based on Schwenck et al. (2014).

Chapter 7 compares four different fracture models and implementations by means of several examples and discusses advantages and disadvantages of the individual approaches. This chapter is based on Schwenck et al. (2015). Finally, the thesis concludes with chapter 8: Summary, conclusion and outlook.

2 Model Concept – Development of a Reduced Model

The assumption of single-phase, incompressible flow in a porous medium leads to a model which comprises the continuity equation and Darcy's law on a bounded open domain $\Omega \subset \mathbb{R}^{\mathrm{n}}$; $\mathrm{n} = 2, 3$ and suitable boundary conditions. In general the presented model is valid for two and three dimensions. However, for the sake of simplicity, the theoretical framework is presented only for two-dimensional systems. Exceptions are specifically mentioned. In many cases the three-dimensional model is much harder to implement. Throughout this manuscript, dimensionless variables are used if not stated explicitly otherwise. A detailed dimensional analysis is given in section 2.6. The strong form of the problem is given by

$$\nabla \cdot \boldsymbol{u} = s \qquad \text{in } \Omega, \tag{2.1a}$$

$$\boldsymbol{u} = -\boldsymbol{K} \nabla p \qquad \text{in } \Omega. \tag{2.1b}$$

The velocity vector is denoted by $\boldsymbol{u}$ and p is the pressure. The permeability tensor $\boldsymbol{K}$ is assumed to be symmetric, positive definite. This leads to the elliptic pressure equation

$$\begin{aligned} \nabla \cdot (-\boldsymbol{K} \nabla p) &= 0 && \text{in } \Omega, \\ p &= \bar{p}^{\mathrm{D}} && \text{on } \partial\Omega^{\mathrm{D}}, \\ \boldsymbol{u} \cdot \boldsymbol{n} &= \bar{f}^{\mathrm{N}} && \text{on } \partial\Omega^{\mathrm{N}}. \end{aligned} \tag{2.2}$$

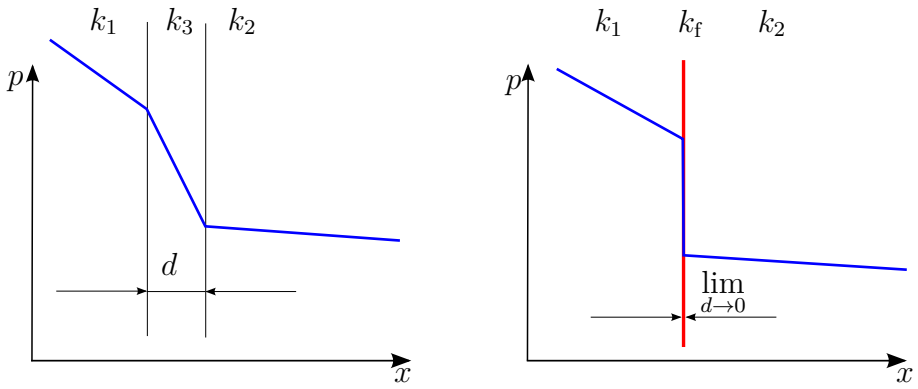

Figure 2.1: Equi and lower-dimensional pressure distribution in one dimension for different permeabilities

The unit outward normal vector is $\boldsymbol{n}$ and $\partial\Omega = \partial\Omega^{\mathrm{D}} \cup \partial\Omega^{\mathrm{N}}$ with $\partial\Omega^{\mathrm{D}} \cap \partial\Omega^{\mathrm{N}} = \emptyset$ is the boundary of the domain where Dirichlet values or Neumann fluxes are prescribed, respectively. The domain of interest contains heterogeneities, i.e., variations in the permeability tensor $\boldsymbol{K}$ over space.

If the heterogeneities are small in one direction, i.e., in two dimensions the ratio of normal extension to lateral extension tends to zero, they are called fractures and the model presented here can be applied. Heterogeneities which are not small in one direction are not excluded but are also not treated as fractures. Due to the assumption of fractures being small in one direction, the model does not resolve the fractures as equidimensional areas. Instead a limiting process is carried out, where the thickness is driven to zero. Thus, fractures are treated as objects of co-dimension one, $\gamma_j \subset \mathbb{R}^{\mathrm{n}-1}$, with respect to the surrounding matrix. Such a limiting process and therefore the basis for the weak equations presented here is for example carried out in Martin et al. (2005), Angot et al. (2009). For the special case of only highly conductive fractures it is presented for example in Alboin et al. (1999, 2002) and for Hele-Shaw flow in the fractures in Angot (2003).

Figure 2.1 shows as an example a one dimensional pressure distribution for an equidimensional and a lower-dimensional approach. In general, there can be full tensor permeabilities in the equidimensional model. In the lower-dimensional model, however, the fracture permeability, for example for a one dimensional fracture, is reduced to two scalar values, the normal permeability, $k_{\mathrm{f,n}}$, and the tangential

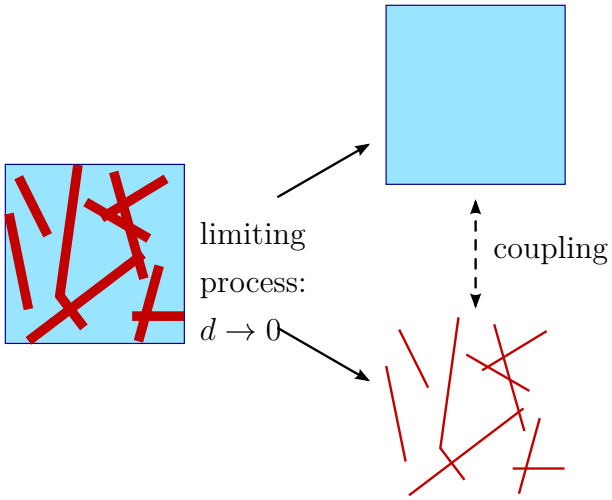

Figure 2.2: The fractured porous media system is decoupled into two subsystems, a lower dimensional fracture network and the remaining rock matrix.

permeability, $k_{\mathrm{f,t}}$. With the unit normal and tangential vectors, $\boldsymbol{n}, \boldsymbol{t}$, the fracture permeabilities of the co-dimension one model can be expressed as tensor in a fracture inherent coordinate system, namely,

$$\boldsymbol{K}_{\mathrm{f}} = \begin{pmatrix} k_{\mathrm{f,t}} & 0 \\ 0 & k_{\mathrm{f,n}} \end{pmatrix}_{\mathrm{f}} \quad \text{so that} \quad \boldsymbol{K}_{\mathrm{f}}\boldsymbol{t} \cdot \boldsymbol{t} = k_{\mathrm{f,t}}\,, \quad \boldsymbol{K}_{\mathrm{f}}\boldsymbol{n} \cdot \boldsymbol{n} = k_{\mathrm{f,n}}\,.$$

This, however, is a parameter constraint or can lead to a loss of information, cf. appendix B.2.

After the limiting process has been carried out, the fracture network is not only reduced by one dimension but also the complete system can be split into a part which only contains the rock matrix domain and another part which accounts for the fracture network, cf. figure 2.2. Both parts are coupled and the coupling conditions are a direct result of the limiting process.

Areas which have the same dimension as the world they live in, i.e., co-dimension zero, are always denoted with a capital Greek letter, co-dimension one areas are denoted with a small Greek letter. In the model presented here, the matrix domains are denoted by Ω for the equidimensional model and Ω_{m} in the lower-dimensional model, the fracture domain is denoted by Γ and γ, respectively.

2.1 Weak Formulation – Splitting and Coupling

For the sake of simplicity, we look at one single fracture which does not intersect itself and ends at the global boundary. In the equidimensional model the global domain is composed of three parts $\Omega = \Omega_1 \cup \Omega_2 \cup \Gamma$. For the lower-dimensional model the fracture divides our domain Ω into exactly two sub-domains, $\Omega_{\mathrm{m},1}$ and $\Omega_{\mathrm{m},2}$ such that $\Omega = \Omega_{\mathrm{m},1} \cup \Omega_{\mathrm{m},2}$ and $\bar{\Omega}_{\mathrm{m},1} \cap \bar{\Omega}_{\mathrm{m},2} = \gamma$, cf. figure 2.3.

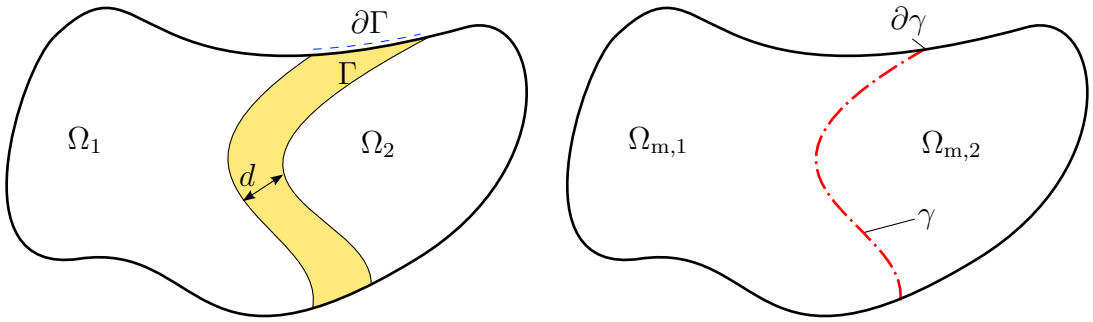

a equidimensional model domain

b mixed-dimensional model domain which includes a lower dimensional fracture

Figure 2.3: Model domains with fracture

In general, the fracture width/aperture, d, can vary along the fracture. In the model presented here, however, the aperture is assumed to be piecewise constant, i.e., $\partial d/\partial \boldsymbol{t} = 0$. That is a justified simplification, because the model input is also piecewise defined. Another option would be to interpolate the piecewise information from the model input and derive a new conceptual model which can handle such varying apertures.

The extension to multiple fractures is straightforward, as long as all fractures extend to the boundary of the computational domain and do not intersect each other. The special case of intersecting fractures is discussed in chapter 5 and fractures which end within the domain are discussed in chapter 4.

Starting with (2.1a) and (2.1b) for the single fracture system and requiring pressure and normal flux continuity at the equidimensional heterogeneity interfaces ($\bar{\Gamma} \cap \bar{\Omega}_i$)

following Martin et al. (2005), Angot et al. (2009), the strong problem formulation reads:

$$\nabla \cdot (\ \boldsymbol{u}_i\ ) = s_{\mathrm{m},i} \qquad \text{in } \Omega_{\mathrm{m},i}, \qquad i = 1,2, \tag{2.3a}$$

$$\boldsymbol{u}_i = -\boldsymbol{K}_i \nabla p_{\mathrm{m},i} \qquad \text{in } \Omega_{\mathrm{m},i}, \qquad i = 1,2, \tag{2.3b}$$

$$p_{\mathrm{m},i} = g \qquad \text{on } \partial\Omega_{\mathrm{m},i}\backslash\gamma, \qquad i = 1,2, \tag{2.3c}$$

$$-\zeta \boldsymbol{u}_i \cdot \boldsymbol{n}_i + \frac{2k_{\mathrm{f,n}}}{d} p_{\mathrm{m},i} = \frac{2k_{\mathrm{f,n}}}{d} p_{\mathrm{f}} - (1-\zeta)\boldsymbol{u}_{i+1} \cdot \boldsymbol{n}_{i+1} \qquad \text{on } \gamma, \qquad i = 1,2, \tag{2.3d}$$

$$\nabla_{\mathrm{t}} \cdot (\ \boldsymbol{u}_{\mathrm{f,t}}\ ) = s_{\mathrm{f}} + (\boldsymbol{u}_1 \cdot \boldsymbol{n}_1|_\gamma + \boldsymbol{u}_2 \cdot \boldsymbol{n}_2|_\gamma) \qquad \text{on } \gamma, \tag{2.3e}$$

$$\boldsymbol{u}_{\mathrm{f,t}} = -k_{\mathrm{f,t}}\, d\, \nabla_{\mathrm{t}}\, p_{\mathrm{f}} \qquad \text{on } \gamma, \tag{2.3f}$$

$$p_{\mathrm{f}} = g \qquad \text{on } \partial\gamma. \tag{2.3g}$$

The index in (2.3d) is always in $[1,2]$, i.e., for $i = 2$ is $\boldsymbol{u}_{i+1} = \boldsymbol{u}_1$. To close the system, appropriate boundary conditions for the matrix have to be applied on $\partial\Omega_{\mathrm{m},i}\backslash\gamma$ and for the fracture on $\partial\gamma$. Dirichlet boundary conditions, g, are exemplarily given in (2.3c) and (2.3g), cf. section 2.2.

The standard continuity equations and Darcy relations are given in (2.3a) and (2.3b) for the rock matrix and in (2.3e) and (2.3f) for the fracture. The continuity equation for the fracture (2.3e) contains an additional source/sink term to account for the exchange flow between matrix and fracture seen by the fracture.

In addition there are two coupling conditions, which can be seen as immersed boundary conditions for the rock matrix on the fracture-matrix interface, (2.3d). They give a relation between the fluxes normal to the fracture, the pressure gradient across the fracture and the average pressure in the fracture.

The algebraic identity together with the definition for a jump and an average is defined as

$$a_2 b_2 - a_1 b_1 = [\![\, a \,]\!]\{\!\{\, b \,\}\!\} + \{\!\{\, a \,\}\!\}[\![\, b \,]\!]$$

$$\text{with } [\![\, \cdot \,]\!] = (\,\cdot\,)_2 - (\,\cdot\,)_1$$

$$\text{and } \{\!\{\, \cdot \,\}\!\} = \frac{(\,\cdot\,)_1 + (\,\cdot\,)_2}{2}.$$

Applying the jump and average definition together with $\boldsymbol{n} = \boldsymbol{n}_1 = -\boldsymbol{n}_2$, i.e., the jump of fluxes is $[\![\, \boldsymbol{u} \cdot \boldsymbol{n} \,]\!] = -\boldsymbol{u}_2 \cdot \boldsymbol{n}_2|_\gamma - \boldsymbol{u}_1 \cdot \boldsymbol{n}_1|_\gamma$ and the average of fluxes is $\{\!\{\, \boldsymbol{u} \cdot \boldsymbol{n} \,\}\!\} = 0.5(\boldsymbol{u}_1 \cdot \boldsymbol{n}_1|_\gamma - \boldsymbol{u}_2 \cdot \boldsymbol{n}_2|_\gamma)$, for the pressures respectively $[\![\, p \,]\!] = p_2|_\gamma - p_1|_\gamma$ and $\{\!\{\, p \,\}\!\} = 0.5(p_1|_\gamma + p_2|_\gamma)$, (2.3d) gives:

$$(2\zeta - 1)[\![\, \boldsymbol{u} \cdot \boldsymbol{n} \,]\!] = \frac{4k_{\mathrm{f,n}}}{d} \left(p_{\mathrm{f}} - \{\!\{\, p \,\}\!\}\right), \qquad \text{on } \gamma, \tag{2.4a}$$

$$\{\!\{\, \boldsymbol{u} \cdot \boldsymbol{n} \,\}\!\} = -\frac{k_{\mathrm{f,n}}}{d} [\![\, p \,]\!], \qquad \text{on } \gamma. \tag{2.4b}$$

Remark 1. Following Martin et al. (2005), two equations to relate the matrix values to the fracture value are necessary (to close the system for each subdomain). The first is always $\{\!\{\, \boldsymbol{u} \cdot \boldsymbol{n} \,\}\!\} = k_{\mathrm{f,n}} \nabla p_{\mathrm{m}} \cdot \boldsymbol{n}$. The second depends on the physically based parameter ζ which is bounded $\zeta \in (0.5, 1.0]$. A $\zeta = 0.5$ represents the classical arithmetic mean, i.e., $p_{\mathrm{f}} = 0.5(p_{\mathrm{m}}|_{\gamma_1} + p_{\mathrm{m}}|_{\gamma_2})$. The other extreme, $\zeta = 1.0$, includes the gradient between averaged fracture and averaged matrix pressures in the mean, which is $k_{\mathrm{f,n}} \frac{p_{\mathrm{f}} - \{\!\{\, p_{\mathrm{m}} \,\}\!\}}{d/2} = \{\!\{\, \boldsymbol{u} \cdot \boldsymbol{n} \,\}\!\}$. The choice of ζ within its boundaries is arbitrary. In this work it is always set to one, because example test cases showed no significant differences, as long as you stay away from the lower limit 0.5. This is in contrast to Angot et al. (2009), cf. section 3.1.

By multiplying with the appropriate test function, cf. section 2.2, and integrating, the weak form starting from (2.3a) and (2.3e) is derived:

$$\begin{aligned}
&\sum_{i=1}^{2} \int_{\Omega_{\mathrm{m},i}} \nabla \cdot (\ \boldsymbol{u}_i\ )\, q_{\mathrm{m},i}\, \mathrm{d}\boldsymbol{x} \\
&\qquad = -\left(\boldsymbol{u}_1,\ \nabla q_{\mathrm{m},1}\right)_{\Omega_{\mathrm{m},1}} + \left(\boldsymbol{u}_1 \cdot \boldsymbol{n}_1,\ q_{\mathrm{m},1}|_\gamma\right)_\gamma + \left(\boldsymbol{u}_1 \cdot \boldsymbol{n}_1,\ q_{\mathrm{m},1}\right)_{\partial\Omega_{\mathrm{m},1}\setminus\gamma} \\
&\qquad\quad -\left(\boldsymbol{u}_2,\ \nabla q_{\mathrm{m},2}\right)_{\Omega_{\mathrm{m},2}} + \left(\boldsymbol{u}_2 \cdot \boldsymbol{n}_2,\ q_{\mathrm{m},2}|_\gamma\right)_\gamma + \left(\boldsymbol{u}_2 \cdot \boldsymbol{n}_2,\ q_{\mathrm{m},2}\right)_{\partial\Omega_{\mathrm{m},2}\setminus\gamma} \\
&\qquad = -\sum \left(\boldsymbol{u}_i,\ \nabla q_{\mathrm{m},i}\right)_{\Omega_{\mathrm{m},i}} + \underbrace{\sum \left(\boldsymbol{u}_i \cdot \boldsymbol{n}_i,\ q_{\mathrm{m},i}\right)_{\partial\Omega_{\mathrm{m},i}\setminus\gamma}}_{\text{global Neumann matrix b.c.}} \\
&\qquad\quad \underbrace{-\Big(\left(\llbracket\, \boldsymbol{u}\cdot\boldsymbol{n}\,\rrbracket, \{\!\{\, q_{\mathrm{m}}\,\}\!\}\right)_\gamma + \left(\{\!\{\, \boldsymbol{u}\cdot\boldsymbol{n}\,\}\!\}, \llbracket\, q_{\mathrm{m}}\,\rrbracket\right)_\gamma\Big)}_{\text{interface c.}}
\end{aligned} \tag{2.5a}$$

$$\begin{aligned}
&\int_\gamma \Big(\nabla_{\mathrm{t}} \cdot (\ \boldsymbol{u}_{\mathrm{f,t}}\ ) - \left(\boldsymbol{u}_1 \cdot \boldsymbol{n}_1|_\gamma + \boldsymbol{u}_2 \cdot \boldsymbol{n}_2|_\gamma\right)\Big) q_{\mathrm{f}}\, \mathrm{d}\boldsymbol{s} \\
&\qquad = -\left(\boldsymbol{u}_{\mathrm{f,t}},\ \nabla_{\mathrm{t}}\, q_{\mathrm{f}}\right)_\gamma + \underbrace{\left(\llbracket\, \boldsymbol{u}\cdot\boldsymbol{n}\,\rrbracket, q_{\mathrm{f}}\right)_\gamma}_{\text{interface c.}} + \underbrace{\left(\boldsymbol{u}_{\mathrm{f,t}} \cdot \boldsymbol{t}, q_{\mathrm{f}}\right)_{\partial\gamma}}_{\text{global Neumann fracture b.c.}}
\end{aligned} \tag{2.5b}$$

Remark 2. An integration over $\partial\gamma$ if Ω is 2d is not necessary, because that means γ is only 1d and its boundary a single point. Following the fundamental theorem of integral calculus, it is in this case sufficient to simply evaluate the integrand at that point.

Using now relations (2.4a) and (2.4b) to solve only for the pressure, cf. (2.2), and not aiming for a mixed finite element approach as in D'Angelo and Scotti (2012), the weak formulation for a Dirichlet problem, with the definition for $\mathcal{Q}_g$ from (2.7), is stated as:

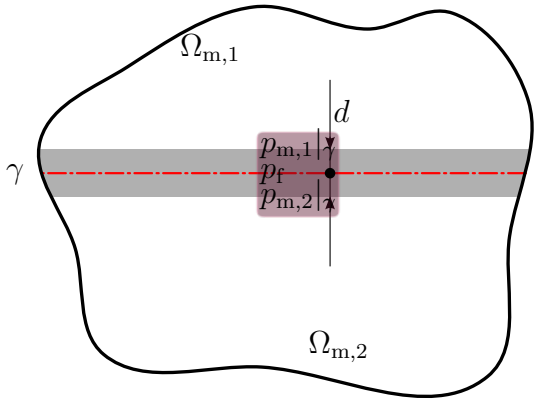

Figure 2.4: Domain decomposition with lower-dimensional fracture (dash-dotted line) and three pressure values and an aperture associated to every point on the fracture

Find $p = (p_{\mathrm{m},1}, p_{\mathrm{m},2}, p_{\mathrm{f}}) \in \mathcal{Q}_g$ such that

$$\sum_i (\boldsymbol{K}_{\mathrm{m},i} \nabla p_{\mathrm{m},i},\ \nabla q_{\mathrm{m},i})_{\Omega_{\mathrm{m},i}} - \sum_i (s_{\mathrm{m},i},\ q_{\mathrm{m},i})_{\Omega_{\mathrm{m},i}}$$
$$+ \left(\frac{4k_{\mathrm{f,n}}}{d} \{\!\{ p_{\mathrm{m}} \}\!\},\ \{\!\{ q_{\mathrm{m}} \}\!\} \right)_\gamma + \left(\frac{k_{\mathrm{f,n}}}{d} [\![p_{\mathrm{m}}]\!],\ [\![q_{\mathrm{m}}]\!] \right)_\gamma = \left(\frac{4k_{\mathrm{f,n}}}{d} p_{\mathrm{f}},\ \{\!\{ q_{\mathrm{m}} \}\!\} \right)_\gamma \tag{2.6a}$$
$$(k_{\mathrm{f,t}}\, d\, \nabla_{\mathrm{t}}\, p_{\mathrm{f}},\ \nabla_{\mathrm{t}}\, q_{\mathrm{f}})_\gamma - (s_{\mathrm{f}},\ q_{\mathrm{f}})_\gamma + \left(\frac{4k_{\mathrm{f,n}}}{d} p_{\mathrm{f}},\ q_{\mathrm{f}} \right)_\gamma = \left(\frac{4k_{\mathrm{f,n}}}{d} \{\!\{ p_{\mathrm{m}} \}\!\},\ q_{\mathrm{f}} \right)_\gamma \tag{2.6b}$$

for all test functions $q \in \mathcal{Q}_0$.

The weak equation for the fracture network is already written in the lower dimensional form, which is denoted by the subscript f, cf. appendix B, i.e., at each point on the fracture γ there are three pressure values in the model, cf. figure 2.4. The subscripts t, n denote the tangential and normal direction of the lower dimensional fracture respectively.

Introducing the porosity ϕ_i, $i = 1, 2, \mathrm{f}$ which can be globally heterogeneous but is assumed to be constant within each subdomain i, does not change the model presented here because the porosity is already included in the Darcy velocity. If an extension towards instationary flow is made the porosity appears in the storage term which does not affect the conceptual model presented here.

2.2 Existence of a Unique Solution: Boundedness and Coercivity

For the sake of simplicity, we show the existence of a unique solution only for the case of a single fracture which divides the domain in exactly two parts and intersects with the global boundary at exactly two points. The second condition, intersection with the global boundary, is only necessary because we want to look at the fracture and the matrix parts separately. Therefore we need also boundary conditions which are applied on the fracture domain. This proof can be easily extended towards several not connected fractures. Fracture crossings and (partially) immersed fractures however, have to be considered separately.

Following the Lax-Milgram theorem, we show boundedness and coercivity to proof the existence of a unique solution. For the split matrix domain, we introduce the Sobolev spaces as follows

$$\mathcal{H}^1_{g;\partial\Omega_{\mathrm{m},i}\setminus\gamma}(\Omega_{\mathrm{m},i}) \coloneqq \left\{ v_i \in \mathcal{H}^1(\Omega_{\mathrm{m},i}) : v_i|_{\partial\Omega_{\mathrm{m},i}\setminus\gamma} = g \right\}$$

so that we define the test functions q_{m} in a product space of the test spaces on each subdomain and the test functions q_{f} for the fracture, and the obvious meaning for $\mathcal{H}^1_g(\gamma)$, as

$$q_{\mathrm{m}} \in \mathcal{Q}_{g,\mathrm{m}} = \mathcal{H}^1_{g;\partial\Omega_{\mathrm{m},1}\setminus\gamma}(\Omega_{\mathrm{m},1}) \times \mathcal{H}^1_{g;\partial\Omega_{\mathrm{m},2}\setminus\gamma}(\Omega_{\mathrm{m},2}), \quad q_{\mathrm{f}} \in \mathcal{Q}_{g,\mathrm{f}} = \mathcal{H}^1_g(\gamma).$$

The complete space for a Dirichlet-problem then reads

$$\begin{aligned} q =& (q_{\mathrm{m}}, q_{\mathrm{f}}) \\ &\in \mathcal{Q}_g = \{ q = (q_{\mathrm{m},1}, q_{\mathrm{m},2}, q_{\mathrm{f}}) \in \mathcal{H}^1_{g;\partial\Omega_{\mathrm{m},1}\setminus\gamma}(\Omega_{\mathrm{m},1}) \times \mathcal{H}^1_{g;\partial\Omega_{\mathrm{m},2}\setminus\gamma}(\Omega_{\mathrm{m},2}) \times \mathcal{H}^1_g(\gamma) \}. \end{aligned} \tag{2.7}$$

It is equipped with a norm, which is for such a product space, as usual the square root of the sum of the squared norms

$$\|\cdot\|_{\mathcal{Q}} = \sqrt{\|\cdot\|_{\mathcal{Q}_\mathrm{m}}^2 + \|\cdot\|_{\mathcal{Q}_\mathrm{f}}^2}. \tag{2.8}$$

We assume for ease of notation homogeneous Dirichlet boundaries for all global boundaries (i.e., on $\partial\Omega$ which includes $\partial\gamma$). The extension towards Dirichlet-Neumann problems is straightforward if there exists at least a Dirichlet boundary part, i.e., $\partial\Omega^\mathrm{D} \neq \emptyset$, $\partial\gamma^\mathrm{D} \neq \emptyset$, otherwise the coercivity cannot be shown easily with the Poincaré-like inequality as in (2.17), cf. for example (Ern 2004, Evans 1998).

Inhomogeneous Dirichlet boundaries can be easily incorporated by reducing the problem to a homogeneous problem, i.e., extending g into Ω_m and γ, by substituting $\breve{p}_{\mathrm{m},i} = p_{\mathrm{m},i} - g|_{\partial\Omega^\mathrm{D}_{\mathrm{m},i}}$ and $\breve{p}_\mathrm{f} = p_\mathrm{f} - g|_{\partial\gamma^\mathrm{D}}$, assuming that such functions exist in $\mathcal{H}^1$ on their corresponding domain. That leads to changed source terms in (2.3a) and (2.3e), $\breve{s}_{\mathrm{m},i} = s_{\mathrm{m},i} - a_\mathrm{m}(g|_{\partial\Omega^\mathrm{D}_{\mathrm{m},i}}, q_{\mathrm{m},i})$ and $\breve{s}_\mathrm{f} = s_\mathrm{f} - a_\mathrm{f}(g|_{\partial\gamma^\mathrm{D}}, q_\mathrm{f})$. This is a widely used standard approach which can be found for example in Braess (2007). For ease of notation we restrict the following section to homogeneous Dirichlet boundary conditions and drop the subscript so that $\mathcal{Q} \equiv \mathcal{Q}_0$. Our homogeneous Dirichlet-problem bi-linear form $a = a_\mathrm{m} + a_\mathrm{f} - b_\mathrm{mf} - b_\mathrm{fm} : \mathcal{Q} \times \mathcal{Q} \to \mathbb{R}$ is given by:

$$\begin{aligned}
a_\mathrm{m}(p_\mathrm{m}, q_\mathrm{m}) &= \sum_i (\boldsymbol{K}_{\mathrm{m},i}\, \nabla\, p_{\mathrm{m},i},\, \nabla\, q_{\mathrm{m},i})_{\mathcal{L}^2(\Omega_{\mathrm{m},i})} \\
&\quad + \left(\frac{4k_{\mathrm{f,n}}}{d} \{\!\{\, p_\mathrm{m} \,\}\!\}, \{\!\{\, q_\mathrm{m} \,\}\!\}\right)_{\mathcal{L}^2(\gamma)} + \left(\frac{k_{\mathrm{f,n}}}{d} [\![\, p_\mathrm{m} \,]\!], [\![\, q_\mathrm{m} \,]\!]\right)_{\mathcal{L}^2(\gamma)}, && \text{(2.9a)} \\
a_\mathrm{f}(p_\mathrm{f}, q_\mathrm{f}) &= (k_{\mathrm{f,t}}\; d\, \nabla\, p_\mathrm{f},\, \nabla\, q_\mathrm{f})_{\mathcal{L}^2(\gamma)} + \left(\frac{4k_{\mathrm{f,n}}}{d} p_\mathrm{f}, q_\mathrm{f}\right)_{\mathcal{L}^2(\gamma)}, && \text{(2.9b)} \\
b_\mathrm{mf}(p_\mathrm{m}, q_\mathrm{f}) &= \left(\frac{4k_{\mathrm{f,n}}}{d} \{\!\{\, p_\mathrm{m} \,\}\!\}, q_\mathrm{f}\right)_{\mathcal{L}^2(\gamma)}, && \text{(2.9c)} \\
b_\mathrm{mf}(p_\mathrm{f}, q_\mathrm{m}) &= \left(\frac{4k_{\mathrm{f,n}}}{d} p_\mathrm{f}, \{\!\{\, q_\mathrm{m} \,\}\!\},\right)_{\mathcal{L}^2(\gamma)}. && \text{(2.9d)}
\end{aligned}$$

Boundedness There exists a constant dependent on problem specific physical parameters $\mathrm{c_b}(k_{\mathrm{f,t}}\,, k_{\mathrm{f,n}}\,, d, \boldsymbol{K}_{\mathrm{m}}, \Omega_{\mathrm{m},1}, \Omega_{\mathrm{m},2}, \gamma) > 0$, so that

$$\begin{aligned} |a(p,q)| &\leq |a_{\mathrm{m}}(p_{\mathrm{m}}, q_{\mathrm{m}})| + |a_{\mathrm{f}}(p_{\mathrm{f}}, q_{\mathrm{f}})| + |b_{\mathrm{mf}}(p_{\mathrm{m}}, q_{\mathrm{f}})| + |b_{\mathrm{fm}}(p_{\mathrm{f}}, q_{\mathrm{m}})| \\ &\leq \mathrm{c_b} \left\|p\right\|_{\mathcal{Q}} \left\|q\right\|_{\mathcal{Q}} \quad \forall p, q \in \mathcal{Q}. \end{aligned} \tag{2.10}$$

First, we show the boundedness separately for the matrix and the fracture and the coupling parts and then use the results in (2.10) to show the boundedness of the coupled system.

The fracture parameters are properly defined on γ and it is assumed that $k_{\mathrm{f,t}}\,, k_{\mathrm{f,n}}$ and d are in $\mathcal{L}^\infty(\gamma)$, i.e., for example at least elementwise continuous. The matrix permeability is assumed to be positive definite and also in $\mathcal{L}^\infty$ on $\Omega_{\mathrm{m},i}$, so that

$$\left\|\boldsymbol{K}_{\mathrm{m}}\right\|_{\mathcal{L}^\infty(\Omega_{\mathrm{m},i})} \;\geq\; \mathrm{c} \;>\; 0, \;\forall\, \boldsymbol{x} \;\in\; \Omega.$$

Before we look at the whole bilinear form of the matrix part (2.9), we find an estimate for the additional terms existing on the fracture. Using the triangle inequality and extending the estimate from the interface into the domains using the trace theorem, we get for the $\mathcal{L}^2$-norms of the average with the average defined as $\{\!\{\, p_{\mathrm{m}} \,\}\!\} = (\mathrm{tr}\, p_{\mathrm{m},1} + \mathrm{tr}\, p_{\mathrm{m},2})/2$ using the fact that $p_{\mathrm{m}} = 0$ on $\partial\Omega$ (and analogue the same for the jump):

$$\begin{aligned} \left\|\{\!\{\, p_{\mathrm{m}} \,\}\!\}\right\|_{\mathcal{L}^2(\gamma)} &\overset{\text{t.i.}}{\leq} \mathrm{c} \left(\left\| p_{\mathrm{m}}|_{\Omega_{\mathrm{m},1}} \right\|_{\mathcal{L}^2(\gamma)} + \left\| p_{\mathrm{m}}|_{\Omega_{\mathrm{m},2}} \right\|_{\mathcal{L}^2(\gamma)} \right) \\ &\overset{\text{t.t.}}{\leq} \mathrm{c} \left(\left\|p_{\mathrm{m}}\right\|_{\mathcal{H}^1(\Omega_{\mathrm{m},1})} + \left\|p_{\mathrm{m}}\right\|_{\mathcal{H}^1(\Omega_{\mathrm{m},2})} \right) \\ &\leq \mathrm{c} \left\|p_{\mathrm{m}}\right\|_{\mathcal{H}^1(\Omega_{\mathrm{m},1} \cup \Omega_{\mathrm{m},2})}. \end{aligned} \tag{2.11}$$

so that we can estimate the matrix bilinear form by using the Cauchy-Schwarz inequality as follows:

$$
\begin{aligned}
|a_{\mathrm{m}}(p_{\mathrm{m}}, q_{\mathrm{m}})| &\overset{\text{C.-S.}}{\leq} \sum_i \mathrm{c}\, \left(\|\boldsymbol{K}_{\mathrm{m}i}\|_{\mathcal{L}^\infty(\Omega_{\mathrm{m},i})} \,\|\nabla p_{\mathrm{m}i}\|_{\mathcal{L}^2(\Omega_{\mathrm{m},i})} \,\|\nabla q_{\mathrm{m}i}\|_{\mathcal{L}^2(\Omega_{\mathrm{m},i})} \right) \\
&\quad + \mathrm{c} \left\| \frac{4k_{\mathrm{f,n}}}{d} \right\|_{\mathcal{L}^\infty(\gamma)} \|\{\!\{ p_{\mathrm{m}} \}\!\}\|_{\mathcal{L}^2(\gamma)} \,\|\{\!\{ q_{\mathrm{m}} \}\!\}\|_{\mathcal{L}^2(\gamma)} \\
&\quad + \mathrm{c} \left\| \frac{k_{\mathrm{f,n}}}{d} \right\|_{\mathcal{L}^\infty(\gamma)} \|[\![p_{\mathrm{m}}]\!]\|_{\mathcal{L}^2(\gamma)} \,\|[\![q_{\mathrm{m}}]\!]\|_{\mathcal{L}^2(\gamma)} \\
&\overset{\text{t.t.}}{\leq} \sum_i \mathrm{c}\, \left(\|\boldsymbol{K}_{\mathrm{m},i}\|_{\mathcal{L}^\infty(\Omega_{\mathrm{m},i})} \,\|\nabla p_{\mathrm{m}i}\|_{\mathcal{L}^2(\Omega_{\mathrm{m},i})} \,\|\nabla q_{\mathrm{m}i}\|_{\mathcal{L}^2(\Omega_{\mathrm{m},i})} \right) \\
&\quad + \mathrm{c} \left\| \frac{5k_{\mathrm{f,n}}}{d} \right\|_{\mathcal{L}^\infty(\gamma)} \|p_{\mathrm{m}}\|_{\mathcal{H}^1(\Omega_{\mathrm{m},1}\cup\Omega_{\mathrm{m},2})} \,\|q_{\mathrm{m}}\|_{\mathcal{H}^1(\Omega_{\mathrm{m},1}\cup\Omega_{\mathrm{m},2})} \qquad (2.12) \\
&\leq \mathrm{c} \left\| \|\boldsymbol{K}_{\mathrm{m}}\|_{\mathcal{L}^\infty(\Omega_{\mathrm{m}})} + \frac{5\tilde{\mathrm{k}}_{\mathrm{f},\boldsymbol{n}}}{\tilde{d}} \right\|_{\mathcal{L}^\infty(\Omega)} \|p_{\mathrm{m}}\|_{\mathcal{H}^1(\Omega_{\mathrm{m},1}\cup\Omega_{\mathrm{m},2})} \,\|q_{\mathrm{m}}\|_{\mathcal{H}^1(\Omega_{\mathrm{m},1}\cup\Omega_{\mathrm{m},2})} .
\end{aligned}
$$

For the sake of simplicity $k_{\mathrm{f,n}}$ and d are extended in their definition into the whole parted domain $\Omega_{\mathrm{m},i}$ and marked with a superscript $\tilde{\cdot}$, so that the trace of the expanded parameters gives exactly the original parameters on γ.

$$
\operatorname{tr} \tilde{\mathrm{k}}_{\mathrm{f},\boldsymbol{n}}|_{\Omega_{\mathrm{m},i}}(\boldsymbol{x}) = k_{\mathrm{f,n}}(\boldsymbol{x}), \quad \operatorname{tr} \tilde{d}|_{\Omega_{\mathrm{m},i}}(\boldsymbol{x}) = d(\boldsymbol{x}) \qquad \forall \boldsymbol{x} \in \gamma
$$

The fracture part follows without any intermediate steps directly by using Cauchy-Schwarz's inequality again.

$$
\begin{aligned}
|a_{\mathrm{f}}(p_{\mathrm{f}}, q_{\mathrm{f}})| &\overset{\text{C.-S.}}{\leq} \mathrm{c}\, \|k_{\mathrm{f,t}}\, d\|_{\mathcal{L}^\infty(\gamma)} \,\|\nabla p_{\mathrm{f}}\|_{\mathcal{L}^2(\gamma)} \,\|\nabla q_{\mathrm{f}}\|_{\mathcal{L}^2(\gamma)} \\
&\quad + \mathrm{c} \left\| \frac{4k_{\mathrm{f,n}}}{d} \right\|_{\mathcal{L}^\infty(\gamma)} \|p_{\mathrm{f}}\|_{\mathcal{L}^2(\gamma)} \,\|q_{\mathrm{f}}\|_{\mathcal{L}^2(\gamma)} \\
&\leq \mathrm{c} \left\| k_{\mathrm{f,t}}\, d + \frac{4k_{\mathrm{f,n}}}{d} \right\|_{\mathcal{L}^\infty(\gamma)} \|p_{\mathrm{f}}\|_{\mathcal{H}^1(\gamma)} \,\|q_{\mathrm{f}}\|_{\mathcal{H}^1(\gamma)} \qquad (2.13)
\end{aligned}
$$

The coupling parts, analogously to the matrix part, can be estimated using the

Cauchy-Schwarz inequality and then applying the triangle inequality and using the trace theorem. With the definition of the norm, (2.8), it follows

$$
\begin{aligned}
&|b_{\mathrm{mf}}(p_{\mathrm{m}}, q_{\mathrm{f}})| + |b_{\mathrm{fm}}(p_{\mathrm{f}}, q_{\mathrm{m}})| \\
&\qquad \overset{\text{C.-S.}}{\leq} \quad \mathrm{c}\,\frac{4k_{\mathrm{f,n}}}{d}\left(\|\{\!\{\, p_{\mathrm{m}} \,\}\!\}\|_{\mathcal{L}^2(\gamma)}\,\|q_{\mathrm{f}}\|_{\mathcal{L}^2(\gamma)} + \|p_{\mathrm{f}}\|_{\mathcal{L}^2(\gamma)}\,\|\{\!\{\, q_{\mathrm{m}} \,\}\!\}\|_{\mathcal{L}^2(\gamma)}\right) \\
&\qquad \overset{(2.11),(2.13)}{\leq} \quad \mathrm{c}\,\frac{4k_{\mathrm{f,n}}}{d}\left(\|p_{\mathrm{m}}\|_{\mathcal{H}^1(\Omega_{\mathrm{m},1}\cup\Omega_{\mathrm{m},2})}\,\|q_{\mathrm{f}}\|_{\mathcal{H}^1(\gamma)} + \|p_{\mathrm{f}}\|_{\mathcal{H}^1(\gamma)}\,\|q_{\mathrm{m}}\|_{\mathcal{H}^1(\Omega_{\mathrm{m},1}\cup\Omega_{\mathrm{m},2})}\right) \\
&\qquad \overset{(2.8)}{\leq} \quad \mathrm{c}\,\|(p_{\mathrm{m}}, p_{\mathrm{f}})\|_{\mathcal{Q}}\,\|(q_{\mathrm{m}}, q_{\mathrm{f}})\|_{\mathcal{Q}}\,. \qquad (2.14)
\end{aligned}
$$

Coercivity There exists a constant dependent on problem-specific physical parameters
$\mathrm{c_c}(k_{\mathrm{f,t}}\,, k_{\mathrm{f,n}}\,, d, \boldsymbol{K}_{\mathrm{m}}, \Omega_{\mathrm{m},1}, \Omega_{\mathrm{m},2}, \gamma) > 0$, so that

$$
a(p,p) = a_{\mathrm{m}}(p_{\mathrm{m}}, p_{\mathrm{m}}) + a_{\mathrm{f}}(p_{\mathrm{f}}, p_{\mathrm{f}}) - 2b \geq \mathrm{c_c}\,\|p\|_{\mathcal{Q}}^2 \quad \forall p \in \mathcal{Q}. \qquad (2.15)
$$

For the coupling parts it is obvious that $b = b_{\mathrm{mf}}(p_{\mathrm{m}}, p_{\mathrm{f}}) = b_{\mathrm{fm}}(p_{\mathrm{f}}, p_{\mathrm{m}})$. Using Young's inequality this can be reformulated and then directly cancels out with one term in the matrix part and fracture part, respectively.

$$
-2b \overset{\text{Y.i.}}{\geq} -\left(\frac{4k_{\mathrm{f,n}}}{d}\{\!\{\, p_{\mathrm{m}} \,\}\!\}, \{\!\{\, p_{\mathrm{m}} \,\}\!\}\right)_{\mathcal{L}^2(\gamma)} - \left(\frac{4k_{\mathrm{f,n}}}{d}p_{\mathrm{f}}, p_{\mathrm{f}}\right)_{\mathcal{L}^2(\gamma)} \qquad (2.16)
$$

For the matrix we look again at first at the additional terms living on the fracture. They are always positive. For the lower estimate we can assume them to be zero if the standard Darcy part is always larger than zero.

$$
\left\|\frac{d}{4k_{\mathrm{f,n}}}\right\|_{\mathcal{L}^\infty(\gamma)}\|\{\!\{\, p_{\mathrm{m}} \,\}\!\}\|_{\mathcal{L}^2(\gamma)} \geq 0, \quad \left\|\frac{d}{k_{\mathrm{f,n}}}\right\|_{\mathcal{L}^\infty(\gamma)}\|[\![\, p_{\mathrm{m}} \,]\!]\|_{\mathcal{L}^2(\gamma)} \geq 0
$$

We then only have the classical Darcy equation on Ω, similar to Laplace's equation, which is known to be elliptic in $\mathcal{Q}_\mathrm{m}$ (under the assumption of a positive definite permeability). From Friedrich's inequality we know it can be estimated by

$$\begin{aligned} a_\mathrm{m}(p_\mathrm{m}, p_\mathrm{m}) &\geq \sum_i \left(\left\| \boldsymbol{K}_{\mathrm{m},i}^{-1} \right\|_{\mathcal{L}^\infty(\Omega_{\mathrm{m},i})} \| \nabla\, p_{\mathrm{m},i} \|^2_{\mathcal{L}^2(\Omega_{\mathrm{m},i})} \right) \\ &\overset{\text{F.}}{\geq} \mathrm{c} \left\| \boldsymbol{K}_\mathrm{m}^{-1} \right\|_{\mathcal{L}^\infty(\Omega_{\mathrm{m},1} \cup \Omega_{\mathrm{m},2})} \|p_\mathrm{m}\|^2_{\mathcal{H}^1(\Omega_{\mathrm{m},1} \cup \Omega_{\mathrm{m},2})} \,. \end{aligned} \tag{2.17}$$

The fracture part follows analogously.

$$a_\mathrm{f}(p_\mathrm{f}, p_\mathrm{f}) \geq \mathrm{c} \left\| \frac{1}{k_{\mathrm{f,t}}\; d} \right\|_{\mathcal{L}^\infty(\gamma)} \| \nabla\, p_\mathrm{f} \|^2_{\mathcal{L}^2(\gamma)} \geq \mathrm{c} \left\| \frac{1}{k_{\mathrm{f,t}}\; d} \right\|_{\mathcal{L}^\infty(\gamma)} \|p_\mathrm{f}\|^2_{\mathcal{H}^1(\gamma)} \tag{2.18}$$

2.3 Discretized Formulation – eXtended Finite Element Method

To keep the computational costs as low as possible, ideally a structured, quadrilateral grid is used for the matrix mesh. The standard Galerkin finite-element method, however, cannot handle discontinuities in the solution except by resolving them through the grid, i.e., the degrees of freedom at the discontinuities are doubled and decoupled, e.g., in structural mechanics and with a Lagrangian approach, the displacement degrees of freedom literally move away from each other. Coming from the structural-mechanics problem of evolving cracks, which lead to discontinuities in the solution (displacement, stress, strain), an extension to this standard finite-element scheme was developed, (Dolbow 1999, Dolbow et al. 2000, Mohammadi 2008), and called "eXtended finite element method" (XFEM).

From the more theoretical point, Nitsche's method, intentionally developed to handle Dirichlet constraints, evolved to a new possibility to treat interface problems, (Hansbo and Hansbo 2002, Hansbo 2005, Burman and Hansbo 2012). XFEM and

Nitsche's method applied to interface problems are in this case essentially the same approach. An overview of recent problems where XFEM methods are investigated is given in Abdelaziz and Hamouine (2008). To be able to represent the discontinuities in the solution, i.e., the jump and the average term, the extended finite element method is used as it is described for example by Dolbow et al. (2000), Hansbo and Hansbo (2004), Mohammadi (2008), and used in the fractured porous medium context for example in D'Angelo and Scotti (2012), Fumagalli and Scotti (2012), for lower dimensional fractures introducing a discontinuous solution in the matrix, for lower dimensional fracture networks having different permeabilities in the network and therefore also discontinuities, (Berrone et al. 2013), for thin heterogeneities (equidimensional) which are not resolved directly with the grid but rather with the XFEM, (Huang et al. 2011).

In the literature such techniques are very often referred to as "Partition of unity" PUFEM and "generalized-finite element methods" GFEM. The difference here is that those are usually on a global level where XFEM adopts the same techniques on an element local formulation. The composite finite element method, first presented in Hackbusch and Sauter (1997), is a special type of geometric multi-grid methods and falls therefore in the context of this manuscript in the category of multi-scale methods, cf. section 1.4.

In the classical Galerkin finite-element approach the discrete solution, $p^{\mathrm{h}}(\boldsymbol{x})$, at a global point $\boldsymbol{x}$ in space, which lies within an element E, is defined by the sum over all shape functions associated to this element multiplied by the value of the corresponding degree of freedom $\hat{p}_i$, cf. for example Braess (2007),

$$p^{\mathrm{h}}(\boldsymbol{x}) = \sum_{i=1}^{\left|\mathsf{N}^E\right|} b_i(\boldsymbol{\xi})\, \hat{p}_i. \tag{2.19}$$

Here, b_i denotes the shape function of the degree of freedom i, $\mathsf{N}^E = \{\mathsf{n}_1, \ldots, \mathsf{n}_{\mathrm{r}}\}$ denotes the set of standard degrees of freedom of the element E. The global coordinate $\boldsymbol{x}$ has to be properly transformed into element local coordinates $\boldsymbol{\xi}$ to

evaluate the shape functions correctly. All matrix elements which are not cut by a fracture are treated with such a standard finite element approach.

Remark 1. For the uncut elements standard order one elements $\mathbb{Q}_1$, bi-linear in 2d, are used. The implementation for the standard elements can be changed easily to a higher order within the limits of the underlying DUNE functionality.

If an element k is cut by a fracture, additional degrees of freedom $\hat{p}_j^{\mathrm{e}}$ are introduced. Those elements which are cut by at least one fracture are called enriched elements. The discrete solution on an enriched element k can be written as

$$p^{\mathrm{h}}(\boldsymbol{x}) = \sum_{i=1}^{\left|\mathsf{N}^{E}\right|} b_i(\boldsymbol{\xi})\, u_i^{\mathrm{s}}(\boldsymbol{x})\, \hat{p}_i + \sum_{j=1}^{\left|\mathsf{N}^{\mathrm{e},E}\right|} b_j^{\mathrm{e}}(\boldsymbol{\xi})\, u_j^{\mathrm{e}}(\boldsymbol{x})\, \hat{p}_j^{\mathrm{e}}. \tag{2.20}$$

Here, $\mathsf{N}^{\mathrm{e},E}$ is the set of enriched degrees of freedoms. To capture discontinuities in the solution the basis functions are multiplied by discontinuous functions, where u_i^{s} denotes the discontinuity functions for the standard degrees of freedom, while u_j^{e} denotes the discontinuity functions for the enriched degrees of freedom, respectively. These functions will be defined below.

In the course of this work the standard basis at cut elements is chosen to be same as for uncut elements, i.e., bi-linear and the additional shape-functions are chosen to be of the same type as the standard shape-functions, i.e., also bi-linear, $b_i = b_j^{\mathrm{e}}$ if i and j refer to degrees of freedom located at the same position. Then, b_j^{e} denotes the nodal shape function of an enriched node j. Furthermore, the XFEM concept is here used in combination with the Ritz-Galerkin approach, i.e., the basis-function space and the test-function space are equal.

Remark 2. In general it is also possible to choose different sets of basis functions for the standard and the additional degrees of freedom. Also the XFEM concept can be applied to mixed finite elements methods, such as a lowest-order Raviart-Thomas $(\mathbb{RT}_0, \mathbb{P}_0)$ combination for velocities and pressures, (D'Angelo and Scotti 2012).

The choice of the discontinuity functions is somehow arbitrary, as long as certain conditions are fulfilled. The patch test, e.g., (Bathe 2006), gives an indication but in general convergence must be proven for the newly created element (combination of number of degrees of freedom, shape functions and discontinuity functions).

One commonly desired property for the choice of discontinuity functions is to choose them such that the enriched basis functions are forced to be zero in all nodes. On the one hand this leads to a propitious quality: The nodal interpolation is still guaranteed by the solution in the standard nodes alone, (Mohammadi 2008). More importantly this property yields to enriched basis functions which are completely local with respect to the cut elements and every basis function has only one discontinuity (within this element) for every set of additional degrees of freedom. This avoids blending elements, (Fries 2008), which have to be introduced otherwise. This is only valid for the special case of a single interface per element. The general, more complex case of several (intersecting) interfaces is discussed from the point of view of the implementation in section 2.4.

Remark 3. There are many other possible choices for the discontinuity functions with different properties, e.g., they can be chosen such that the standard basis remains unmodified and the discontinuity is only represented by the enriched basis or such that the mean of the enriched basis functions is zero.

Remark 4. In structural mechanics very often not only strong/sharp discontinuity functions but rather weak/smooth functions are used to capture the underlying physical effects, represent the conceptual model discretely exact or enhance numerical stability. In this work the physical and model discontinuities are sharp and numerical instability due to the XFEM was not the case, so that such weak discontinuity functions were not used.

Remark 5. Very often the position of the interface is described by a level set method (LSM), so that the interface itself is at the zero level and on one side of the fracture the level is larger and on the other side smaller than zero. This orientation choice is also arbitrary. The LSM has its advantages mainly in the description of moving interfaces. Because the fracture network in this work is not changing, the LSM is not used.

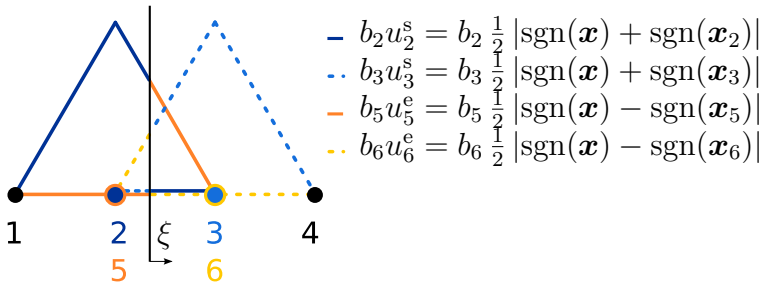

Figure 2.5: The zero dimensional fracture with local coordinate ξ divides the one dimensional matrix element. Solid lines show the two modified basis functions associated to node two (degrees of freedom two and five), dashed lines the modified basis of degrees of freedom three and six at node three.

We present here the discontinuity functions as they are implemented in the code related to this work. The sign function sgn is positive one on the side of the positive normal direction and negative one on the other. With the help of this shifted function the discontinuity functions are defined as

$$u_i^{\mathrm{s}}(\boldsymbol{x}) \coloneqq \frac{1}{2} \left| \mathrm{sgn}(\boldsymbol{x}) + \mathrm{sgn}(\boldsymbol{x}_i) \right|, \quad u_i^{\mathrm{e}}(\boldsymbol{x}) \coloneqq \frac{1}{2} \left| \mathrm{sgn}(\boldsymbol{x}) - \mathrm{sgn}(\boldsymbol{x}_i) \right|.$$

The second term, $\mathrm{sgn}(\boldsymbol{x}_i)$, associates a constant value to every node, so that the discontinuity function for the original degrees of freedom is one if $\boldsymbol{x}$ and $\boldsymbol{x}_i$ lie on the same side of the interface and zero if they are on different sides. For the additional degrees of freedom it is vice versa. The modified basis functions for this kind of discontinuity functions are exemplarily shown for the one-dimensional case in figure 2.5. For this approach, the orientation of the normal vector $\boldsymbol{n}$ of the interface has to be chosen. This choice is arbitrary.

The domain Ω is shape regularly discretized by $n^{E_{\mathrm{m}}}$ quadrilateral elements E_{m}^i into $\mathsf{T}_{\mathrm{m}}^{\mathrm{h}} = \{E_{\mathrm{m}}^i\}_{i=1}^{n^{E_{\mathrm{m}}}}$ independent of γ. Then γ is discretized with one-dimensional elements, $\mathsf{T}_{\mathrm{f}}^{\mathrm{h}} = \{E_{\mathrm{f}}^i\}_{i=1}^{n^{E_{\mathrm{f}}}}$, independent of $\mathsf{T}_{\mathrm{m}}^{\mathrm{h}}$. We define all elements, $E_{\mathrm{m}} \in \mathsf{T}_{\mathrm{m}}^{\mathrm{h}}$, which are totally in or partly belonging to $\Omega_{\mathrm{m},i}$ as $E_{\mathrm{m},i} = E_{\mathrm{m}} \cap \Omega_{\mathrm{m},i}$. All elements which are not fully included in one subdomain occur in both. The discrete space can then be defined as

$$\mathcal{Q}^{\mathrm{h}}_{\mathrm{m},i} = \{q^{\mathrm{h}}_{\mathrm{m},i} \in \mathcal{L}^2(\Omega_{\mathrm{m},i}) : q^{\mathrm{h}}_{\mathrm{m},i}|_{E_{\mathrm{m}}\cap\Omega_{\mathrm{m},i}} \in \mathbb{Q}_1(E_{\mathrm{m},i}), E_{\mathrm{m}} \in \mathsf{T}^{\mathrm{h}}_{\mathrm{m}}\}.$$

The complete discrete space for the rock matrix domain is then just the product space of the subdomain spaces $\mathcal{Q}^{\mathrm{h}}_{\mathrm{m}} = \mathcal{Q}^{\mathrm{h}}_{\mathrm{m},1} \times \mathcal{Q}^{\mathrm{h}}_{\mathrm{m},2}$, where the elements cut by a fracture are contained twice but each with the cut basis. The discrete space for γ reads

$$\mathcal{Q}^{\mathrm{h}}_{\mathrm{f}} = \{{q_{\mathrm{f}}}^{\mathrm{h}} \in \mathcal{L}^2(\gamma) : {q_{\mathrm{f}}}^{\mathrm{h}}|_{E_{\mathrm{f}}} \in \mathbb{Q}_1(E_{\mathrm{f}}), E_{\mathrm{f}} \in \mathsf{T}^{\mathrm{h}}_{\mathrm{f}}\}$$

so that the combined space is $\mathcal{Q}^{\mathrm{h}} = \mathcal{Q}^{\mathrm{h}}_{\mathrm{m}} \times \mathcal{Q}^{\mathrm{h}}_{\mathrm{f}}$ and the discrete variational formulation becomes: Find $p^{\mathrm{h}} = (p^{\mathrm{h}}_{\mathrm{m},1}, p^{\mathrm{h}}_{\mathrm{m},2}, p^{\mathrm{h}}_{\mathrm{f}}) \in \mathcal{Q}^{\mathrm{h}}_g$ such that

$$\sum_i \left(\boldsymbol{K}_{\mathrm{m},i}\,\nabla\, p^{\mathrm{h}}_{\mathrm{m},i},\ \nabla\, q^{\mathrm{h}}_{\mathrm{m},i}\right)_{\Omega_{\mathrm{m},i}} + \left(\frac{4k_{\mathrm{f,n}}}{d}\{\!\{\, p^{\mathrm{h}}_{\mathrm{m}}\,\}\!\},\ \{\!\{\, q^{\mathrm{h}}_{\mathrm{m}}\,\}\!\}\right)_{\gamma} + \left(\frac{k_{\mathrm{f,n}}}{d}[\![\, p^{\mathrm{h}}_{\mathrm{m}}\,]\!],\ [\![\, q^{\mathrm{h}}_{\mathrm{m}}\,]\!]\right)_{\gamma} = \left(\frac{4k_{\mathrm{f,n}}}{d}p^{\mathrm{h}}_{\mathrm{f}},\ \{\!\{\, q^{\mathrm{h}}_{\mathrm{m}}\,\}\!\}\right)_{\gamma} \tag{2.21a}$$

$$(k_{\mathrm{f,t}}\, d\, \nabla_{\mathrm{t}}\, p_{\mathrm{f}},\ \nabla_{\mathrm{t}}\, q_{\mathrm{f}})_{\gamma} + \left(\frac{4k_{\mathrm{f,n}}}{d}p_{\mathrm{f}},\ q_{\mathrm{f}}\right)_{\gamma} = \left(\frac{4k_{\mathrm{f,n}}}{d}\{\!\{\, p_{\mathrm{m}}\,\}\!\},\ q_{\mathrm{f}}\right)_{\gamma} \tag{2.21b}$$

for all test functions $q \in \mathcal{Q}^{\mathrm{h}}_0$ with the obvious meaning for the spaces $\mathcal{Q}^{\mathrm{h}}_g$ that include the Dirichlet boundary conditions.

Remark 6. The discrete lower dimensional gradient ∇_{t} of a one-dimensional fracture embedded in a two-dimensional matrix world is basically defined as the difference between the downstream and the upstream value divided by the distance.

Now $\mathsf{N}_{\mathrm{f}} = \{\mathsf{n}^k_{\mathrm{f}}\}_{k=1}^{n^{\mathsf{n}}_{\mathrm{f}}}$ is the set of nodes of $\mathsf{T}^{\mathrm{h}}_{\mathrm{f}}$ and $\mathsf{N}_{\mathrm{m}} = \mathsf{N}_{\mathrm{m,s}} \cup \mathsf{N}_{\mathrm{m,e}} = \{\mathsf{n}^k_{\mathrm{m}}\}_{k=1}^{n^{\mathsf{n}}_{\mathrm{m,s}}} \cup \{\mathsf{n}^k_{\mathrm{m}}\}_{k=1}^{n^{\mathsf{n}}_{\mathrm{m,e}}}$ is the combined set of standard and enriched nodes of $\mathsf{T}^{\mathrm{h}}_{\mathrm{m}}$, respectively

so that $\mathsf{N} = \mathsf{N}_\mathrm{f} \cup \mathsf{N}_\mathrm{m}$ contains all nodal degrees of freedom. The subsets $\mathsf{N}_\mathrm{f}^\mathrm{D}$ and $\mathsf{N}_\mathrm{m}^\mathrm{D}$ contain all nodes which belong to a Dirichlet boundary. Expanding (2.21) with (2.20) and analogously for the fracture, (2.19), gives: Find all $\hat{p}_{\mathrm{m},j}$ and $\hat{p}_{\mathrm{f},l}$ such that in rock matrix elements:

$$\begin{aligned}
&\sum_{\mathsf{n}_j \in \Omega_1} \hat{p}_{\mathrm{m},j} \left(\boldsymbol{K}_{\mathrm{m},1} \nabla b_{\mathrm{m},j},\ \nabla b_{\mathrm{m},i} \right)_{\Omega_1} + \sum_{\mathsf{n}_j \in \Omega_2} \hat{p}_{\mathrm{m},j} \left(\boldsymbol{K}_{\mathrm{m},2} \nabla b_{\mathrm{m},j},\ \nabla b_{\mathrm{m},i} \right)_{\Omega_2} \\
&\quad + \sum_{\mathsf{n}_j \in \Omega_1 \cup \Omega_2} \hat{p}_{\mathrm{m},j} \left(\frac{4k_{\mathrm{f,n}}}{d} \{\!\{ b_{\mathrm{m},j} \}\!\},\ \{\!\{ b_{\mathrm{m},i} \}\!\} \right)_\gamma \\
&\quad + \sum_{\mathsf{n}_j \in \Omega_1 \cup \Omega_2} \hat{p}_{\mathrm{m},j} \left(\frac{k_{\mathrm{f,n}}}{d} [\![b_{\mathrm{m},j}]\!],\ [\![b_{\mathrm{m},i}]\!] \right)_\gamma \\
&\qquad = \sum_{\mathsf{n}_l \in \gamma} \hat{p}_{\mathrm{f},l} \left(\frac{4k_{\mathrm{f,n}}}{d} b_{\mathrm{f},l},\ \{\!\{ b_{\mathrm{m},i} \}\!\} \right)_\gamma \quad \forall i : \mathsf{n}_\mathrm{m}^i \in \mathsf{N}_\mathrm{m} \backslash \mathsf{N}_\mathrm{m}^\mathrm{D}
\end{aligned} \tag{2.22a}$$

in fracture network elements:

$$\begin{aligned}
&\sum_{\mathsf{n}_l \in \gamma} \hat{p}_{\mathrm{f},l} \left(k_{\mathrm{f,t}}\, d\, \nabla_\mathrm{t}\, b_{\mathrm{f},l},\ \nabla_\mathrm{t}\, b_{\mathrm{f},z} \right)_\gamma + \sum_{\mathsf{n}_l \in \gamma} \hat{p}_{\mathrm{f},l} \left(\frac{4k_{\mathrm{f,n}}}{d} b_{\mathrm{f},l},\ b_{\mathrm{f},z} \right)_\gamma \\
&\qquad = \sum_{\mathsf{n}_j \in \Omega_1 \cup \Omega_2} \hat{p}_{\mathrm{m},j} \left(\frac{4k_{\mathrm{f,n}}}{d} \{\!\{ b_{\mathrm{m},j} \}\!\},\ b_{\mathrm{f},z} \right)_\gamma \quad \forall z : \mathsf{n}_\mathrm{f}^z \in \mathsf{N}_\mathrm{f} \backslash \mathsf{N}_\mathrm{f}^\mathrm{D}
\end{aligned} \tag{2.22b}$$

and $\hat{p}_{\mathrm{m},i} = g \quad \forall i : \mathsf{n}_\mathrm{m}^i \in \mathsf{N}_\mathrm{m,s}^\mathrm{D}$ and $\hat{p}_{\mathrm{f},z} = g \quad \forall z : \mathsf{n}_\mathrm{f}^z \in \mathsf{N}_\mathrm{f}^\mathrm{D}$.

Remark 7. Equations (2.22a) and (2.22b) form now a linear system of equations which can be solved either directly as a whole in a monolithic approach or iteratively for the fracture and matrix part separately.

Because the Dirichlet boundary function g can be in general of higher order or even discontinuous across $\partial\gamma$, the enriched nodal degrees of freedom on a Dirichlet boundary have to be chosen such that g is approximated best with respect to the order of the ansatzfunctions, in this case linearly, e.g., find the matrix element k

which is cut by γ on the Dirichlet boundary and choose two $\boldsymbol{x}_\mathrm{e}$ close to $\partial\gamma$, each on one side, and evaluate

$$p_\mathrm{m}^\mathrm{h} = \sum_{\substack{i \\ \mathsf{n}_i \in \mathsf{N}_{\mathrm{m,s}}^k}} b_i^\mathrm{s}(\boldsymbol{\xi}_\mathrm{e})\, u_i^\mathrm{s}(\boldsymbol{x}_\mathrm{e})\, \hat{p}_i^\mathrm{s} + \sum_{\substack{j \\ \mathsf{n}_j \in \mathsf{N}_{\mathrm{m,e}}^k}} b_j^\mathrm{e}(\boldsymbol{\xi})\, u_j^\mathrm{e}(\boldsymbol{x}_\mathrm{e})\, \hat{p}_j^\mathrm{e} = g(\boldsymbol{x}_\mathrm{e})$$

for the unknowns $\hat{p}_{\mathrm{m},j}^\mathrm{e}$ with given $\hat{p}_{\mathrm{m},i}^\mathrm{s}$.

2.4 XFEM for Multiple Interfaces

The intersection or crossing of fractures is discussed in detail in chapter 5. This section only presents the conceptual model for XFEM for multiple interfaces, i.e., the matrix part which contains more than one discontinuity interface in one element.

The XFEM concept can also handle multiple interfaces within one element. For every new partition of the element, one set of additional degrees of freedom is needed, i.e., for two not-crossing fractures the element is divided into three sub-element regions so that two sets of additional unknowns are used. For two crossing fractures the element is divided into four sub-element regions so that three sets of additional unknowns are used, cf. figure 2.6. This is necessary to represent a solution which has support in only one of the sub-element regions.

The discrete form looks similar to (2.20). However, two differences should be noted. First, the set of enriched degrees of freedom has changed and its size is now $\left|\mathsf{N}^{\mathrm{e},k}\right| = 4(n_\mathrm{fb}^k - 1)$ for $n_\mathrm{fb} \leq 2$ for $\mathbb{Q}_1$ elements, where n_fb^k is the number of fracture branches inside this element k. Second, the discontinuity functions are different.

The choice of discontinuity functions $u_i^\mathrm{s}, u_j^\mathrm{e}$, presented above, works fine for cases where only one interface per element is allowed, e.g., structural mechanics with non-intersecting cracks or direct simulation of two phase flow where the interface separates the different phases, (Schott 2010), or the situation of a single fracture per element presented here.

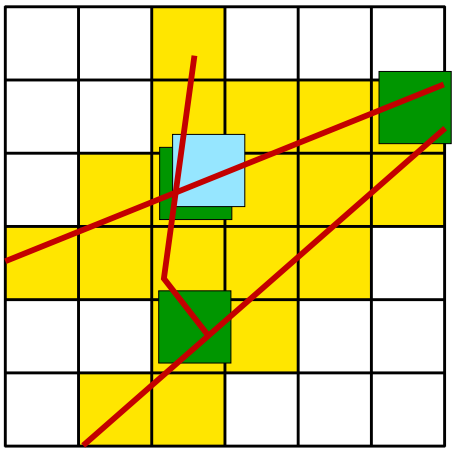

Figure 2.6: A structured matrix mesh and different fracture situations: White are standard elements, colored are enriched (XFEM) elements. The first set of additional degrees of freedom is marked yellow, the second green and the third blue.

For a matrix dimension larger than one and more than one single fracture per element, e.g., one fracture splitting into two, the discontinuity functions, (2.23a), can be chosen in a similar way as for a single fracture:

$$u_i^{\mathrm{s}}(\boldsymbol{x}) \coloneqq \begin{cases} 1 & \text{if } \boldsymbol{x}, \boldsymbol{x}_i \text{ in } E_j, \forall j \\ 0 & \text{else} \end{cases} \qquad \text{for } i = 1, \ldots, 4, \tag{2.23a}$$

$$u_{i,j}^{\mathrm{e}}(\boldsymbol{x}) \coloneqq \begin{cases} 1 & \text{if } \boldsymbol{x} \quad \text{in } E_j^i \\ 0 & \text{else} \end{cases} \qquad \text{for } i = 5, \ldots, (4n_{\mathrm{fb}}). \tag{2.23b}$$

Every basis function has support only on one sub-element region, cf. figure 2.7, and the sum over all basis functions is equal to one at every point in space. The local finite element area of element E, Ω^E is composed of the sub-elements, $\Omega^E = \bigcup_j E_j$, where E_j is the j-th sub-element area within n_{fb}^E sub-elements of the element E.

For the discontinuity function each nodal degree of freedom gets associated to a sub-element. For the discontinuity function of the standard basis the associated sub-element j is always the one which contains the node. To every enriched degree of freedom also one sub-element gets associated. This sub-element is called E_j^i.

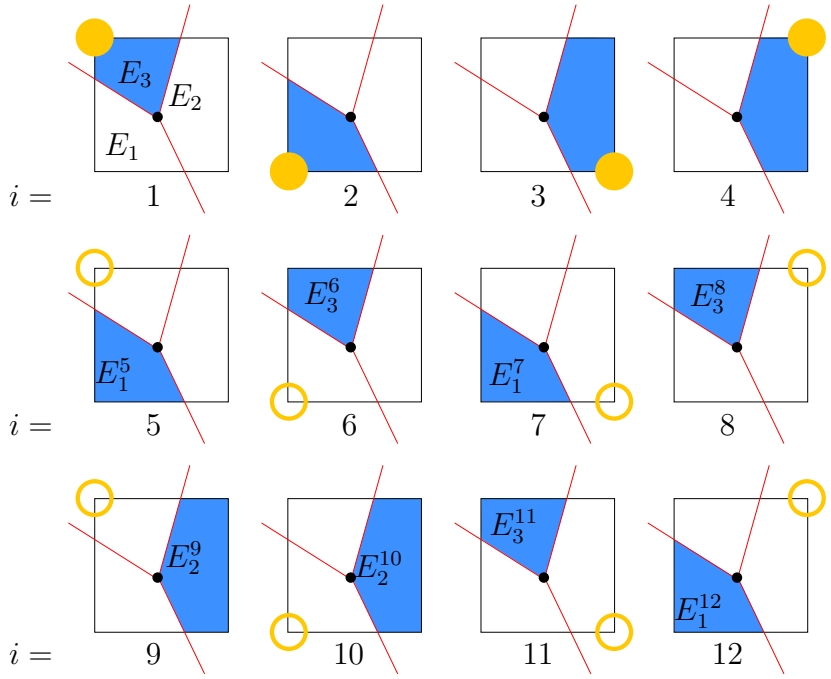

Figure 2.7: The first row shows the set of standard basis functions, the second and third row show the first and second set of additional basis functions. The yellow dot/circle marks the position of the corresponding nodal basis function. The red lines symbolize a fracture which splits into two. The blue areas show the region of support for each basis function.

This cannot be the sub-element which is associated to the standard nodal degree of freedom. The choice between the remaining sub-elements is somehow arbitrary. There are, however, restrictions which are more complex than for the single fracture (two fracture branches) case, in other words, this choice is not anymore element local but node-global, cf. figures 2.8 and 2.9.

Element 2 needs two additional sets of degrees of freedom. In the neighbouring elements 1 and 3 only one additional set is necessary, respectively, cf. figure 2.8. The basis functions associated to the central node, however, have to be continuous across element edges and must only be discontinuous across the fractures. There are three degrees of freedom at the marked, central node ●, and we name them a,b,c. The standard basis function has support, if it is on the same side of the fracture(s) as the nodal degree of freedom. The degree of freedom a does never pose any problem to the association of areas of support to this degree of freedom.

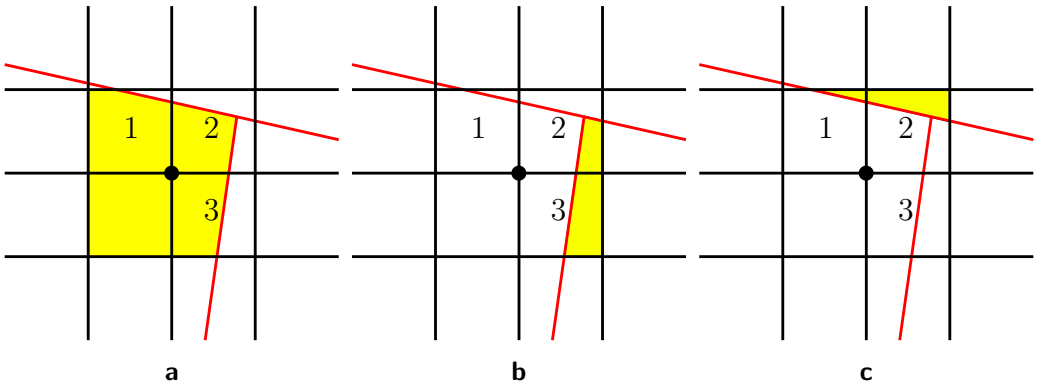

Figure 2.8: Node global problem of basis function support

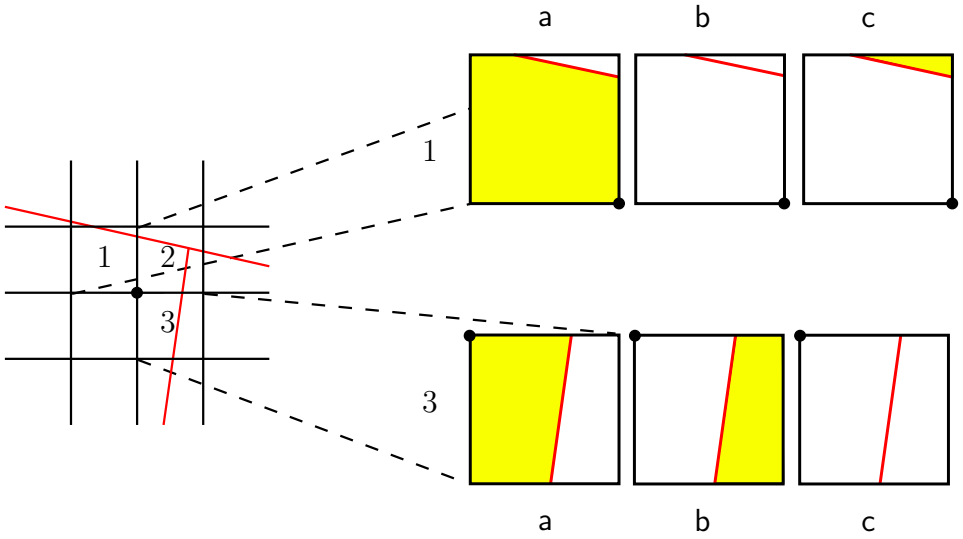

Figure 2.9: Area of support for the degrees of freedom a,b,c

The degrees of freedom b,c, however, have either no support in element 1 or 3 and depending on this choice, the subregions in element 2 are associated to the degrees of freedom, cf. figure 2.9.

2.5 Implementation and Employed Software Packages

This section gives an overview of utilized software packages which provide a foundation for the development of the simulation toolbox created in this project. Also, the actual implementation and code specific details of the model concept and discretization technique presented in previous sections are presented. XFEM related details and its employment are described in sections 2.5.1 to 2.5.3 whereas the fracture network related details are presented in section 2.5.4. The model concept and implementation for the XFEM for immersed interfaces, i.e., fractures which end inside the domain are presented and discussed in chapter 4.

The implementation of the model concept is based on the free and open source software package DUNE, "the Distributed and Unified Numerics Environment, a modular toolbox for solving partial differential equations with grid-based methods", (Bastian et al. 2008a,b). The "Iterative Solvers Template Library (ISTL)", (Blatt and Bastian 2007), allows the usage of different solvers for the linear equation system via so called adapters. In this work the direct solver SuperLU, (Li 2005, Li et al. 1999), is used if not explicitly stated otherwise.

For the rock matrix part the finite element toolbox UG, (Bastian et al. 1997), is used as grid manager, because at the point in time of the implementation it was the only DUNE compatible grid manager which could handle unstructured, mixed simplex-quadrilateral grids. The fracture network part uses the finite element toolbox ALBERTA, (Schmidt and Siebert 2005), as grid manager, because at the point in time of the implementation it was the only publicly available and DUNE compatible grid manager which provided co-dimension one functionality.

The domain decomposition into cut and uncut rock matrix elements is handled by the DUNE module dune-multidomaingrid, (Müthing and Bastian 2012). The XFEM implementation is based on the DUNE modules dune-PDELab, "an extensible C++ template library for finite element methods based on DUNE" (Bastian et al. 2010b), and dune-multidomain which "... extends PDELab for solving heterogeneous

problems on spatial subdomains in an easy way. These subdomains are managed using another DUNE module called dune-multidomaingrid" (Müthing 2014).

The coupling of two different grids is implemented manually. The module dune-grid-glue (Bastian et al. 2010a), claims to be able to handle all such grid cases but was at the time of the implementation not compatible with PDElab. To improve the flexibility and reduce the maintenance effort for the implementation presented here the possibility to include dune-grid-glue should be part of future work.

2.5.1 XFEM for Multiple Intersecting Interfaces

There are infinitely many cases in which the matrix elements can be intersected by fractures. The model concept presented here is intended to be applied to large scale fractures which show significant influence throughout the whole simulation domain, cf. section 1.5. Therefore, it is assumed that it is sufficient for the XFEM implementation in this work to handle up to four fracture branches per XFEM element. Figure 2.10 shows all implemented cases for up to four fracture branches. It only shows the intersection cases for a structured grid with quadratically shaped elements. The extension towards any, not self-intersecting, two-dimensional, four edged element is straightforward and does not introduce other cases. For cases a and b it is also allowed that the fracture intersects the XFEM element at two neighboring edges. There are also cases which are at the moment not implemented. Those are depicted in figure 2.11. Case a also represents two not intersecting bending fractures. If case a is not allowed this automatically leads to an exclusion of cases b–d, but they require a different implementation on their own, too. A detailed discussion of a–d is part of this section whereas case e is further discussed in chapter 4.

As presented in section 2.4 the definition of the discontinuity functions and therefore the area of support for each nodal basis is not anymore an element local decision, but node global. In the following a solution to this problem and its implementation is presented. The idea is to transform the node-global problem of basis function support into an element local problem so that the assembling can still be carried out in element local operators, cf. section 2.5.5.

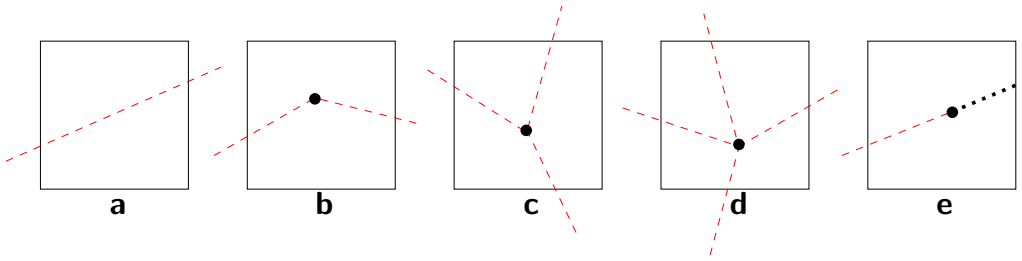

Figure 2.10: XFEM interface cases which are implemented: **a** single straight fracture without a node in the XFEM element, **b** single bending fracture, **c** Y-crossing, **d** X-crossing, **e** ending fracture with the projected intersection on the edge opposite of the real intersection

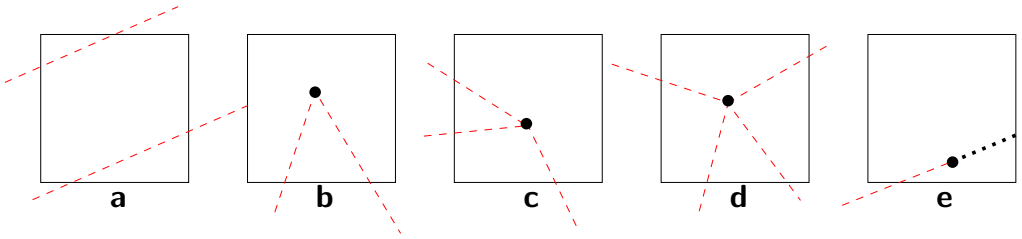

Figure 2.11: XFEM interface cases which do not require additional theory but a different implementation: **a** two not-intersecting fractures, **b–d** single fracture, Y-crossing, X-crossing with two intersections on one edge respectively, **e** ending fracture with the projected intersection on an edge neighboring the real intersection

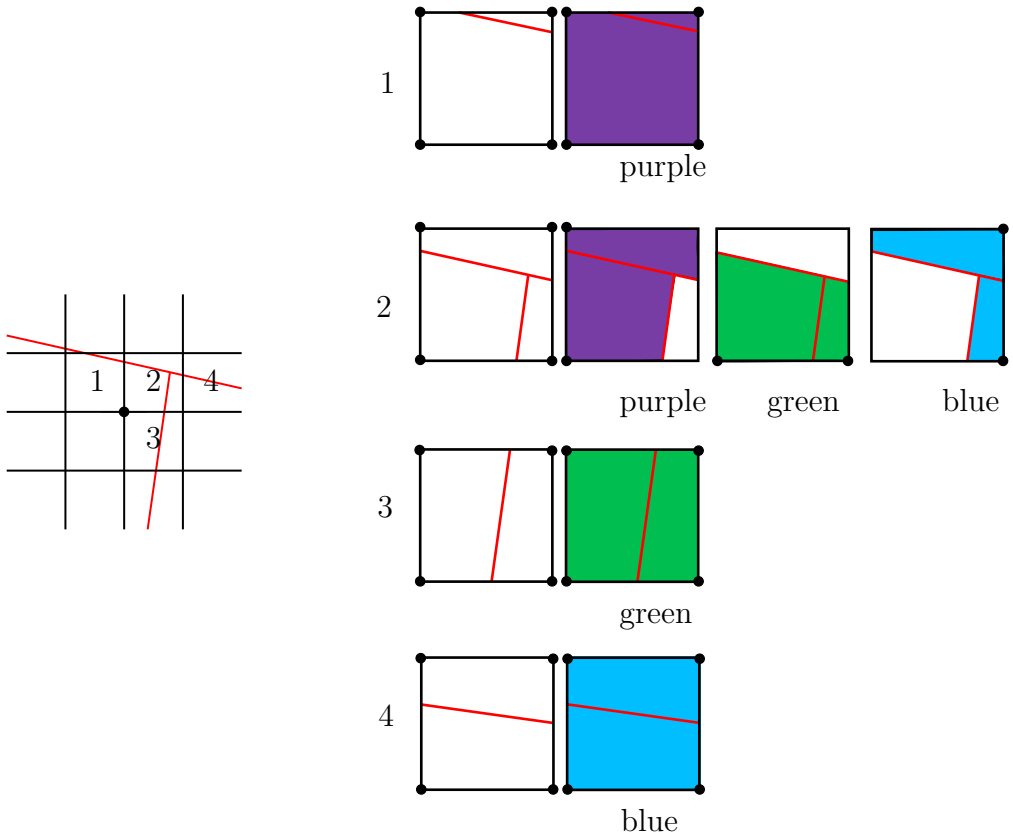

Figure 2.12: Converting the node global problem of shapefunction support into an element local one with the help of an edge coloring algorithm

The following describes the handling of Y-crossings and X-crossings. Bending fractures do not need a special treatment. For every fracture branch an additional set of degrees of freedom is used, i.e., a Y-crossing has three additional sets of degrees of freedom and an X-crossing four. That leads to more degrees of freedom than necessary and discussed in section 2.4. Such elements follow the idea of the so called "blending elements" in structural mechanics. To overcome the problem of too many degrees of freedoms, additional discontinuity functions are introduced which simply are zero everywhere and rule out the influence of the superfluous degrees of freedom. The correct association of the discontinuity function itself is a global problem, but once carried out it gives the possibility to assemble the global system via element local operators.

The global discontinuity function association problem is solved with an algorithm

based on the edge-coloring problem. Vizing's theorem, cf. theorem C.1, states that at maximum one plus the maximal number of fracture branches in one crossing is needed to color the graph with a minimum of different colors. In some cases only the maximal number of fracture branches in one crossing is sufficient to color the graph. To determine if the lower number is sufficient, however, is an np-complete problem, (Leeuwen et al. 1990).

For the application in the case of the XFEM implementation with dune-multidomain, it is not relevant if and how the problem can be solved exactly with the minimum number of colors. In this case the computational time to solve the problem is more relevant than the storage which is needed when simply more available colors are allocated and distributed in an efficient way. There are algorithms available which solve the problem with more colors than necessary, e.g., (Misra and Gries 1992).

For the implementation of a maximum of four fracture branches, theorem C.1 states that at most five colors are needed. In the implementation six colors are available to speed up the coloring algorithm. The simplest version of the implemented coloring algorithm is shown in algorithm C.2. The implementation uses here a subdomain from dune-multidomaingrid to store and distinguish the different colors.

An exemplary Y-crossing is shown in figure 2.12. The mandatory color choices for all degrees of freedom are shown. After the mandatory choices the basis is not fully complete, i.e., in this case the upper left and right degree of freedom lack support in the lower right and left sub-element. The choice to which colored elements those degrees of freedom are assigned with non-zero support, is arbitrary.

This algorithm is based on the initially given discrete fracture network before its elements are created, i.e., it has only vertices where a fracture ends, bends or intersects with other fractures, cf. section 2.5.4. The algorithm does not know the XFEM grid and therefore cannot detect if two fractures are contained within one XFEM grid cell and would need another color. An extension of the algorithm to possibly handle such cases is given in algorithm C.3. Because of the additional condition given by the grid, i.e., from outside the graph, the problem is not anymore

comparable to a classical edge coloring problem and the proof and implementation of an efficient algorithm remains future research.

2.5.2 Corner Cut and Touched Elements

To be able to simulate almost arbitrary fracture networks, i.e., situations of interfaces cutting through matrix elements, in addition to the above presented interface cases, two non-standard cases have to be implemented. On the one hand there is the case of a fracture cutting directly through a corner, cf. section 2.5.2, and for bi-linear finite elements through the position of the degree of freedom. On the other hand a fracture can be aligned with an element edge, cf. figure 2.13b, and that means for structured grids with all edges over the lateral extension of the fracture.

In general those cases are not related to the XFEM because they can be handled by a standard finite element method, where the interface is resolved through the grid, i.e., the the degrees of freedom are doubled at the interface and completely decoupled at first and later coupling conditions such as for crack development in structural mechanics can be applied. This behavior can be emulated by the XFEM. The previously discussed discontinuity functions cannot be applied, because that would mean the enriched degrees of freedom have simply no support at all.

To circumvent that problem the following scheme is suggested: At first, the fracture normal direction is defined. The fracture is virtually moved a little away from the intersection in normal direction, so that the cut/touched degrees of freedom lie on the other side of the fracture than the rest. Now the support area is defined as the whole element or no support. The element(s) on the negative normal fracture side are also enriched. The fracture is again virtually moved away from the intersection but this time in negative normal direction. The support area is defined again as the full element or the empty space, but this time the enriched and standard degrees of freedom switch their support area. That basically mimics the doubling and splitting of the standard degrees of freedom for classical finite element methods.

a corner cutting fracture **b** edge aligned fracture

Figure 2.13: Special cases of fracture alignment

The choice of discontinuity functions is for the method presented above again not element local, but must be carried out dependent on neighboring elements. Another difficulty arises for the implementation of the coupling part, where the average and jump of the matrix pressure is not anymore element local. That is the reason why extensive testing of these two special intersection cases remains future research.

2.5.3 XFEM and Numerical Integration

For the numerical integration of the matrix terms in the context of the XFEM, the numerical integration has to be able to capture the discontinuity. This can exactly be achieved by dividing the enriched element into sub-elements, cf. figure 2.14. On each of those sub-elements a standard Gaussian integration rule with an order corresponding to the order of the basis functions is used and gives the position and weights for each integration point on each sub-element, i.e., there is no approximation due to the numerical integration.

Tests have shown that it is also possible to avoid this sometimes complex geometrical sub-element division and using instead a Gaussian integration rule of a very high order (> 15) on the genuine element to approximate the integration of the discontinuous basis functions. However, this high order cannot integrate the discontinuous basis exactly and oscillation effects close to the interface occur. Because normally an exact visualization of the discontinuity is desired and most visualization tools, including the free post processing software tool Paraview which is used to visualize the results in this work, cannot handle discontinuous basis functions, the visualization is carried out on a new visualization grid which introduces additional nodes exactly at each side of the discontinuities. Therefore a sub-triangulation has to be calculated anyway. In the results presented in this work only the sub-triangulation integration is used. This sub-triangulation works for single as well as multiple interfaces.

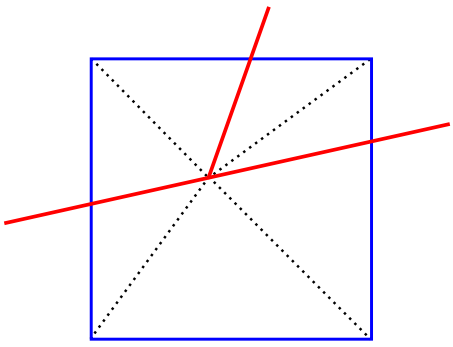

Figure 2.14: Sub-triangulation example of a cut element for numerical integration and similar for visualization purposes.

Another challenge arises for non-standard, i.e., rectangular, elements. This is due to the fact that the assembling of the global stiffness matrix is carried out, as usually the case for most finite element codes, locally on every element with its respective contribution to the global system. For non-rectangular elements the global-local transformation is possibly not affine, i.e., the globally straight line fractures can become non-linear connections between vertices. Tests showed that the change in curvature has no significant influence on the global solution. But the position of the fracture has to be the same for all terms which include the fracture, i.e., the XFEM matrix volume terms because of the cut support area as well as the coupling terms itself which are evaluated on the fracture and include matrix pressures on both sides of the interface. The current implementation transforms each integration point on the fracture exactly into the element local coordinate system so that there is no error for the terms evaluated on the fracture. The linear connection between the transformed integration points gives the element local interface for the volume terms of the cut matrix elements. That is not exact but it seems accurate enough to make the implementation stable.

2.5.4 Fracture Network

The physical concept for flow in crossings is described in chapter 5. This section is about the general implementation of the fracture network.

It is assumed that the fracture network is given discretely as a graph of vertices and edges which form the fracture network $\gamma = \cup_j \gamma_j$. Edges are always straight lines between vertices in global coordinates. Such networks can be created for example with the stochastical fracture generator Frac3d, (Silberhorn-Hemminger 2002). Every fracture has only two nodes except for the case that it is not straight, where it has one additional node at every kink. Every crossing has exactly one node at the intersection of the fractures. Overlapping fractures without a connection are not allowed.

Inside DUNE the fracture network is handled with the grid manager ALBERTA, (Schmidt and Siebert 2005). At the moment of the implementation, ALBERTA was

not able to handle crossing one-dimensional elements, so that this functionality is implemented manually when reading the fracture grid from the art format into a DGF. The intersection vertex is doubled so that crossing fractures are virtually split into overlapping fractures without a connection. The doubled vertices are stored. In the assembled matrix the degrees of freedom associated with a doubled vertex are set to be equal, i.e., the matrix rows are added onto one row and the other row is replaced with an empty line except for the one on the main diagonal and analogously for the right hand side.

2.5.5 PDELab and Local Operators

The basis for the implementation of the model concept is given by PDELab. It assembles the global problem by traversing all elements, calculating the relevant terms locally and then writing them into the global system matrix or vector. This is a standard approach in finite element theory and codes. The element local function for calculating the element matrix and right hand side is called “local operator”.

For the model presented here, there are four different local operators. The first is the standard Darcy operator, which is used on all rock matrix elements without any contact to a fracture. The second is the XFEM-Darcy operator which is used to treat the rock matrix elements with a fracture. The third is the lower-dimensional fracture Darcy operator and the fourth the coupling operator which contains unknowns from the rock matrix and the fracture grid. This split into different local operators leads to a very clear and structured code which is directly related to the weak formulation. It also offers a great flexibility whenever only some parts of the model concept are changed. Such partial changes can easily be incorporated into the code.

2.5.6 Local Mass Conservation

It is known that the standard finite element method without any additional concepts is not necessarily locally conservative, e.g., chapter four in Flemisch (2013). Locally conservative schemes have to fulfill two conditions. The first is seen locally from the

element, where all fluxes over all edges have to be equal to the source term. This is often called "What goes in, must go out". The second is that the flux across one edge between neighboring elements i and j has to be the same from element i to j as the negative flux from j to i, or "What goes out (from element j across one edge), must go in again (into element i over the shared edge)".

The problem for standard finite element methods is to calculate the flux across the edges, because of the discontinuity of the gradient of the shapefunctions at the edges. For the XFEM approach presented here this is not a problem for the fluxes between fracture and matrix. They are directly included in the conceptual model and the discretization inside the cut elements has uniquely defined gradients at the fracture-matrix interface. The problem still holds in areas without fractures, inside the fractures itself and at the intersection between XFEM elements and standard elements.

Since we do not use the fluxes for solving additional transport equations, the missing local mass conservation poses no problem for this work. However, it becomes relevant if the pressure flow model should be extended towards transport simulation.

2.6 Dimensional Analysis

In the context of this work dimensionless and scaled equations are used. To simulate application oriented problems with physical fluid and soil properties and boundary conditions this section gives the derivation for the dimensionless, scaled equations for heterogeneous (fractured) porous medium problems starting from the dimensional equations for homogeneous porous media flow. The dimensional quantities are marked with a $\tilde{(\cdot)}$.

$$\frac{\partial \tilde{\varrho}}{\partial \tilde{t}} + \tilde{\nabla} \cdot (\tilde{\varrho} \tilde{\boldsymbol{u}}) = \tilde{s} \tag{2.24a}$$

$$-\frac{1}{\tilde{\mu}} \tilde{\boldsymbol{K}} \tilde{\nabla} \tilde{p} = \tilde{\boldsymbol{u}} \tag{2.24b}$$

The flow field is assumed to be stationary, i.e., $\partial\tilde{\varrho}/\partial\tilde{t} = 0$. Darcy's law, (2.24b) can be integrated into the mass continuity equation, (2.24a), and with the kinematic viscosity $\tilde{\nu} = \tilde{\mu}/\tilde{\varrho}$ that leads to the dimensional pressure equation (2.25).

$$\tilde{\nabla} \cdot \left(-\frac{1}{\tilde{\nu}} \tilde{\boldsymbol{K}} \, \tilde{\nabla} \, \tilde{p} \right) = \tilde{s} \tag{2.25}$$

For an incompressible fluid with constant dynamic viscosity, i.e., $\tilde{\nu} = \text{constant}$, the mass flux per volume and time and thus the Darcy velocity depend only on the intrinsic permeability and the pressure gradient locally and the fluid properties globally. For heterogeneous problems with fractures the permeability can be split into fracture domain and matrix domain permeabilities and additionally the fracture aperture, also dependent on the position, appears.

Expressing the vectorial and tensorial quantities as scalar with (double) index defining the direction of it, table 2.1 shows all relevant parameters for the dimensional analysis. The Buckingham-Π theorem states that for nine physical parameters and a three dimensional physical quantity space, exactly six dimensionless relations can be found to describe the system.

Table 2.1: Dimensional analysis variables

pressure difference	$\Delta\tilde{p}(\boldsymbol{x})$	$^{\mathrm{kg}}/_{\mathrm{m\cdot s^2}}$
permeability	$\tilde{k}(\boldsymbol{x})_{ij}$	m^2
fluid dynamic viscosity	$\tilde{\mu}$	$^{\mathrm{kg}}/_{\mathrm{m\cdot s}}$
pressure	$\tilde{p}(\boldsymbol{x})$	$^{\mathrm{kg}}/_{\mathrm{m\cdot s^2}}$
velocity	$\tilde{u}_i$	$^{\mathrm{m}}/_{\mathrm{s}}$
fluid density	$\tilde{\rho}$	$^{\mathrm{kg}}/_{\mathrm{m^3}}$
position	$\tilde{\boldsymbol{x}}$	m
fracture aperture	$\tilde{d}(\boldsymbol{x})$	m
characteristic domain length	$\tilde{D}$	m

Starting from (2.25) the pressure difference $\Delta\tilde{p}$, matrix permeability $\tilde{k}_\mathrm{m}$ and fluid viscosity $\tilde{\mu}$ are chosen as physical parameters. That leads directly to three dimensionless products:

$$\Pi_1 = \frac{\tilde{p}}{\Delta\tilde{p}} =: p \tag{2.26a}$$

$$\Pi_2 = \frac{\tilde{\mu}\,\tilde{u}_i}{\tilde{k}_\mathrm{m}^{1/2}\,\Delta\tilde{p}} \tag{2.26b}$$

$$\Pi_3 = \frac{\tilde{k}_\mathrm{m}\,\Delta\tilde{p}\,\tilde{\varrho}}{\tilde{\mu}^2}. \tag{2.26c}$$

For fractured porous media the fourth relation is obvious.

$$\Pi_4 = \frac{\tilde{k}_{ij}}{\tilde{k}_\mathrm{m}} =: \begin{cases} k_\mathrm{f,n} & \text{if } \boldsymbol{x} \text{ in } \gamma \text{ in normal direction} \\ k_\mathrm{f,t} & \text{if } \boldsymbol{x} \text{ in } \gamma \text{ in tangential direction} \\ k_\mathrm{m} & \text{if } \boldsymbol{x} \text{ in } \Omega_\mathrm{m} \end{cases}$$

An order-of-magnitude analysis for typical porous media applications leads to the result that for most applications $\tilde{k}_\mathrm{m}$ is small (e.g., $< 10^{-8}\,\mathrm{m}^2$) and the domain size is large (e.g., $\mathcal{O}$(km) for groundwater flow). Thus additionally the domain length is fixed and one dimensionless product is eliminated, i.e., the dimensional relation $\Pi = \tilde{k}_\mathrm{m}/\tilde{D}^2$ is explicitly decoupled. The remaining two products are the dimensionless fracture aperture and the position within the domain.

$$\Pi_5 = \frac{\tilde{\boldsymbol{x}}}{\tilde{D}} =: \boldsymbol{x} \qquad\qquad \Pi_6 = \frac{\tilde{a}}{\tilde{D}} =: a$$

The dimensionless pressure equation is now given by

$$\nabla \cdot (-\boldsymbol{K}\,\nabla\, p\,) = s \tag{2.27}$$

where the dimensionless source term is scaled, $s = \tilde{s}\,(\tilde{\nu}/\Delta\tilde{p})$, i.e., as long as there is no source term in dimensional form given the scaling does not affect the similitude.

Table 2.2: Typical numbers for fluid and soil properties in groundwater applications (Bear 1988, Belayneh et al. 2006), i.e., viscosity, density and velocity are given for water.

$\tilde{\boldsymbol{K}}$	$\approx 10^{-8} \sim 10^{-19} \cdot \mathbf{I}$	m^2
$\tilde{\mu}\,(10°\mathrm{C})$	$\approx 1.308 \cdot 10^{-3}$	$^{\mathrm{kg}}/_{(\mathrm{m}\cdot\mathrm{s})}$
$\tilde{\varrho}$	≈ 1000	$^{\mathrm{kg}}/_{\mathrm{m}^3}$
$\tilde{\boldsymbol{u}}_{\mathrm{D}}$	$\approx 7 \cdot 10^{-5}$	$^{\mathrm{m}}/_{\mathrm{s}}$

To introduce a Reynolds number related to the flow problem the square root of the permeability is used as characteristic length. The flow velocity in the problem setup is seen as the result of a pressure gradient and thus, leads to Reynolds and Euler numbers which cannot be chosen a priori but are part of the result. A rearrangement of (2.26b) and (2.26c) leads to the Reynolds number Re and the Euler number Eu:

$$\mathrm{Re}_k = \frac{\tilde{u}\,\tilde{\varrho}\,\tilde{k}_{\mathrm{m}}^{1/2}}{\tilde{\mu}} = \Pi_2 \cdot \Pi_3, \tag{2.28a}$$

$$\mathrm{Eu} = \frac{\Delta\tilde{p}}{\tilde{\varrho}\,\tilde{u}^2} = 1/(\Pi_2^2 \cdot \Pi_3). \tag{2.28b}$$

For the similitude of two flow fields except for the directly appearing parameters $p, d, k_{\mathrm{m}}, k_{\mathrm{f,n}}, k_{\mathrm{f,t}}$ furthermore the Re_k and Eu similarity has to be fulfilled.

In many cases, the reformulation of physical equations into a dimensionless form and an additional scaling of the important parameters, can influence the stability of implementations of numerical schemes especially if the input parameters vary in orders of magnitude, as they do for example in groundwater flow, table 2.2.

3 Validation of the Model Concept and Implementation

In this chapter a validation approach for the implemented model is presented. First, in section 3.1, the negligible influence of the averaging parameter is shown for a representative example. In section 3.2, the model applied to a single horizontal fracture is compared against an analytical solution.

3.1 Influence of the Averaging Parameter

In section 2.1, the averaging parameter $\zeta \in (0.5, 1.0]$ was presented. In Martin et al. (2005) the theoretical influence of ζ on the stability of the mixed formulation (saddle-point problem) was shown. In contrast, this section shows the negligible influence in the primal formulation by means of two examples. The first example is a one-dimensional domain with a zero-dimensional discontinuity, i.e., only flow normal to the fracture is assumed.

The boundary conditions are given as Dirichlet values on both ends, and the single fracture value is explicitly set by means of a Dirichlet value. Three different matrix pressure distributions are shown in figure 3.1 for a fixed aperture and a almost impermeable fracture. It is obvious that the influence of ζ on the matrix pressure distribution can be neglected. For higher permeable fractures this influence becomes even less significant (not shown here).

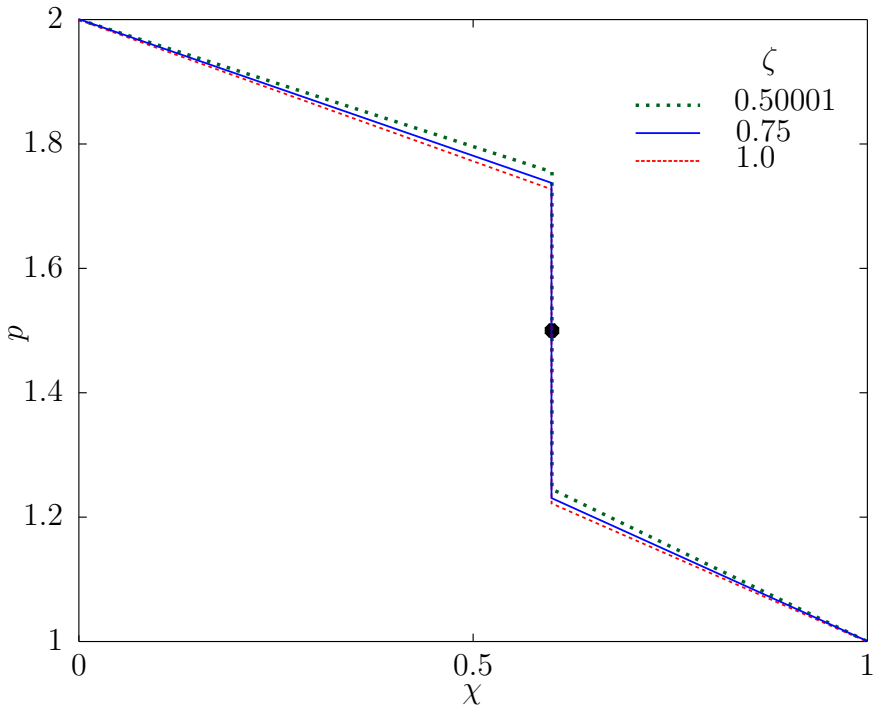

Figure 3.1: 1d pressure distribution for $d = k_{\mathrm{f,n}} = 10^{-4}, k_{\mathrm{m}} = 1.0$ and three different values for the averaging parameter $\zeta \in \{1.0, 0.75, 0.50001\}$

The second example, figure 3.2, is a two-dimensional matrix domain with a single inclined fracture. The boundary conditions are Dirichlet on the bottom and top boundary with a gradient from bottom to top. The left and right hand side have Neumann boundary conditions, for the matrix no flow and for the fracture inflow on the left and outflow on the right. The fracture is almost impermeable in normal direction and, to show the influence of two-dimensional problem, highly conductive in tangential direction. The cases of a highly permeable or almost impermeable fracture in tangential and normal direction show similar results with even less visible influence of the averaging parameter. The results of a negligible influence of the averaging parameter in an asymptotic model is in contrast to Angot et al. (2009).

For more complex fracture network cases, it can be observed that the value of $\zeta = 1.0$ leads to the most stable results. That is probably due to the implementation and possible numerical rounding errors if $\zeta \to 0.5$. Thus, in the course of this work and the presented results the averaging parameter is always chosen to be $\zeta = 1.0$.

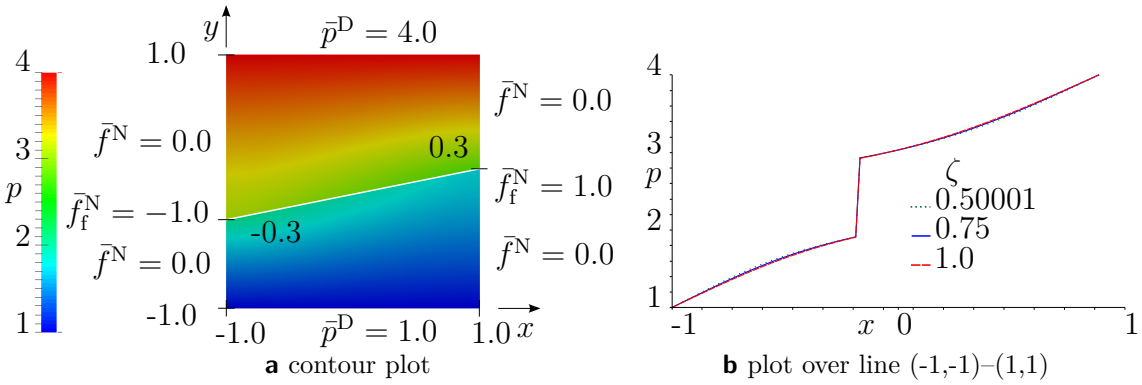

Figure 3.2: Influence of the averaging parameter in 2d for $d = k_{\mathrm{f,n}} = 10^{-4}, k_{\mathrm{f,t}} = 10^{4}, k_{\mathrm{m}} = 1.0$, with $\zeta \in \{1.0, 0.75, 0.50001\}$

3.2 Comparison with an Analytical Solution

An analytical solution for a single fracture case was presented in Hægland et al. (2009) and corrected and extended in Sandve et al. (2012). It solves the equidimensional heterogeneity problem

$$\nabla \cdot (-\boldsymbol{K}(x,y) \nabla p(x,y)) = s(x,y) \tag{3.1}$$

with the additional requirements of pressure and flux continuity at the heterogeneity interface. The permeability tensors are given by

$$\boldsymbol{K}(x,y) = \begin{cases} \boldsymbol{K}_{\mathrm{m}} & (x,y) \in \Omega_{\mathrm{m}} \\ \boldsymbol{K}_{\mathrm{f}} & (x,y) \in \Gamma \end{cases}, \quad \boldsymbol{K}_{\mathrm{m}}(x,y) = \begin{pmatrix} c_{\mathrm{a}} & 0 \\ 0 & 1 \end{pmatrix}, \quad \boldsymbol{K}_{\mathrm{f}}(x,y) = k \cdot \boldsymbol{K}_{\mathrm{m}},$$

so that c_{a} is the anisotropy ratio in fracture and matrix and k is the heterogeneity ratio between the fracture and matrix. The source term is given by

$$s(x,y) = \begin{cases} (1-k)\cos(x)\cosh(d\sqrt{c_{\mathrm{a}}}/2) & (x,y) \in \Omega_{\mathrm{m}}, \\ 0 & (x,y) \in \Gamma. \end{cases} \tag{3.2}$$

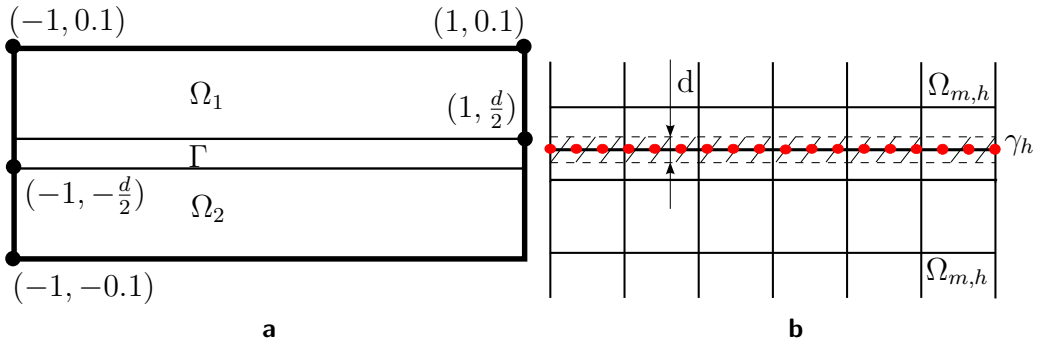

Figure 3.3: Continuous (left) and discrete (right) simulation domains

All boundary conditions are set to Dirichlet and are given by the analytical solution directly.

$$p(x,y) = \begin{cases} k\cos(x)\cosh(y\sqrt{c_\mathrm{a}}) + (1-k)\cos(x)\cosh(d\sqrt{c_\mathrm{a}}/2) & (x,y) \in \Omega_\mathrm{m}, \\ \cos(x)\ \cosh(y\sqrt{c_\mathrm{a}}) & (x,y) \in \Gamma. \end{cases} \tag{3.3}$$

The computational domain is chosen to be $\Omega = (-1,\, 1) \times (-0.1,\, 0.1)$. Looking only at the fracture domain, the correct solution can only be reproduced if the fracture gets the correct input from the matrix and thus, the matrix boundary. Therefore, in contrast to earlier comparisons, e.g., (Hægland et al. 2009, Sandve et al. 2012), the global domain is chosen much smaller in y-direction to exclude numerical errors coming purely from the matrix domain. The focus of this comparison lies on the coupling of fracture and matrix.

The fracture lies horizontally at $y = 0$ so that $\Gamma = (-1,\, 1) \times (-d/2,\, d/2)$ and the matrix domain follows $\bigcup_i \Omega_i = \Omega \backslash \bar{\Gamma}$, figure 3.3.

To show grid convergence and determine the accuracy order of the employed numerical scheme, traditionally global errors are calculated by means of area weighted $\mathcal{L}^2$-norms.

$$e = \frac{\left\| p^{\mathrm{h}} - p \right\|_{\mathcal{L}^2}}{\|p\|_{\mathcal{L}^2}} \approx \sqrt{\frac{\sum\limits_i a_{\mathrm{m},i}(p^{\mathrm{h}}_{\mathrm{m},i} - p_{\mathrm{m},i})^2 + \sum\limits_j a_{\mathrm{f},j}(p^{\mathrm{h}}_{\mathrm{f},j} - p_{\mathrm{f},j})^2}{\sum\limits_i a_{\mathrm{m},i}\, p^2_{\mathrm{m},i} + \sum\limits_j a_{\mathrm{f},j}\, p^2_{\mathrm{f},j}}}$$

The global error e consists of contributions from the fracture and the matrix. Every evaluation point i is associated to a surrounding area, e.g., if the area is evaluated at every node i, this area is defined by the connection of the midpoints of all edges connected to this node and the area barycenter of the elements sharing node i. If the node is part of $\partial\Omega$ the node itself is to be included in the connection of midpoints and barycenters.

In previous comparisons of fracture models such an error was used, but for the case of highly permeable fractures, which leads to a very large permeability ratio, the global error is totally dominated by the matrix contributions and the fracture part, which is where most of the flow happens, is almost canceled out because of the small area weighting. We can calculate the areas and estimate the pressures:

$$a_{\mathrm{m},i} = h_i^2, \quad a_{\mathrm{f},j} = h_j d_j, \quad p^2_{\mathrm{m},i} = \mathcal{O}(k)^2, \quad p^2_{\mathrm{f},j} = \mathcal{O}(1)$$

and under the assumptions of similar element lengths for fracture and matrix elements, i.e., $\mathcal{O}(h_{\mathrm{m}}) = \mathcal{O}(h_{\mathrm{f}})$ and approximately the same size for all elements, then the error reads:

$$e \approx \sqrt{\frac{\sum\limits_i (p^{\mathrm{h}}_{\mathrm{m},i} - p_{\mathrm{m},i})^2 + \frac{d}{h}\sum\limits_j (p^{\mathrm{h}}_{\mathrm{f},j} - p_{\mathrm{f},j})^2}{\sum\limits_i \underbrace{p^2_{\mathrm{m},i}}_{\mathcal{O}(k)^2} + \frac{d}{h}\sum\limits_j \underbrace{p^2_{\mathrm{f},j}}_{\mathcal{O}(1)}}}.$$

Normally, lower-dimensional models are only used in situations when d is very small and we still have a grid where $\mathcal{O}(h) > \mathcal{O}(d)$. The fracture error now has to be (h/d)-times larger than the matrix error to show a significant contribution to the global error.

Table 3.1: Order of global error, e_g, convergence between level ℓ and level $\ell - 1$, element size is given by $h_\mathrm{f} = 2.0/2^\ell \approx h_\mathrm{m}$, aperture is fixed at $d = 10^{-6}$

$\ell \setminus k$	10^4	10^1	10^0	10^{-1}	10^{-4}
6	1.13	2.66	2.87	3.60	1.98
7	1.21	3.09	3.82	3.31	1.99
8	2.25	3.86	3.84	2.38	1.99
9	2.64	3.36	3.05	2.04	1.98
10	3.37	2.46	2.15	1.93	1.93

We therefore look at the matrix and the fracture error separately and define the global error as the sum of the individually weighted and normalized errors.

$$e_\mathrm{g} = e_\mathrm{m} + e_\mathrm{f}, \quad e_\mathrm{m} = \frac{\left\| p_\mathrm{m}^\mathrm{h} - p_\mathrm{m} \right\|_{\mathcal{L}^2}}{\|p_\mathrm{m}\|_{\mathcal{L}^2}}, \quad e_\mathrm{f} = \frac{\left\| p_\mathrm{f}^\mathrm{h} - p_\mathrm{f} \right\|_{\mathcal{L}^2}}{\|p_\mathrm{f}\|_{\mathcal{L}^2}}$$

In the following calculations the anisotropy is set to one, $c_\mathrm{a} = 1$. For a fixed aperture $d = 10^{-6}$ and varying k, figures 3.4a and 3.4b show the fracture and matrix error. For this case almost optimal order of convergence is shown in table 3.1. The matrix element size is not exactly but only approximately the same as the fracture element size so that always a non-conforming situation occurs.

Remark 1. To also capture the quality of our implemented version of the XFEM, the errors are not only evaluated at the nodes but at all points of a high order Gauss integration rule.

Remark 2. In our method the fracture domain is discretized with lower dimensional elements, Γ_h. The discretized matrix domain covers the same global area Ω, but because of the line elements for the fracture γ in the global space, cf. figure 3.3, the discretized matrix domain is larger than the continuous (equidimensional) matrix domain given by the problem definition, $|\Omega_\mathrm{m,h}| > |\cup_i \Omega_i|$. This introduces an error which corresponds to the artificial additional area in the discretized matrix domain with the size of $|\Gamma|$. The source term is not evaluated in this region of the matrix elements and the error is also not calculated in this region.

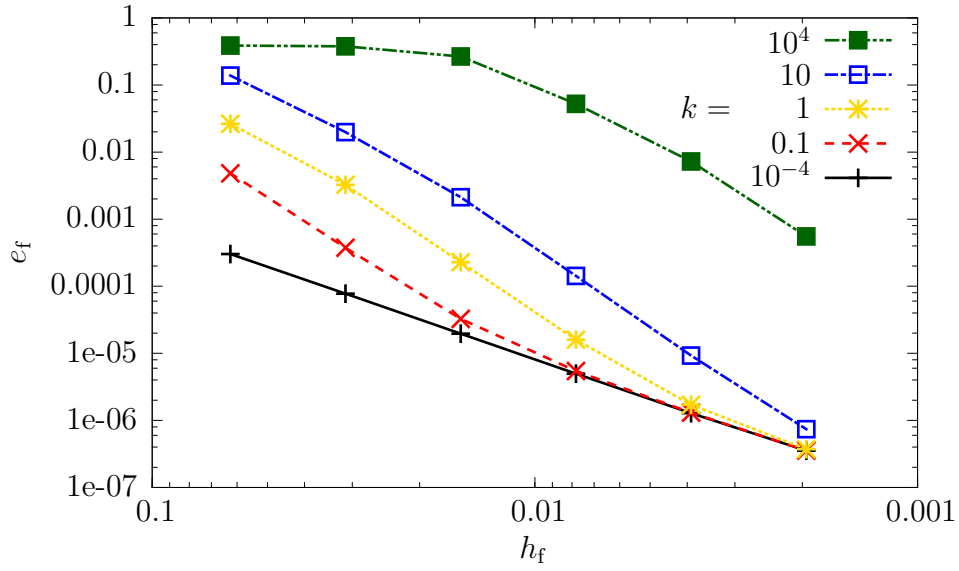

a fracture error e_f

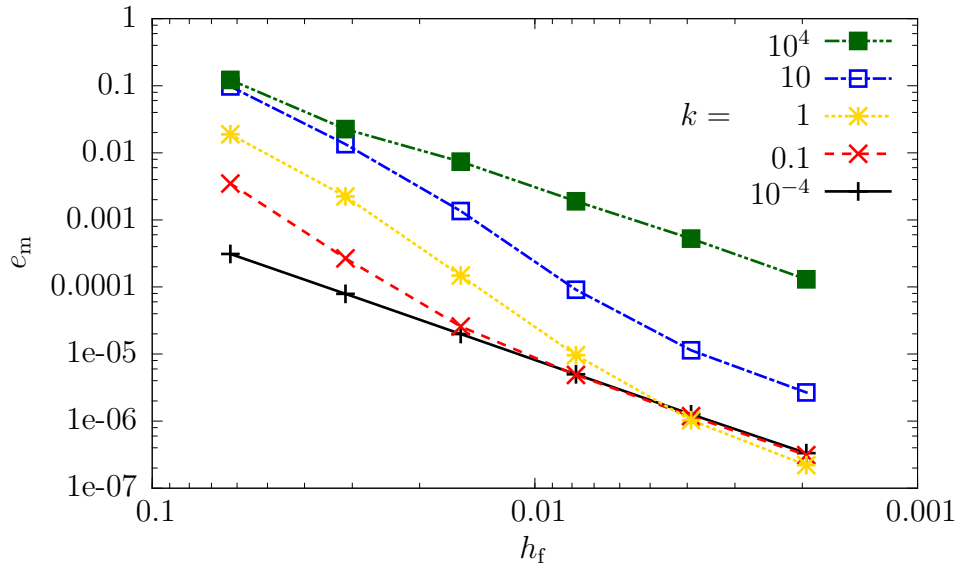

b matrix error e_m

Figure 3.4: Error plots for global refinement, fixed aperture $d = 10^{-6}$ and matrix permeability $\boldsymbol{K}_\mathrm{m} = \mathbf{I}$ (no anisotropy), varying fracture permeabilities k

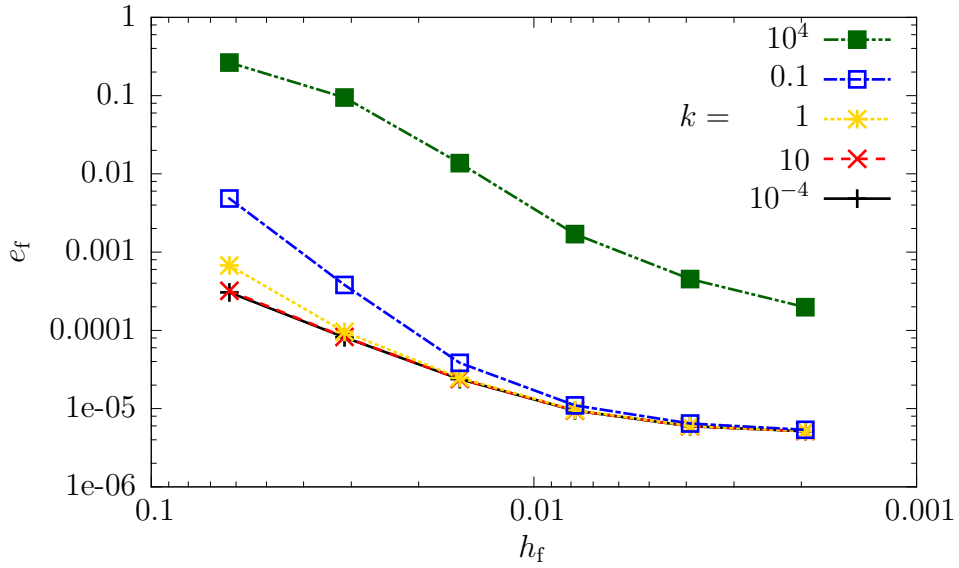

Figure 3.5: Fracture error e_f for global refinement, fixed aperture $d = 10^{-4}$ and matrix permeability $\boldsymbol{K}_m = \mathbf{I}$ (no anisotropy), varying fracture permeabilities k

Increasing the fracture aperture, the error seems to stagnate at a level too high to be caused by machine precision errors and the error does not show optimal convergence for highly permeable fractures. For an aperture of $d = 10^{-4}$ this can be seen for the fracture error in figure 3.5. The matrix error shows similar behavior, (Oueslati 2013). An aperture of $d = 10^{-5}$ does not show this stagnation effect but rather optimal convergence in the same range of h_f as for an aperture of $d = 10^{-6}$.

This is probably an effect of the ratio of matrix element size to virtual fracture area inside one matrix element. For the aperture of $d = 10^{-4}$ the optimal convergence is lost at approximately $h_m \approx 0.004$ which means $\approx 2.5\%$ of a matrix element would actually be covered by the fracture.

To absolutely exclude errors caused by machine precision, simulations were carried out with quadruple precision. Figure 3.6 shows that the increased quadruple precision produces the same error as for standard (double) precision. For this tests, iterative solvers were used. They showed the same results as the double precision direct solver so that a quadruple precision direct solver did not had to be tested. A BiCGStab (bi-conjugate gradient stabilized method) solver with ILU0 (zero fill in incomplete

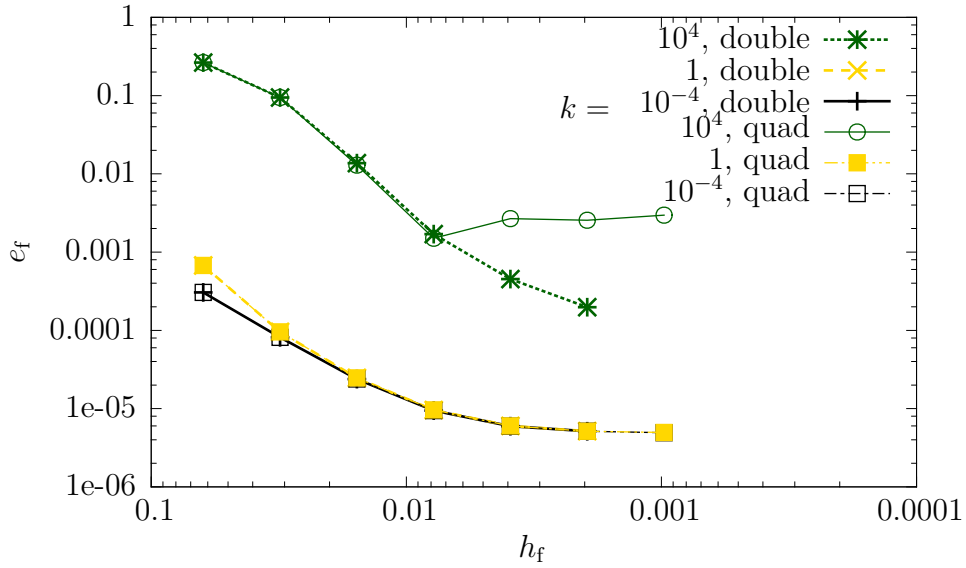

Figure 3.6: $d = 10^{-4}$, fracture error e_f, double (direct) vs. quad precision (iterative)

Cholesky factorization) and SSOR (Symmetric Successive Over-Relaxation) preconditioners and a MinRes (minimum residual) solver preconditioned with SSOR, were tested, all with the same result. For a fine grid they do not converge anymore.

To check the influence of the source term on the coupling and convergence behavior an alternative analytical solution was tested, (3.4), with a source term which is zero in the matrix domain and not-zero in the fracture domain, (3.5).

$$p = \begin{cases} \cos(x)\cosh(y) & (x,y) \in \Omega_m \\ \frac{1}{k}\cos(x)\cosh(y) + (1-\frac{1}{k})\cos(x)\cosh(\frac{d}{2}) & (x,y) \in \Gamma \end{cases} \tag{3.4}$$

$$s(x,y) = \begin{cases} 0 & (x,y) \in \Omega_m \\ (1-\frac{1}{k})\cos(x)\cosh(\frac{d}{2}) & (x,y) \in \Gamma \end{cases} \tag{3.5}$$

This alternative analytical solution shows a very similar convergence behavior so that an error in the source term can be ruled out.

3.3 Summary and Outlook

The influence of the averaging parameter was tested and the results show that its influence is negligible, but for reasons of stability and robustness it should be chosen not close to its lower limit.

The XFEM implementation for a single horizontal fracture is compared against an analytical solution for different apertures and permeability ratios. Optimal convergence is shown for all permeability ratios if the fracture domain covers less than $\approx 2.5\%$ of the area of the matrix elements in which the fracture is embedded. Sequential solvers in the current implementation do not converge for highly conductive fractures on a fine grid. There exists potential for improvement.

4 Ending Fractures

In this chapter two major aspects are discussed. The first is about the XFEM for ending fractures and the second about the coupling concept at the tip of a fracture.

4.1 XFEM for Ending Fractures

If a fracture ends within a matrix element, the fracture is virtually extended in tangential direction until an edge of this element is reached. This is called "projected intersection". As presented in section 2.5.1 and shown in figures 2.10 and 2.11 **e**, there exist two cases for the implementation of ending fractures in the XFEM; in relation to the cut edge, the projected intersection of the fracture with the matrix element is on the opposite or on a neighboring matrix element edge.

The XFEM implementation for the case of a projected intersection on an opposite edge than the cut edge is straightforward. The degrees of freedom on the cut edge are enriched and the previously introduced discontinuity functions are used for standard and enriched degrees of freedom. The other two degrees of freedom, on the edge cut by the virtually extended fracture, are not enriched and therefore no discontinuity functions are used on the standard basis. That leads to a continuous solution at the projected intersection point and a possible bi-linear increase of the solution jump towards the entry point. If there is a jump at the real intersection, there will be also a jump across the virtual fracture part. This cannot be avoided in the current implementation and the error made because of this implementation enters the total error seen in the examples.

The coupling conditions are only evaluated across the real part of the fracture. The fracture length and position inside the matrix element have a significant influence on the total system which is not neglected, i.e., the coupling across the fracture is carried out exactly.

If the projected intersection is on a neighboring edge to the cut edge, the jump is in general not only on the virtual path of the fracture not zero, but also not zero on the virtually intersected edge. In the simulations carried out in the context of this project the same treatment is applied independent whether the projected intersection lies on a neighboring or opposite edge with respect to the cut edge. This did not lead to stability problems or obvious, visibly wrong solutions and is thus assumed to be negligible.

4.2 Fracture Tip – Rock Matrix Coupling

The fracture tip is hard to simulate efficiently even for equidimensional models. There are several approaches to handle fracture tips from the conceptual point of view as well as the numerical point of view. The tip treatment for several numerical methods is discussed for example in Neunhäuserer (2003), but there, the fracture is resolved with only one element in its normal direction.

Because for lower dimensional models the thickness is already assumed to be very small in comparison to the lateral extension of the fracture, Angot et al. (2009) assumed that there is no relevant flow contribution in lateral fracture direction across the, in the limit, zero thickness fracture tip.

In contrast to the no-flow assumption of Angot et al. (2009), the XFEM model assumes that there is a non-zero flux across the fracture tip. For the coupling of that flow across the fracture tip, the discrete node at the tip is treated as an internal node with an occurring, but unknown, Neumann flow. This flow is used as a source term in the matrix element which includes the tip,

$$\boldsymbol{u}_{\mathrm{f,t}} d|_{\boldsymbol{x}_{\mathrm{tip}}} = s_{\mathrm{m,tip}}. \tag{4.1}$$

The XFEM implementation of the lower-dimensional model presented here is compared against two models presented in Angot et al. (2009), a two-point flux cell centered finite volume method (CCFV) and a mimetic finite difference method (MFD) which is assumed to give a reference solution. Both, CCVF and MFD, are used as they are implemented in DuMu$^{\mathrm{x}}$.

It is a well-known fact that the two-point flux model is in general only able to simulate flow on k-orthogonal grids correctly. This was also the case in the examples presented here. The influence of the error through the grid was significant and dominated the total solution. Thus, the CCFV with two-point flux is not used as reference but only the MFD results on structured quadrilateral as well as unstructured simplex grids.

4.3 Example 1: Single Fracture Tip

This example is taken from Angot et al. (2009) where it is the third test in section 5.2. It was also simulated in Meyer (2014). It contains a single fracture with an aperture of $d = 0.01$. The matrix permeability is the unit tensor $\boldsymbol{K}_{\mathrm{m}} = \mathbf{I}$. The fracture is permeable in tangential and normal direction $k_{\mathrm{f,t}} = k_{\mathrm{f,n}} = 10^2$. The boundary conditions are Neumann no-flow on bottom and top except for the fracture, where a Dirichlet pressure of $\bar{p}^{\mathrm{D}} = 2$ is given. On the matrix a global pressure gradient is imposed by applying Dirichlet pressure on the left $\bar{p}^{\mathrm{D}} = 1$ and on the right $\bar{p}^{\mathrm{D}} = 2$, cf. figure 4.1.

The XFEM implementation is compared against a fine grid solution obtained from an equidimensional model discretized with MFD. This is assumed to be the correct solution and used as reference. In Angot et al. (2009) two models were proposed and simulated. There is no visual difference between the solutions of those two models. The asymptotic model uses 16364 control volumes, the assumed to be converged

solution of XFEM use 2833 degrees of freedom. Already a XFEM solution on a grid with 525 degrees of freedom shows a sufficiently good approximation of the matrix pressure and the pressure inside the fracture. However, to capture the fracture tip pressure sufficiently, the aforementioned finer grid is needed.

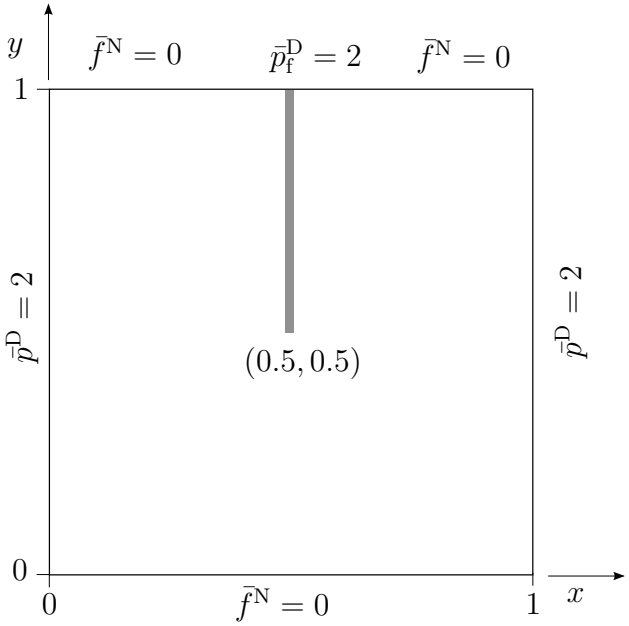

Figure 4.1: Single fracture tip domain and boundary conditions

The pressure contour distribution is shown in figure 4.2 for the reference MFD solution with the grid and for the XFEM implementation including pressure iso-lines. Pressure plots along two different cut-lines for the MFD and the XFEM models and the models from Angot et al. (2009), figure 4.3, also do not show any obvious differences.

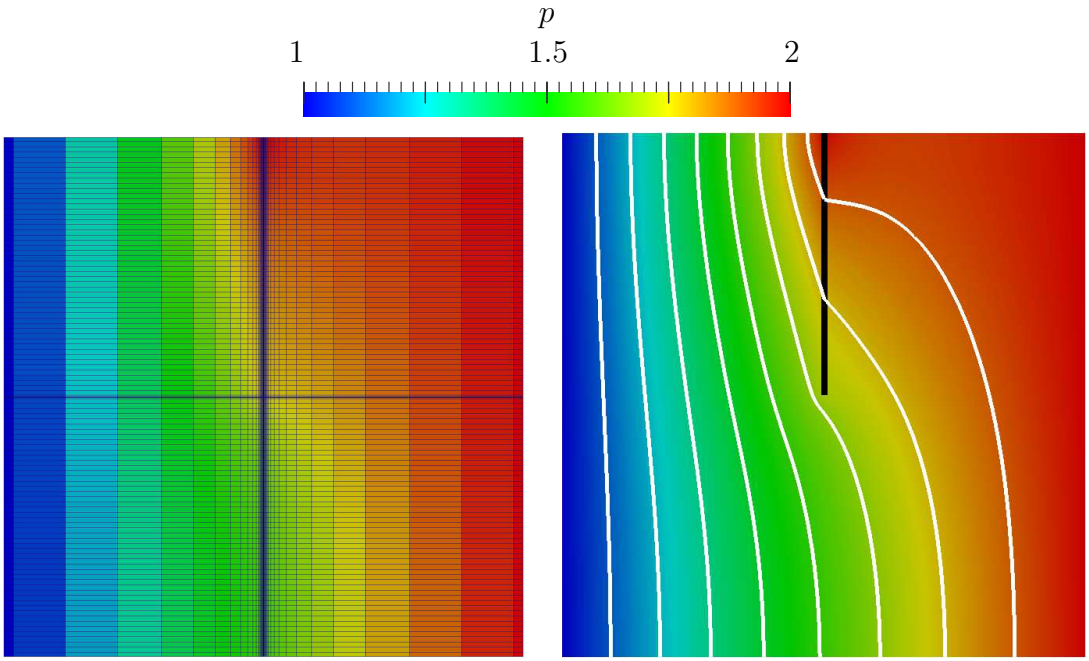

a MFD with grid: 10 elements in fracture normal direction, at the tip quadratic elements, increasing in size away from fracture and tip

b XFEM with pressure iso-lines

Figure 4.2: Single fracture tip: Pressure distribution

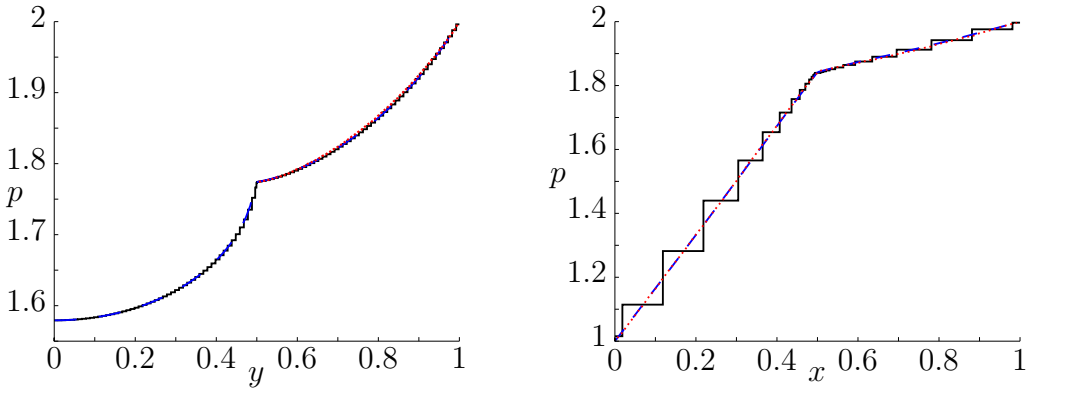

a along the fracture for constant $x = 0.5$

b along horizontal line for constant $y = 0.75$

Figure 4.3: Single fracture tip: Pressure along cut-lines; red-dotted Angot et al. (2009), black-solid equidimensional MFD, blue-dashed XFEM

4.4 Example 2: Multiple Fracture Tips

This example is taken from Angot et al. (2009) where it is the third test in section 5.4. It was also simulated in Meyer (2014). It contains four fractures with an aperture of $d = 0.01$. The two fractures entering the domain from the left are almost impermeable in tangential and normal direction $k_{\mathrm{f,t}} = k_{\mathrm{f,n}} = 10^{-2}$. The other two fractures, entering the domain from the right, are almost impermeable only on normal direction $k_{\mathrm{f,n}} = 10^{-2}$, but conductive in tangential direction $k_{\mathrm{f,t}} = 10$. The matrix permeability is the unit tensor $\boldsymbol{K}_{\mathrm{m}} = \mathbf{I}$.

The boundary conditions are Dirichlet everywhere, constant on left and right boundary, $\bar{p}^{\mathrm{D}} = 1$ and $\bar{p}^{\mathrm{D}} = 2$ respectively and quadratic on top and bottom $\bar{p}^{\mathrm{D}} = (2x - 1)(3x - 1)$, cf. figure 4.4.

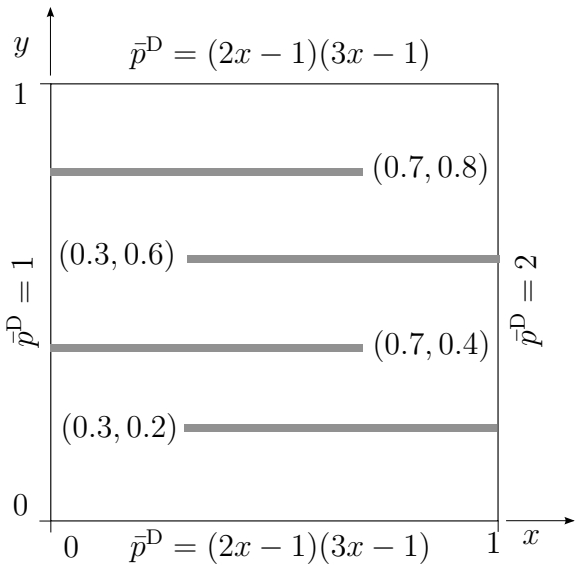

Figure 4.4: Multiple fracture tips domain and boundary conditions

Remark 1. Keep in mind that the boundary conditions presented here might not reflect a physical situation because the used pressure scaling, cf. section 2.6, does not involve a shift with respect to a reference pressure, i.e., negative pressure would not exist. Nevertheless this example shows the robustness of the implementation and allows a comparison against literature results.

Four different models are compared. The reference solution is given on a structured quadrilateral grid, refined in the fractures and fracture tips with 136881 control volumes and computed with an MFD method. The literature reference is taken from an equidimensional, so called "global Darcy", model with 201704 control volumes and a lower-dimensional, "asymptotic", model with 25600 control volumes from Angot et al. (2009). The fourth model is the XFEM model which has 236 degrees of freedom. The MFD and the XFEM models were also simulated with finer grids and the coarsest grid with an assumed to be converged solution are picked for the visualization and comparison.

The pressure contour distribution is shown in figure 4.5 for the reference MFD solution with the grid and for the XFEM implementation including pressure iso-lines.

Pressure plots along two different cut-lines for MFD, XFEM and Angot et al. (2009), do not show any obvious differences for the pressure in the matrix, cf. figure 4.6a. The results from Angot et al. (2009) cannot be used as comparison because obviously the results are wrong – they do not match the Dirichlet boundary conditions.

The fracture pressures match nicely for the MFD and XFEM models for the fractures entering the domain from the left, which are in tangential and normal directions almost impermeable, figure 4.6b. The asymptotic (lower-dimensional) model and the global Darcy model (equidimensional) from Angot et al. (2009) match each other but are visually different to the MFD reference solution.

The fracture pressures for the fractures entering the domain from the right, which are only in normal direction almost impermeable but in tangential direction permeable, do not match, figure 4.7. As already discussed in Angot et al. (2009), their asymptotic model fails to capture the boundary correctly and also shows significant differences to their global Darcy model along the fracture, except for the fracture tip, where the pressures match. Nevertheless there exists a significant difference to the MFD reference solution for the XFEM model, too. The Angot et al. (2009) models seem to underestimate the pressure where the XFEM model overestimates it.

The error made with the XFEM model seem to have no visible effect on the matrix solution. In total the XFEM model needs a lot less computational time to create the

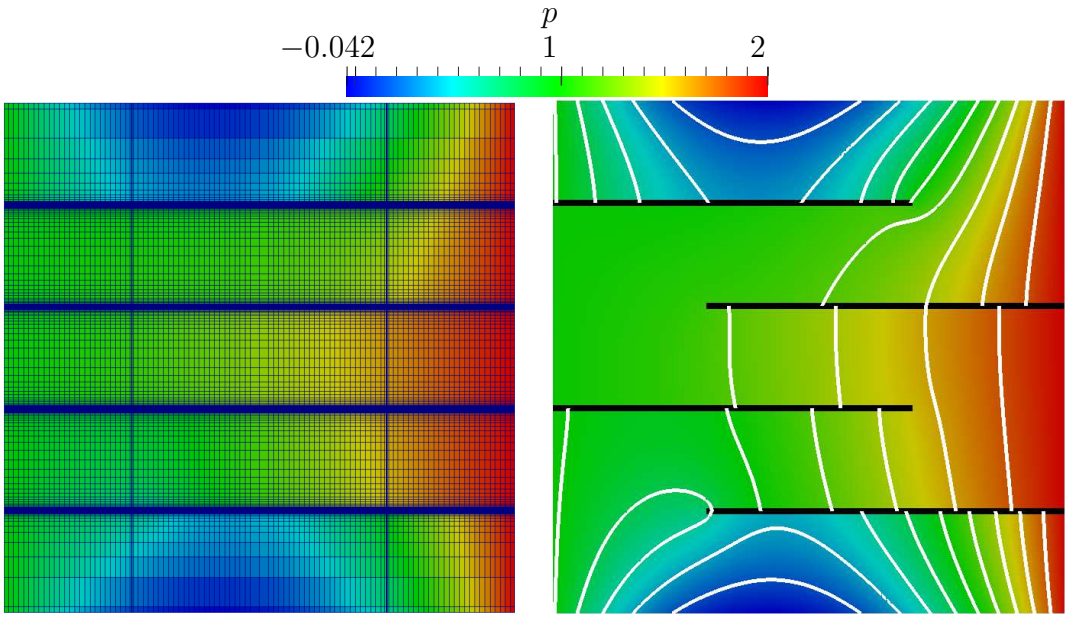

a MFD with grid **b** XFEM with pressure iso-lines

Figure 4.5: Multiple fracture tips: Pressure distribution

grid and to solve the problem with at some points better agreement to the reference than the Angot et al. (2009) model and at other points an error in the same order of magnitude as the asymptotic literature reference model.

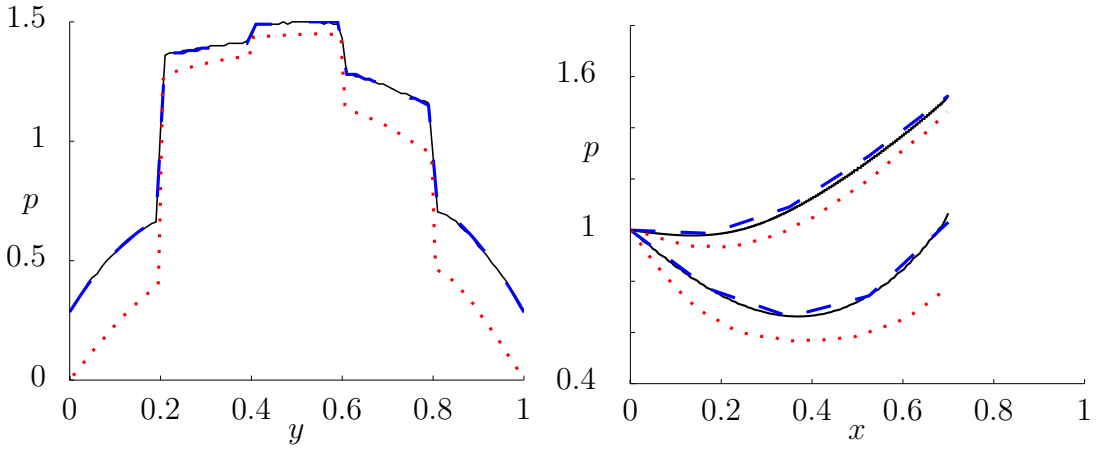

a along vertical line for constant $x = 0.65$

b Pressure along the fractures from the left, $y = 0.4$ and $y = 0.8$

Figure 4.6: multiple fracture tips: Pressure along cut-lines; red-dotted asymptotic model from Angot et al. (2009), black-solid equidimensional MFD, blue-dashed XFEM

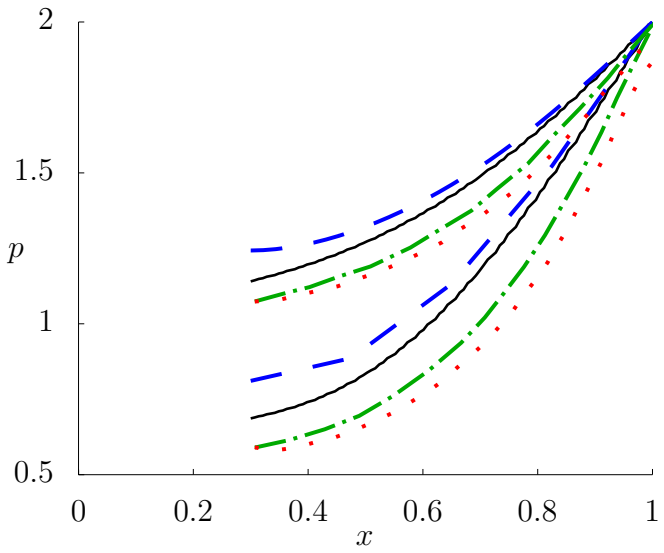

Figure 4.7: pressure along the fractures from the right, $y = 0.2$ and $y = 0.6$, multiple fracture tips: Pressure along cut-lines; red-dotted asymptotic model from Angot et al. (2009), green-dash-dotted equidimensional model from Angot et al. (2009), black-solid equidimensional MFD, blue-dashed XFEM

4.5 Summary and Outlook

The XFEM model is able to reproduce the reference solution. The grid creation is carried out with almost no computational efforts. This is an efficiency advantage which strongly depends on the complexity of the fracture network. For the academic examples presented above, however, it is not measurable. Furthermore a reduction in degrees of freedom between a factor of ≈ 5 for the single fracture model to ≈ 100 for the multiple fracture model was possible to receive visually the same results.

The case of fractures permeable in tangential and almost impermeable in normal direction shows significant differences between all the compared models and thus, there is space for improvement also in the tip treatment of the XFEM model.

The case of a projected intersection edge neighboring a real intersection edge and the corresponding implementation can be investigated further and the error quantified. A possible enrichment alternative might be to enrich only the node which lies on the real intersection edge but not on the projected intersection edge.

Another coupling concept for the fracture tip could be a coupling of pressures directly, a Dirichlet-Dirichlet coupling, where the pressure at the fracture tip is set to be equal to the average pressure of the matrix,

$$p_{\mathrm{f}}(\boldsymbol{x}_{\mathrm{tip}}) = \{\!\{ p_{\mathrm{m}}(\boldsymbol{x}_{\mathrm{tip}}) \}\!\}. \tag{4.2}$$

An ad-hoc implementation of this alternative coupling concept does not produce reasonable results and thus, it remains future work.

Remark 1. In isotropic structural mechanics problems the XFEM is used for fracture tip treatment. The enriched basis is here not simply a standard basis with a discontinuity function but instead a radial basis is used. It has to be shown that this is also a valid approach for flow problems and an extension to orthotropic or even anisotropic problems has to be made.

5 Fracture Crossings

Bibliographic Note: This chapter is based on: *Schwenck, N., Flemisch, B., Helmig, R., and Wohlmuth, B. I. (2014). Dimensionally reduced flow models in fractured porous media: Crossings and boundaries.* Submitted and NUPUS preprint 2014/5.

From the applicational point of view, a crossing is assumed to be a heterogeneity of several (≥ 2) fracture branches, with possibly different permeabilities, intersecting. In general, there exist several possibilities to model such fracture crossing areas. Classical approaches for heterogeneity interfaces are usually based on averaging schemes. Looking at an equidimensional crossing with, for example, four fracture branches with arbitrary permeability each, the average permeability for the crossing would depend on four different, possibly full tensor, permeabilities. To find an average permeability for this situation which captures the important flow features, is not easy. In general, the problem for tensorial permeabilities is, the absolute mean permeability should be dominated by the lowest permeability but the mean direction should be dominated by the highest permeability, so that harmonic mean approaches for a permeability tensor, defined as the harmonic mean of the entries, can give wrong flow directions. It is, however, still possible to define an averaged permeability tensor by solving some kind of upscaling equations, cf. e.g., (Wen et al. 2003, Wolff 2013).

For lower dimensional fractures, the pressure is usually defined as the average pressure in normal direction for every point in the tangential direction of the fracture. The fracture local coordinates ξ, η, define the tangential and normal direction of the fracture, (5.1). Every fracture is thus defined by a center line with a

(possibly varying) thickness and associated properties such as normal and tangential permeabilities. Such fractures of co-dimension one, $\gamma_j \subset \mathbb{R}^{n-1}$, define a network of fractures as a set of discrete lines $\gamma = \cup_j \gamma_j$.

$$p_{f_i}(\xi) = \frac{1}{d_i(\xi)} \int_{-d_i/2}^{+d_i/2} p_i(\xi, \eta) \, d\eta \tag{5.1}$$

In a crossing, however, the different properties of every fracture branch can overlap and a unique association of properties is not always possible, so that, in general, new properties have to be defined especially for the crossing area. This is in fact also a requirement from the physical point of view. If there is a crossing of fractures with very different permeabilities, one fracture always dominates a crossing from a geological point of view. For example, if there exists a highly permeable fracture which becomes intersected over time by an almost impermeable fracture, the crossing's permeability is more likely to be almost impermeable than highly conductive or averaged. It is then neither a good idea to always average the permeabilities in a crossing nor to neglect the connection between different fractures.

In contrast to an averaging approach, in the model presented here the permeability for the crossing region is assumed to be given as input parameter for this area which might differ from the surrounding fractures. This is a reasonable assumption since permeabilities, thickness and position of the fractures are also given.

The flow through such a crossing of fractures, with possibly very different physical parameters in a global coordinate system, is not at all trivial and classical models are not always able to capture the important flow features correctly or lack numerical stability, e.g., the standard model in Formaggia et al. (2012) or Section 6.2 in Neunhäuserer (2003).

In Formaggia et al. (2012), a model for two straight intersecting fractures is introduced. This section proposes an alternative, new methods to handle arbitrary numbers (≥ 2) of fracture branches which end in the same point. Starting at an equidimensional crossing with the equidimensional fracture branches Γ_i, pressure relations in the lower-dimensional model are derived for all fracture branches γ_i

and the crossing, Υ. The presentation of the method is here limited to the two-dimensional case. The extension to three dimensions for co-dimension one fractures might not be straightforward.

In the equidimensional model a crossing can have almost arbitrary shapes. One approach to handle such a crossing in an equidimensional sense is to introduce a virtual finite element with a complex shape and therefore basis. Another approach is to derive an algebraic expression which gives a relation between the adjacent fracture pressures. Such algebraic expressions are presented in the following.

5.1 Conceptual Model

An example of a crossing is shown in figure 5.1. The equidimensional model domain

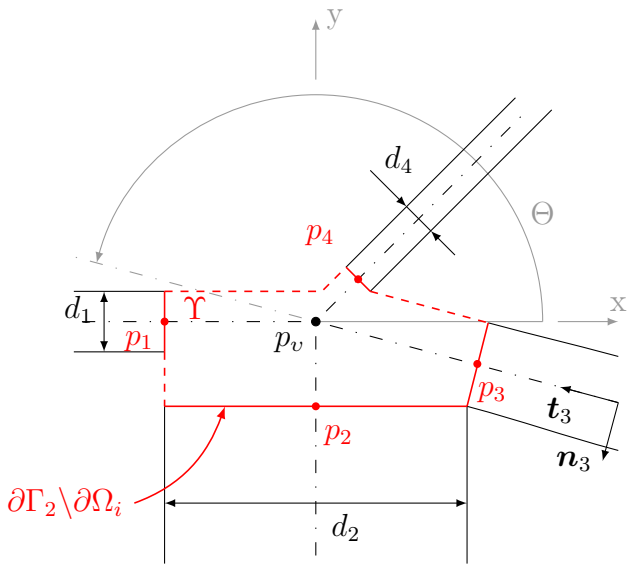

Figure 5.1: Example 4-crossing with intersection geometries and location of pressure unknowns in the equidimensional model

can now be decomposed into three different domain types: Matrix, fracture and crossing, $\Omega = \left(\bigcup_i \Omega_i\right) \cup \left(\bigcup_i \Gamma_i\right) \cup \Upsilon$. We define the crossing area Υ with boundaries to the fractures $(\partial\Upsilon)_{\mathrm{f},i} \coloneqq \partial\Gamma_i \cap \partial\Upsilon$ (solid red lines) and boundaries to the rock matrix $(\partial\Upsilon)_{\mathrm{m}} \coloneqq \partial\Upsilon \backslash (\bigcup_i \partial\Gamma_i)$ (dashed red lines). The intersection of the fracture center

lines is denoted by υ. Capital Greek letters indicate areas in the equidimensional model, small Greek letters indicate dimensionally reduced areas.

With the crossing area defined, figure 5.1, we introduce an additional degree of freedom, the pressure at the intersection of the fracture center lines, p_υ. Introducing

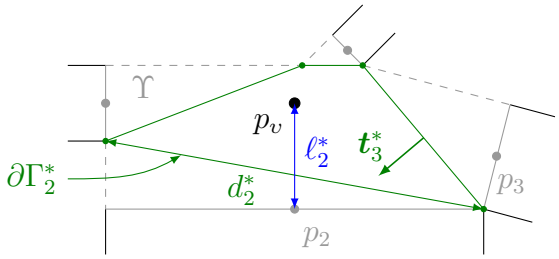

Figure 5.2: Example 4-crossing with definition of geometrical parameters inside the crossing area

the green boundaries in figure 5.2, we get a closed control area for which we can write down the mass conservation equation which gives a relation between the crossing area pressure and the adjacent fracture pressures p_i.

The superscript $(\cdot)^*$ denotes values which are inside Υ, i.e., d_i^* is the length of the interface between fracture i and Υ, $\boldsymbol{t}_i^*$ is the unit inward normal vector of fracture i on $\partial\Gamma_i^*$. The distance between the crossing point υ and the center of $\partial\Gamma_i$ for every fracture is denoted by ℓ_i^*. The classical mass conservation without sources or sinks for a steady-state situation for the crossing area $\int_{\partial\Upsilon} \boldsymbol{u}\cdot\boldsymbol{n}\,\mathrm{d}\boldsymbol{s} = 0$ can be written as the sum of the normal fluxes across each fracture boundary to the inner crossing area, $\sum_{i=1}^{\mathrm{n_f}} f_i^* = 0$. Here, $\mathrm{n_f}$ is the number of fracture branches connected to this crossing. The normal flux is defined as $f_i^* = \int_{\partial\Gamma_i} \boldsymbol{u}_{i,\Upsilon}^* \boldsymbol{t}_{i,\Upsilon}^*\,\mathrm{d}\boldsymbol{s}$ for every fracture i. Using the Darcy closure, $\boldsymbol{u}_i^* = -\boldsymbol{K}_\Upsilon(\nabla p_i)_\Upsilon$, to eliminate the velocities leads to

$$\sum_i \left[(-\boldsymbol{K}_\Upsilon(\nabla p_i)_\Upsilon)\,\boldsymbol{t}_i^*\right] d_i^* = 0\,. \tag{5.2}$$

To incorporate this continuous mass conservation equation into our flow fracture model, we need to discretize it. Because we want to get an explicit expression for the pressures, we need to approximate the gradient.

The rotation matrix $\boldsymbol{R}(\theta) = \begin{pmatrix} \cos(\theta) & -\sin(\theta) \\ \sin(\theta) & \cos(\theta) \end{pmatrix}$ is defined as the transformation (rotation) from local fracture coordinates into the reference coordinate system where the tangential vector is the first axis (x) and points towards the crossings center. The pressure gradient in the fracture, however, is in our lower dimensional model defined as the finite difference along the tangential fracture direction, because we only know one average pressure and not a variation of pressure in fracture normal direction. That means

$$(\nabla p_i)_{\Upsilon} = \boldsymbol{R}(\theta_i)\,[(\nabla p_i)_{\Upsilon}]_{\mathrm{f},i} = \boldsymbol{R}(\theta_i) \left[\begin{pmatrix} \frac{p_\upsilon - p_i}{\ell_i^*} \\ 0 \end{pmatrix} \right]_{\mathrm{f},i} \tag{5.3}$$

approximates the gradient in global coordinates dependent on the local fracture gradient and the orientation θ of the fracture. We can now write the compatibility equation as

$$\sum_i \left\{ \left(-\boldsymbol{K}_{\Upsilon} \left(\boldsymbol{R}(\theta_i) \left[\begin{pmatrix} \frac{p_\upsilon - p_i}{\ell_i^*} \\ 0 \end{pmatrix} \right]_{\mathrm{f},i} \right) \right) \boldsymbol{t}_i^* \right\} d_i^* = 0\,. \tag{5.4}$$

This approximation of the pressure gradient is exact (in the context of the fracture normal averaged pressure) inside the respective fracture branch. Inside Υ the global pressure gradient possibly varies in space and is dependent on all adjacent averaged fracture pressures. Thus, our approach is an approximation of this complex dependency.

Remark 1. In the case of four fractures with the same aperture intersecting at 90 degrees, figure 5.3 left, the red and green lines fall together. This does not pose any problem for this approach.

Remark 2. The case of two parallel fractures with different aperture intersecting, figure 5.3 right, cannot be handled with this approach because the crossing area Υ shrinks to a line and all three pressures p_1, p_2, p_υ are located at the same geometrical position in the equidimensional domain.

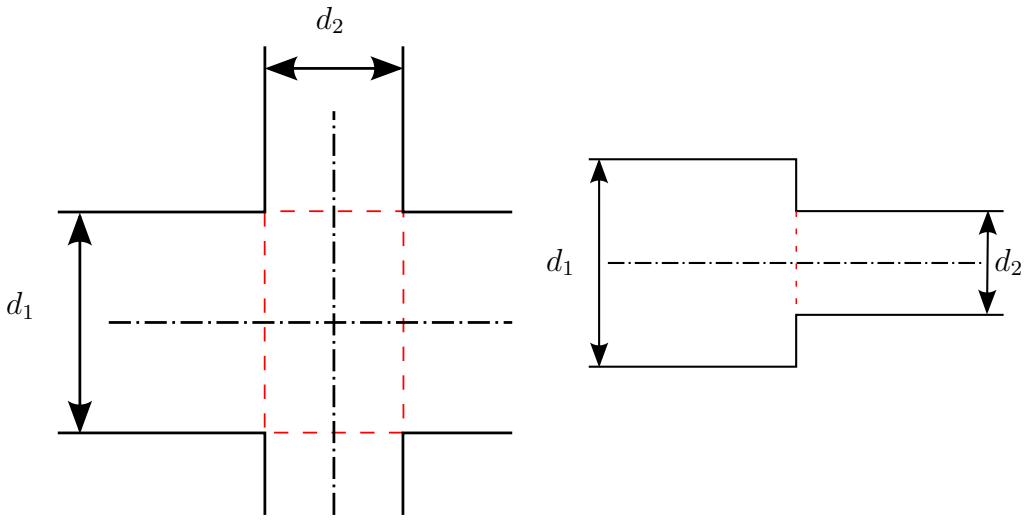

Figure 5.3: Two special crossing cases. Left: Four fractures intersecting 90 degrees, which is not a problem for the proposed method. Right: Two parallel fractures with changing aperture, which cannot be handled by the proposed method.

5.2 Validation Approach: Comparison Against Equidimensional Reference

In this section a simple crossing of four fracture branches, two straight horizontal and two straight vertical, crossing in the middle of the domain, is analyzed and compared against an equidimensional solution obtained with an MPFA-O CCFV method which was computed with DuMu$^{\text{x}}$. The domain is the unit square with Dirichlet boundary conditions on the left and right and between $0.3 \leq x \leq 0.7$ on top and bottom. The rest is closed with Neumann no flow conditions, figure 5.4a. The matrix permeability is the unit tensor $\boldsymbol{K}_{\text{m}} = \mathbf{I}$, the horizontal fracture is conductive $k_{\text{f,n}} = k_{\text{f,t}} = 100$, where the vertical fracture is almost impermeable in normal direction $k_{\text{f,n}} = 10^{-4}$, but even higher permeable than the horizontal fracture in tangential direction $k_{\text{f,t}} = 10^4$. The fracture crossing has the same permeabilities as the horizontal fracture, $k_{\text{x}} = k_{\text{y}} = 100$.

The XFEM solution is obtained from a grid with 750 degrees of freedom whereas the reference solution is computed on a very fine grid which resolves each fracture in normal direction with 39 control volumes and contains in total 23409 control

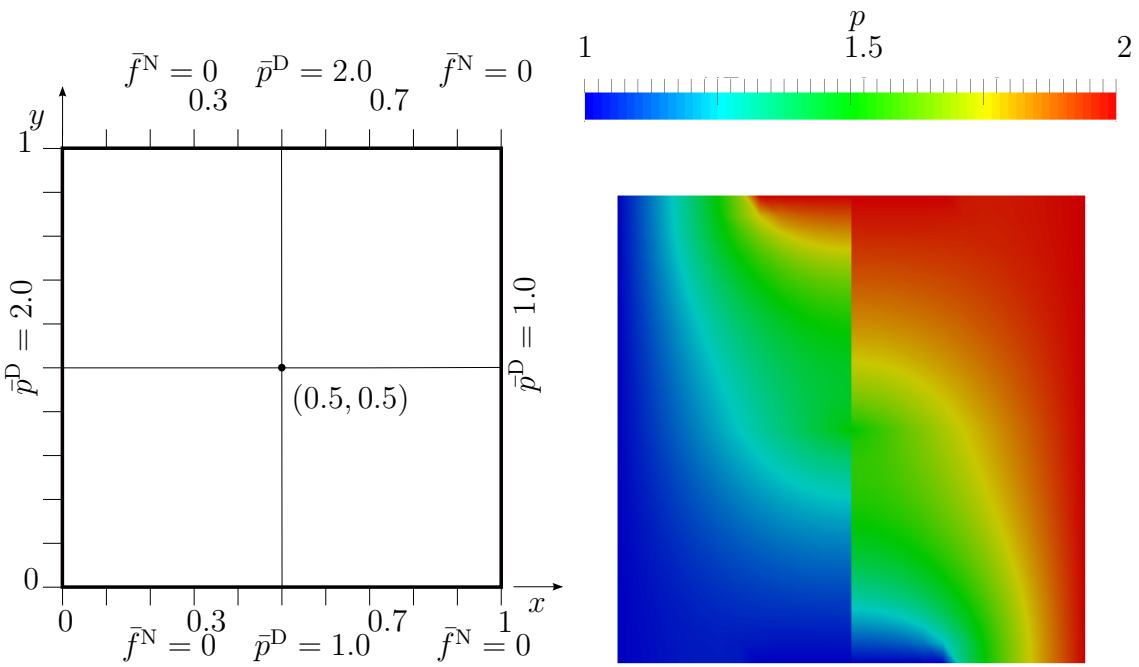

a domain and boundary conditions

b XFEM pressure solution

Figure 5.4: Simple crossing

volumes. The pressure distribution in the whole domain obtained with the XFEM implementation is shown in figure 5.4b.

Pressure plots along cut-lines are shown in figures 5.5a, 5.5b, 5.6a and 5.6b for $y = 0.5$ and $x = 0.5$, i.e., along the fractures, and $y = 0.25$ and $x = 0.25$, i.e., through the matrix, respectively. For all cases the XFEM solution matches the assumed reference MPFA solution quite well.

Two important flow field features are also well captured by the reduced model. The pressure along the horizontal cut-line at $y = 0.25$, figure 5.5a, is non monotone because of the heterogeneity (the fracture). This is the expected, physical flow behavior, because the main flow occurs in fracture direction. The XFEM solution with its solution on two different grids can reproduce this behavior. It underestimates the fracture pressure a little. The second, important flow feature is the continuity of pressure in equidimensional models, which leads to pressure discontinuities in lower-dimensional models. A zoom in the crossing region of the fracture pressure plot figure 5.6a is shown in figure 5.7. That zoomed plot shows the pressure

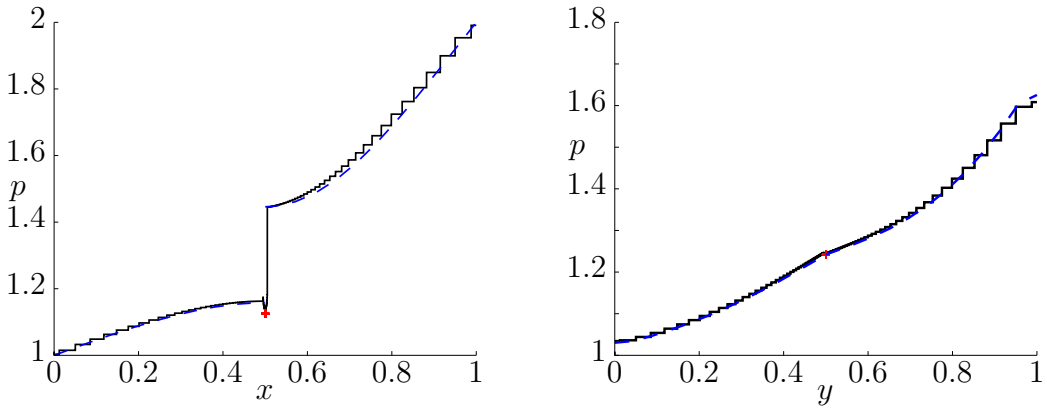

a horizontal line $y = 0.25$ **b** vertical line $x = 0.25$

Figure 5.5: Simple crossing: Pressure plots along cut-lines; black-solid line: Reference MPFA solution, blue-dashed line: Reduced XFEM model, red: Reduced model fracture solution

jump in the lower dimensional model and compares it to the virtual pressure jump of the equidimensional model across the heterogeneity. The jump is a little bit overestimated by the reduced model.

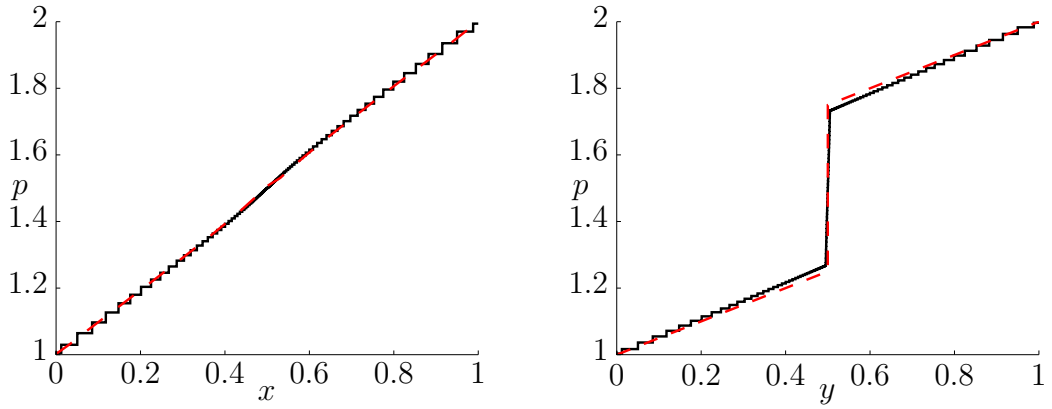

a horizontal fracture $y = 0.5$ **b** vertical fracture $x = 0.5$

Figure 5.6: Simple crossing: Pressure plots along fractures; black-solid line: Reference MPFA solution, red-dashed line: Reduced model solution

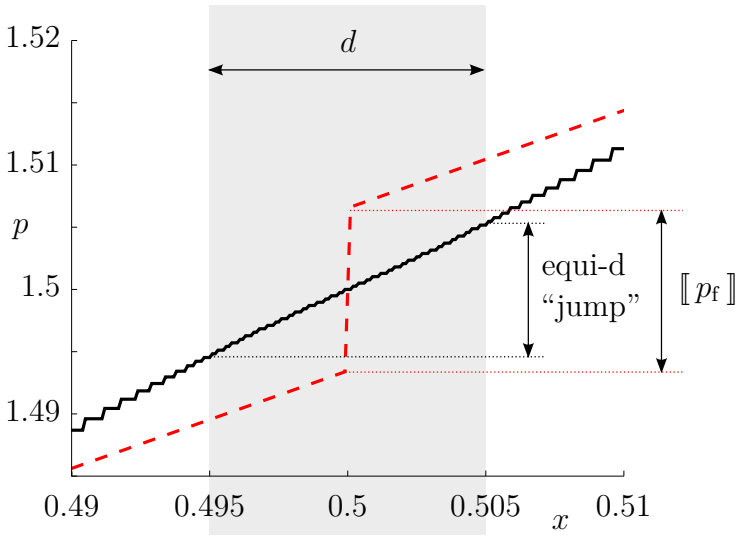

Figure 5.7: Simple crossing: Zoom on the crossing region of the pressure plot along the horizontal fracture; black-solid line: Reference MPFA solution, red-dashed line: Reduced model solution; grey background: Actual fracture domain in the equidimensional domain

5.3 Example 3: Different Crossing Area Permeabilities

This example shows a small fracture network consisting of three fractures as shown in figure 5.8a. It includes an X-crossingand a Y-crossing, highly conductive and almost impermeable fractures. The matrix permeability is the unit tensor $\boldsymbol{K}_{\mathrm{m}} = \mathbf{I}$. All fractures have the same aperture $d = 10^{-4}$. The horizontal fracture is highly conductive $k_{\mathrm{f,n}} = k_{\mathrm{f,t}} = 10^{4}$, whereas the vertical fractures are almost impermeable $k_{\mathrm{f,t}} = k_{\mathrm{f,n}} = 10^{-4}$. The permeabilities in the crossings are: $\boldsymbol{K}_{\Upsilon} = 10^{-4}\mathbf{I}$. All given values here are normalized.

The same type of boundary condition is applied on each side, i.e., for fracture and matrix. Dirichlet boundary conditions are set on the left and right boundary with a pressure gradient from left to right. The bottom boundary is closed (Neumann no flow) and an injection (Neumann inflow) is applied on the top boundary.

Grid convergence is shown by plotting the matrix pressure over a line. Figure 5.8b shows the pressure distribution in the domain for the coarse grid solution, the fractures and the location of the line plot (from [-0.2,-1.0] to [1.0,0.9]). The solution for three different refinement levels plotted over this line is shown in figure 5.9a and a zoom is shown in figure 5.9b. Convergence can easily be seen.

Furthermore the influence of different permeabilities in the crossing regions is considered. A second simulation is carried out with a different set of permeabilities in the two crossing regions. The X-crossing is highly permeable, $\boldsymbol{K}_{\Upsilon} = 1.0^{4}\mathbf{I}$, and the Y-crossinghas a mixed permeability, $\boldsymbol{K}_{\Upsilon} = \begin{pmatrix} 10^{-4} & 0 \\ 0 & 10^{4} \end{pmatrix}$.

The horizontal fractures, which are almost impermeable, lead to a pressure jump. In the crossing areas, this discontinuity depends on the corresponding permeabilities. In figure 5.10 the crossing area has almost the same permeability as the fractures itself, so that the discontinuity persists over the whole vertical fracture distance. The second case, figure 5.11, has two different permeabilities for the two crossing regions. The X-crossing is highly conductive in x- and y-direction and therefore

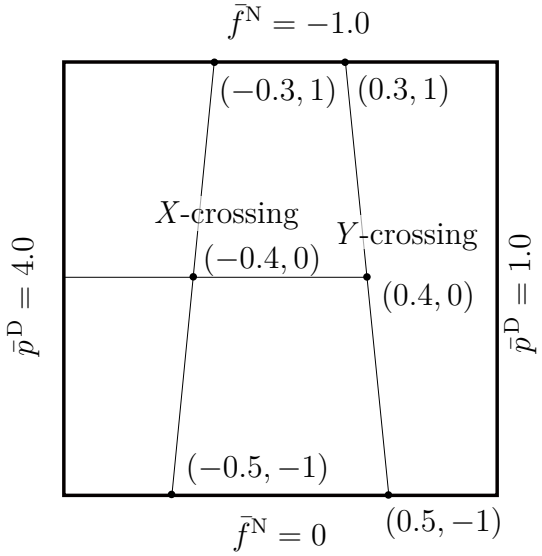

a simulation domain $(-1, 1) \times (-1, 1)$ with fractures and boundary conditions

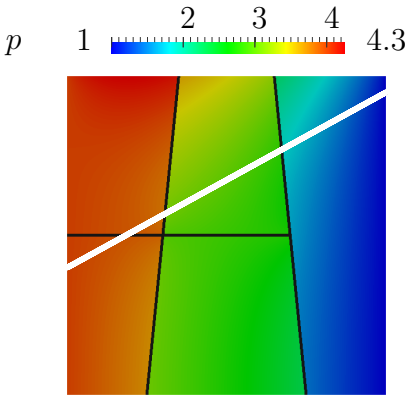

b coarse grid matrix pressure solution and location of the line plot.

Figure 5.8: Example 4: Simulation domain and pressure solution

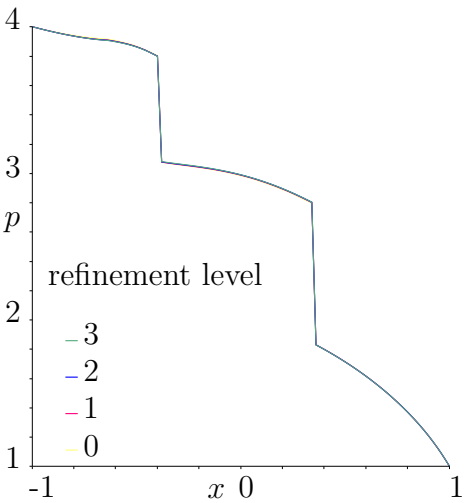

a Matrix pressures for coarse grid and three refinement levels along a line.

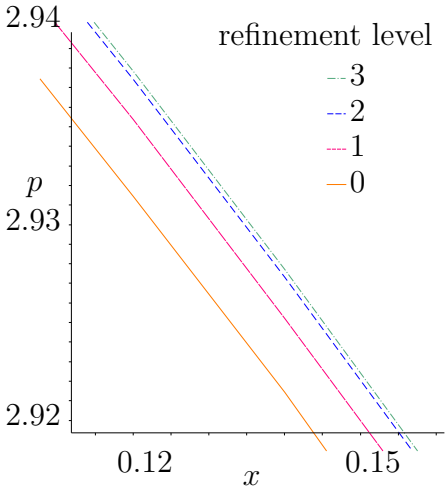

b Matrix pressures for coarse grid and three refinement levels along a part of the line show grid convergence.

forces also the matrix pressure to be almost continuous. The Y-crossing however, is highly conductive in y-direction and almost impermeable in x-direction. The discontinuity across the fracture is preserved and the permeability change along this fracture across the crossing region has almost no influence.

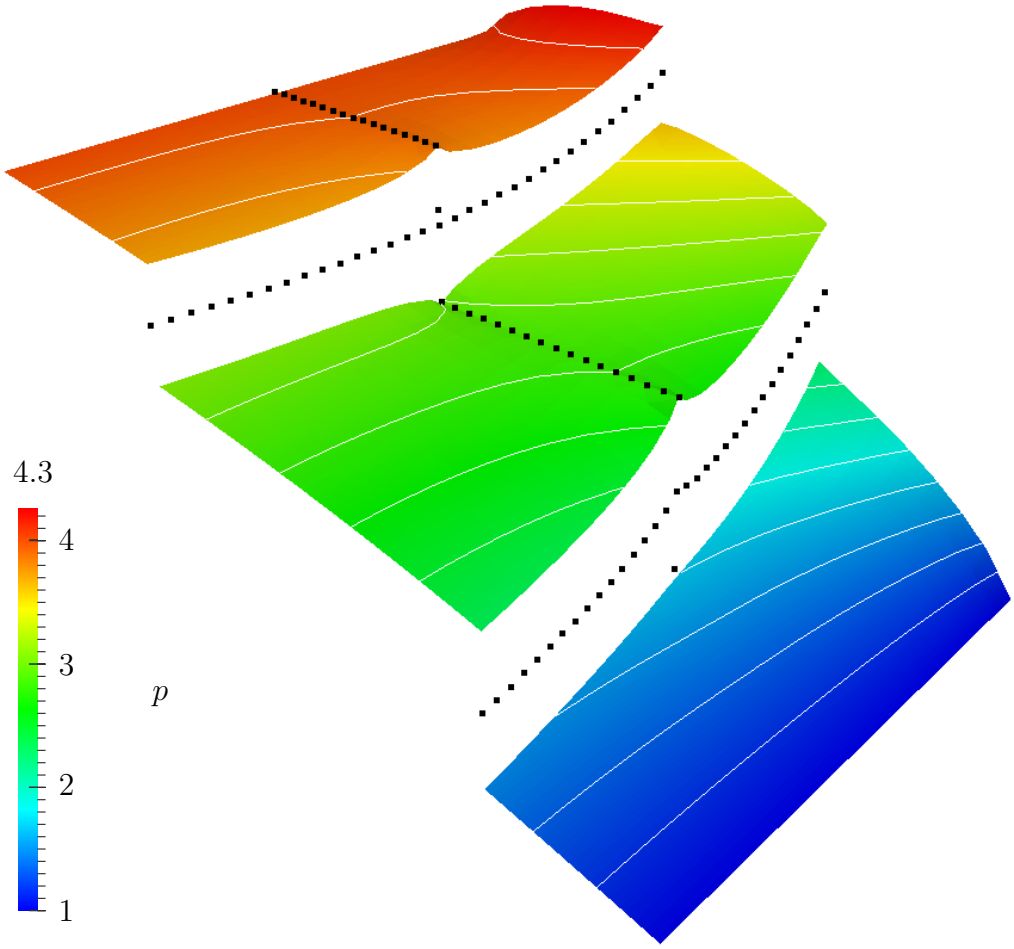

Figure 5.10: Pressure distribution in the matrix with the same permeability in both crossings: $\boldsymbol{K}_\Upsilon = 10^{-4}\mathbf{I}$.

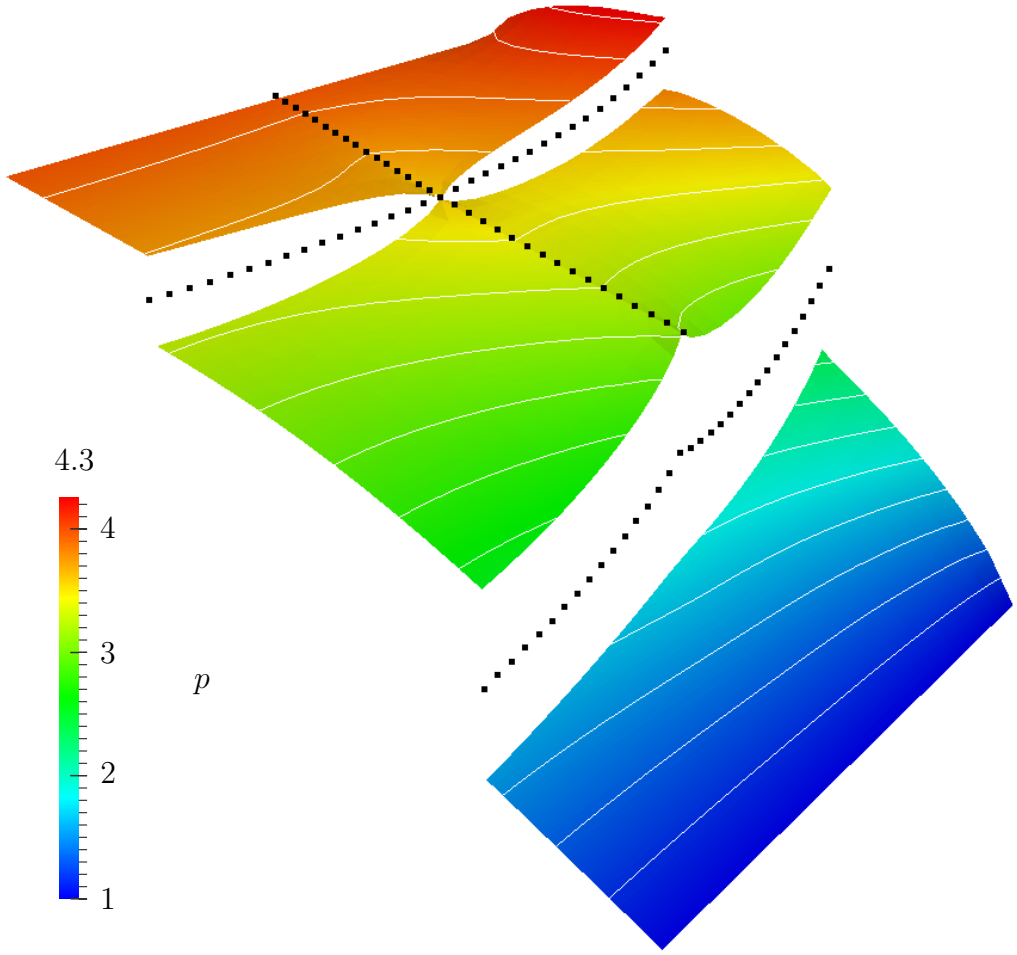

Figure 5.11: Pressure distribution in the matrix with a highly permeable crossing area in the X-crossing: $\boldsymbol{K}_{\Upsilon} = 1.0^4\mathbf{I}$, and a mixed permeability in the Y-crossing: $\boldsymbol{K}_{\Upsilon} = \begin{pmatrix} 10^{-4} & 0 \\ 0 & 10^4 \end{pmatrix}$.

5.4 Example 4: Hydrocoin Benchmark

Within the international Hydrocoin project, (Swedish Nuclear Power Inspectorate (SKI) 1987), a benchmark for heterogeneous groundwater flow problems was presented. The domain setup is shown in figure 5.12 with the exact coordinates given in table 5.1.

The boundary conditions are Dirichlet piezometric head on the top boundary and Neumann no flow on the other three boundaries. The hydraulic conductivity in the fracture zones is $10^{-6}\,\mathrm{m/s}$ and in the rock matrix $10^{-8}\,\mathrm{m/s}$, respectively. The inclination of the fracture zones has no influence on the permeability tensor and in lower dimensional models, the normal and tangential permeabilities are exactly the same scalars.

The original benchmark shows the piezometric head distribution along five horizontal lines through the modelled domain. Here only the plot at a depth of $-800\,\mathrm{m}$ is shown and compared to the range of results from the Hydrocoin summary report, (Swedish Nuclear Power Inspectorate (SKI) 1987), in figure 5.13. The dashed-dotted line shows the pressure head for a relatively coarse grid (303 unknowns, 17×13 standard and 82 enriched dofs) and the solid line for a uniformly refined grid (979 unknowns, 33×25 standard and 154 enriched dofs). The fracture element size is chosen in the same order of magnitude as the matrix element size and therefore also uniformly refined for the second case (38 and 70 dofs respectively). It is clearly visible that the solution is already very good close to the fractures (and the crossing) on the coarse grid and a significant error can only be seen in an area where no fractures are present, i.e., the fracture solution is very accurate and couples significantly back to the matrix. A finer grid is only necessary in areas where the (non-linear) solution is not captured well enough with the bi-linear standard finite elements.

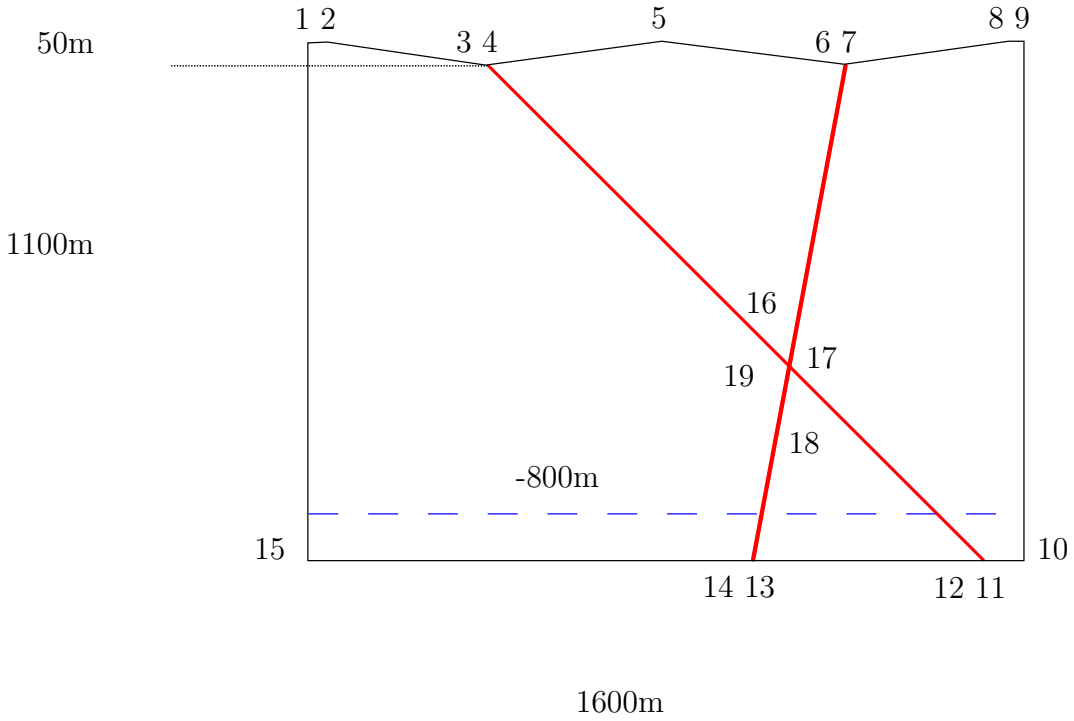

Figure 5.12: Geometry of the modelled domain of the Hydrocoin test case 2, (Swedish Nuclear Power Inspectorate (SKI) 1987). Boundary conditions are hydraulic head on top and Neumann no-flow on the other three sides of the domain.

Table 5.1: Coordinates of the numbered points in the modelled region of the problem depicted in figure 5.12,(Swedish Nuclear Power Inspectorate (SKI) 1987)

point	x (m)	z (m)	point	x (m)	z (m)
1	0	150	11	1505	-1000
2	10	150	12	1495	-1000
3	395	100	13	1007.5	-1000
4	405	100	14	992.5	-1000
5	800	150	15	0	-1000
6	1192.5	100	16	1071.35	-566.35
7	1207.5	100	17	1084.04	-579.04
8	1590	150	18	1082.5	-587.5
9	1600	150	19	1069.81	-574.81
10	1600	-1000			

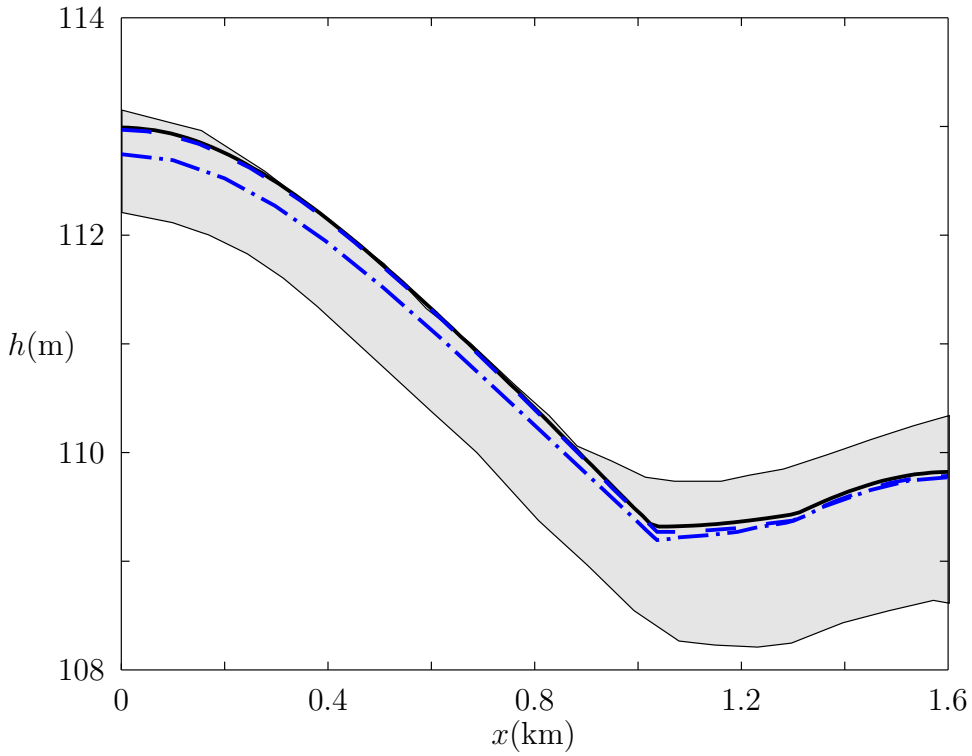

Figure 5.13: Hydraulic head for constant y=−800 m, the grey shaded area marks the range of different simulator results from the Hydrocoin summary report (Swedish Nuclear Power Inspectorate (SKI) 1987), the dashed-dotted line and the dashed line show the XFEM solution for a coarse (341 unknowns) and a refined grid (1049 unknowns), the solid line represents an equidimensional reference solution computed on a very fine grid with an MFD

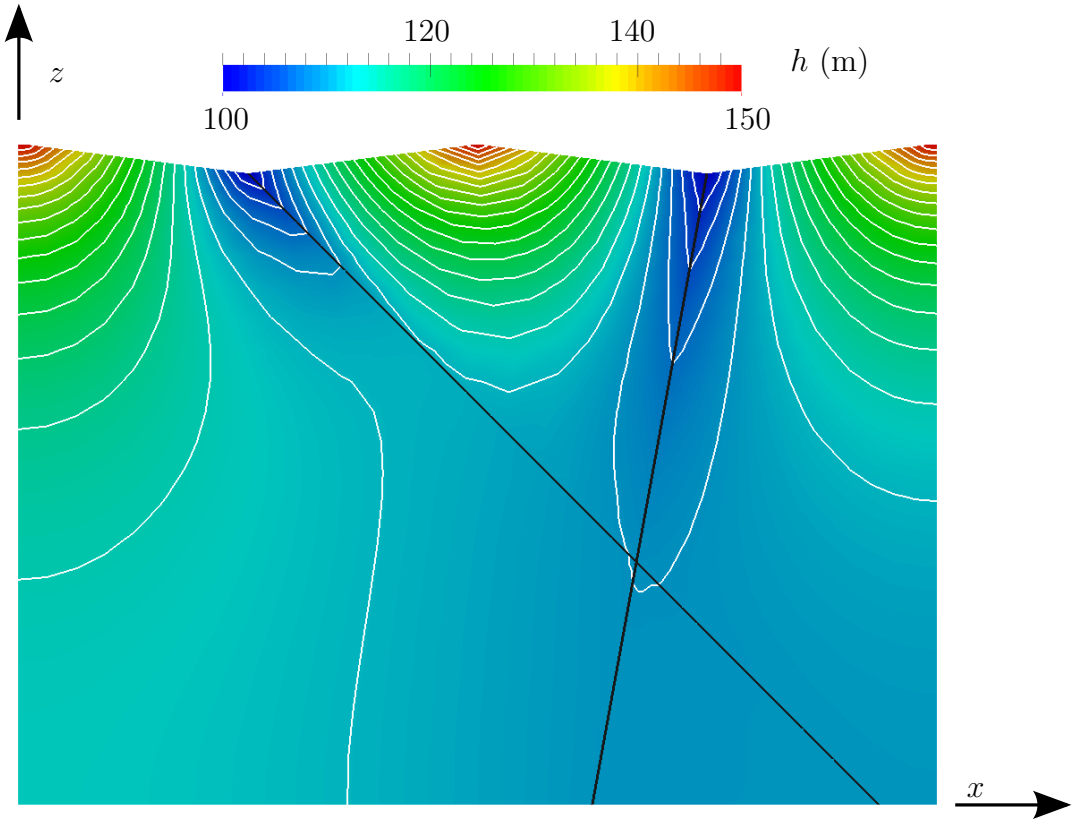

Figure 5.14: Hydraulic head contour plot for the XFEM solution on a fine grid (1049 unknowns)

5.5 Summary

In this chapter a novel approach to simulate co-dimension one fracture crossings of arbitrary number and intersection angles for arbitrary permeabilities is presented. It is easy to implement and integrate in existing (XFEM) codes and models and shows robust behavior for the presented implementation. A validation approach through comparison against an equidimensional model which is very finely resolved with a CCFV method with an MPFA-O method for the flux calculation, is conducted. Examples for highly conductive as well as almost impermeable fractures show numerical convergence and physical flow behavior. Moreover, the novel model is evaluated on a classical groundwater flow benchmark. This emphasizes the efficiency as well as accuracy of the presented model.

6 Boundary Conditions

Bibliographic Note: This chapter is based on: *Schwenck, N., Flemisch, B., Helmig, R., and Wohlmuth, B. I. (2014). Dimensionally reduced flow models in fractured porous media: Crossings and boundaries.* Submitted and NUPUS preprint 2014/5.

Classical boundary conditions are first (Dirichlet), second (Neumann) and third (Robin) kind. Other options are for example to eliminate parts of the boundary by demanding periodicity or symmetry or prescribing higher order derivatives, e.g., free outflow. In single phase subsurface systems very often Dirichlet and Neumann boundary conditions are used because they represent pressure and mass flux which also can be easily measured and directly links to physical concrete quantities. First type boundary conditions very often lead to a more stable numerical system.

This section deals with a way of prescribing Dirichlet boundary conditions to a fractured porous medium. Boundary conditions for fractured porous media systems with explicitly modelled fractures are not easy to define. The simplest choice is to prescribe a constant pressure along a domain boundary or a linear change for example for the case of a hydrostatic pressure distribution.

Applying constant or linear pressure over a larger part of a domain boundary often does not reflect the highly heterogeneous structure in the case of fractured porous media systems. That again leads to a strong influence of the boundary conditions on the solution if the domain is not chosen large enough. For field scale simulations, one usually obtains pointwise pressure information from which the best boundary conditions are to be picked. We present a possibility to interpolate pointwise pressure data along a given boundary including the information of the geometrical position

and geological parameters (aperture, permeability) of the fractures intersecting with this boundary.

In this section, we look only at the boundary of the problem domain, to be more precise a segment of arbitrary (non-zero) length of that boundary, figure 6.1. We define this segment as ω having local coordinates from zero to one $\chi \in [0, 1]$. There are n^{f} fractures intersecting with this boundary segment so that we get $n^{\mathrm{f}} + 1$ parts of the domain $\Omega_{\mathrm{m},i}$ adjacent to the boundary $\omega = \bigcup_i \omega_i$. The position of the fractures, χ_i, $i = 1, \ldots, n^{\mathrm{f}}$, intersecting with the boundary segment are given in boundary local coordinates. Additionally we define $\chi_0 = 0, \chi_{n^{\mathrm{f}}+1} = 1$ as the ends of the boundary segment we are looking at,

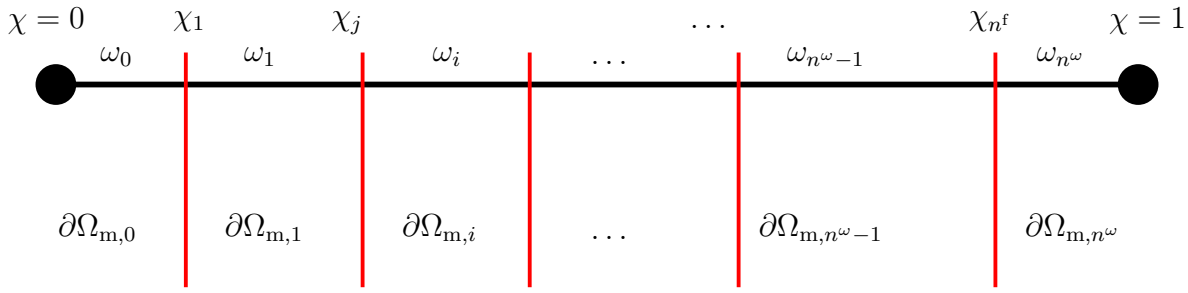

Figure 6.1: Partitioning of the boundary according to intersecting fractures.

$$\partial\Omega_{\mathrm{m},i} = [\chi_i, \chi_{i+1}] =: \omega_i, \qquad |\omega_i| = \chi_{i+1} - \chi_i.$$

We want to find an interpolation method to interpolate between χ_0 and $\chi_{\mathrm{n}+1}$, i.e., we set the pressure at $\chi = 0$ and $\chi = 1$. In our implementation for the complete 2d domain we use (bi-)linear finite elements, therefore we assume it to be sufficient if the interpolation on the boundary is piece-wise linear with respect to the intervals ω_i. The pressure can then be written for every boundary section as

$$p_{\mathrm{b}}(\chi) = m_i \chi + b_i \quad \text{so that } \nabla p_{\mathrm{b}} = m_i \quad \text{on } \omega_i, \tag{6.1}$$

with the two unknowns m_i, b_i. We admit a jump in the pressure across the fracture-boundary intersections. In particular, the jump at intersection j is given by the left

and right pressure limit, namely,

$$\begin{aligned}\llbracket p_{\mathrm{b}} \rrbracket_j &= \lim_{\chi \searrow \chi_j} p_{\mathrm{b}}(\chi_j) - \lim_{\chi \nearrow \chi_j} p_{\mathrm{b}}(\chi_j) \\ &= m_j \chi_j + b_j - m_{j-1}\chi_j - b_{j-1}, \end{aligned} \tag{6.2}$$

and it is positive in the normal direction from ω_{i-1} towards ω_i.

For the new problem we want to solve on ω, we introduce the test functions which are in $\mathcal{H}^1(\omega_i)$ and zero on the global boundary.

$$q_{\mathrm{b},i} = \begin{cases} n^{\omega}\chi - i & \text{on } \omega_i \\ 0 & \text{else} \end{cases} \tag{6.3}$$

This particular choice of testfunctions allows us to use

$$\begin{aligned} \nabla q_{\mathrm{b},i} &= n^{\omega} \quad \text{on } \omega_i, & i &= 0, \ldots, n^{\omega}, \\ \llbracket q_{\mathrm{b}} \rrbracket_j &= -1, & j &= 1, \ldots, n^{\mathrm{f}}, \\ \llbracket q_{\mathrm{b},i} \rrbracket_j &= n^{\omega}\chi_j - i, & & \\ \llbracket q_{\mathrm{b},i} \rrbracket_{j+1} &= -n^{\omega}\chi_{j+1} + i. & & \end{aligned}$$

To close the system there are two obvious choices. First the pressure in the fracture can be set equal to the average of the adjacent matrix pressures. This has the advantage that the modeler does not need any extra information, i.e., does not have to know the pressure in the fractures at the boundary. However, this is a strong assumption which is not necessarily physically correct within the domain. The other possible choice, which can be required by the application setup, is to set the pressure in the fractures additionally to the two matrix pressures at $\chi = 0$ and $\chi = 1$.

6.1 Fracture Pressure as Output

Assuming the average of the pressure left and right of the fracture to be equal to the pressure in the fracture leads to the following boundary functions for single and multiple fractures. We use the weak formulation for the matrix (2.6a), but now only on the boundary with zero dimensional fractures and the assumption $p_{\mathrm{f}} = \{\!\{ p_{\mathrm{m}} \}\!\}$, i.e., we do not need (2.6b), and obtain

$$\sum_{i=1}^{2} \left((\boldsymbol{K}_i \boldsymbol{s} \cdot \boldsymbol{s}) \nabla p_{\mathrm{b}},\ \nabla q_{\mathrm{b}} \right)_{\omega_i} + \frac{k_{\mathrm{f,n}}}{d} [\![p_{\mathrm{b}}]\!] [\![q_{\mathrm{b}}]\!] \Big|_{\omega_1 \cap \omega_2} = 0. \tag{6.4}$$

Here, $\boldsymbol{s}$ is a vector which is oriented along the boundary of $\partial\Omega_{\mathrm{m},i}$, so that we can define the effective permeability of the boundary section ω_i to be $\mathbf{K}_i \boldsymbol{s} \cdot \boldsymbol{s} =: k_{\mathrm{b},i}$. Extending (6.4) to multiple fractures gives

$$\begin{aligned} \sum_{i=j-1}^{j} \int_{\omega_i} k_{\mathrm{b},i}\ \nabla p_{\mathrm{b}} \cdot\ \nabla q_{\mathrm{b}}\ \mathrm{d}\boldsymbol{s} \\ = -\left. \frac{k_{\mathrm{f,n}}}{d} \right|_j [\![p_{\mathrm{b}}]\!]_j [\![q_{\mathrm{b}}]\!]_j \quad \text{for } j = 1, \ldots, n^{\mathrm{f}} \end{aligned} \tag{6.5}$$

With the given boundary conditions that we want to interpolate, namely, $p_{\mathrm{b}}(0) = \mathrm{p_{left}}$ and $p_{\mathrm{b}}(1) = \mathrm{p_{right}}$, and the additional constraint assumption, $p_{\mathrm{f},i} = \{\!\{ p_{\mathrm{b}} \}\!\}_i$, we get a general solution for the linear pressure parts on the boundary,

$$m_i = \frac{\mathrm{p_{right}} - \mathrm{p_{left}}}{\tilde{k}_i}, \tag{6.6}$$

with

$$\begin{aligned}\tilde{k}_i =& k_{\mathrm{b},i}\omega_i \frac{q_{0\,0}}{q_{-1\,0}} \prod_{\ell=0}^{i} \frac{q_{(\ell-1)\ell}}{q_{\ell\ell}} \\ & \cdot \left\{ \sum_{j=1}^{n^{\mathrm{f}}} q_{(j-1)j} \prod_{k=1}^{j} \frac{q_{kk}}{q_{(k-1)k}} \left[\left. \frac{d}{k_{\mathrm{f,n}}} \right|_j \left(\frac{1}{q_{(j-1)j}} + \frac{1}{q_{jj}} \right) \right.\right. \\ & \left.\left. + \chi_j \left(\frac{1}{k_{\mathrm{b},j}\omega_j} \frac{1}{q_{(j-1)j}} - \frac{1}{k_{\mathrm{b},j-1}\omega_{j-1}} \frac{1}{q_{jj}} \right) \right] \right. \\ & \left. + \frac{1}{k_{\mathrm{b},n^\omega}\omega_{n^\omega}} \prod_{\ell=1}^{n^{\mathrm{f}}} \frac{q_{\ell\ell}}{q_{(\ell-1)\ell}} \right\} \qquad \text{for } i = 0, \ldots, n^\omega, \end{aligned} \tag{6.7}$$

where $q_{ij} \coloneqq [\![q_{\mathrm{b},i}]\!]_j$, $q_{0\,0}$ and $q_{-1\,0}$ are only introduced for ease of notation, are not assigned any value and always cancel out. Moreover, the coefficients b_i are given as

$$\begin{aligned} b_i = \sum_{\ell=1}^{i} \Bigg(& \chi_\ell \left(m_{\ell-1} - m_\ell \right) \\ & + \left. \frac{d}{k_{\mathrm{f,n}}} \right|_\ell \left(\sum_{k=\ell-1}^{\ell} k_{\mathrm{b},k} m_k \omega_k \right) \Bigg) + b_0 \end{aligned} \tag{6.8}$$

For the reformulations above, we require the fracture positions to be different than the roots of the jump terms of the test functions to avoid division by zero.

For one single fracture, $n^{\mathrm{f}} = 1$, this yields

$$m_0 = \frac{\mathrm{p}_{\mathrm{right}} - \mathrm{p}_{\mathrm{left}}}{\frac{k_{\mathrm{b},0}}{k_{\mathrm{f,n}}} d + \omega_1 + \omega_0 \frac{k_{\mathrm{b},0}}{k_{\mathrm{b},1}} + (\frac{k_{\mathrm{b},0}}{k_{\mathrm{b},1}} - 1)}, \tag{6.9}$$

$$m_1 = \frac{\mathrm{p}_{\mathrm{right}} - \mathrm{p}_{\mathrm{left}}}{\frac{k_{\mathrm{b},1}}{k_{\mathrm{f,n}}} d + \omega_0 + \omega_1 \frac{k_{\mathrm{b},1}}{k_{\mathrm{b},0}} + (1 - \frac{k_{\mathrm{b},1}}{k_{\mathrm{b},0}})}. \tag{6.10}$$

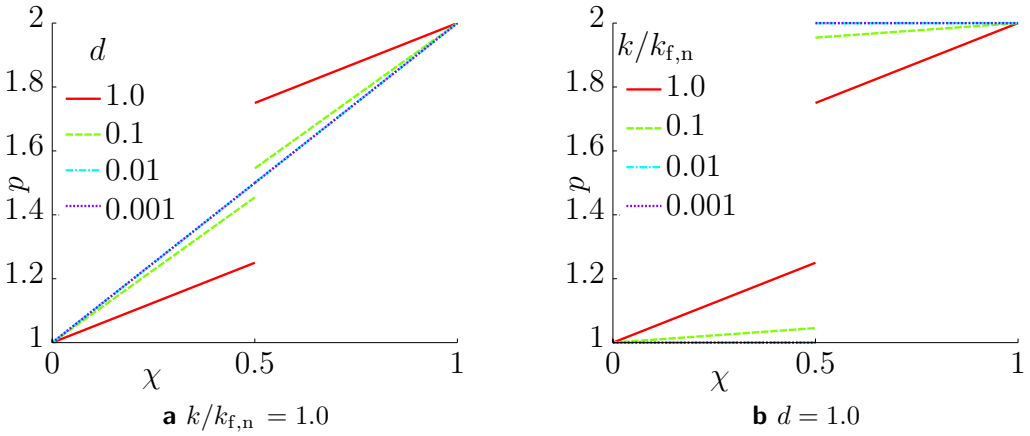

Figure 6.2: Boundary interpolation for variations of aperture and matrix-fracture permeability ratio. $p_{\text{left}} = 1.0$, $p_{\text{right}} = 2.0$

As an example, we look at the symmetric case of one fracture intersecting a homogeneous rock matrix boundary, $k = k_{\text{b},0} = k_{\text{b},1}$, $\omega_0 = \omega_1 = \chi_1 = 0.5$. Then

$$m_0 = m_1 = \frac{\mathrm{p}_{\text{right}} - \mathrm{p}_{\text{left}}}{1 + \frac{k}{k_{\text{f,n}}} d}, \tag{6.11}$$

$$[\![p]\!] = \frac{\mathrm{p}_{\text{right}} - \mathrm{p}_{\text{left}}}{1 + \frac{k_{\text{f,n}}}{k} \frac{1}{d}}. \tag{6.12}$$

From (6.11) and (6.12), we can see, cf. figure 6.2, for the different limit cases that

- for a really small fracture width, $\lim_{d \to 0}$, the pressure gradient is the same as without a fracture and the pressure jump is zero,
- for a highly conductive fracture, $\lim_{k/k_{\text{f,n}} \to 0}$, there is almost no effect on the pressure gradient and the jump is zero,
- and for a totally impermeable fracture, $\lim_{k_{\text{f,n}}/k \to 0}$, the pressure gradient is zero and therefore $[\![p]\!] = \mathrm{p}_{\text{right}} - \mathrm{p}_{\text{left}}$.

A detailed derivation of the general solution for multiple fractures and the fracture pressure as output: Keep in mind that the test function q_b is actually not zero in one of the adjacent areas, $[\![\, q_{\mathrm{b},i} \,]\!]_i \neq [\![\, q_\mathrm{b} \,]\!]_i$. In (6.5) already the sum over the two equations in the two sub-domains was evaluated, so that always both volume parts are non-zero and the jump is actually dependent on both sides. If only the test function for one area is used, (6.3), for example $q_{\mathrm{b}i}$, (6.5) can be rewritten into

$$\int_{\omega_i} k_{\mathrm{b},i} \nabla p_\mathrm{b} \nabla q_{\mathrm{b},i} + \left. \frac{k_{\mathrm{f,n}}}{d} \right|_i [\![\, p_\mathrm{b} \,]\!]_i [\![\, q_{\mathrm{b},i} \,]\!]_i = 0 \quad \text{for } i = 1, \ldots, n^\mathrm{f}$$

so that

$$\frac{k_{\mathrm{b},i}\omega_i m_i}{q_{ii}} = \frac{k_{\mathrm{b},i-1}\omega_{i-1} m_{i-1}}{q_{(i-1)i}} \quad \text{for } i = 1, \ldots, n^\mathrm{f}. \tag{6.13}$$

Combining (6.13) for all i and reformulating it for every m_i gives (6.14).

$$m_i = \frac{k_{\mathrm{b},0}\omega_0}{k_{\mathrm{b},i}\omega_i} \prod_{k=1}^{i} \frac{q_{kk}}{q_{(k-1)k}} m_0 \quad \text{for } i = 1, \ldots, n^\mathrm{f}. \tag{6.14}$$

With the original (6.5) and thus $[\![\, q_\mathrm{b} \,]\!]_i = -1$ for all i, we obtain

$$\begin{aligned} &k_{\mathrm{b},i}\omega_i m_i + k_{\mathrm{b},i-1}\omega_{i-1} m_{i-1} \\ &\qquad - \left. \frac{k_{\mathrm{f,n}}}{d} \right|_i \Big(m_i \chi_i + b_i - m_{(i-1)} \chi_i - b_{(i-1)} \Big) = 0 \quad \text{for } i = 1, \ldots, n^\mathrm{f}, \end{aligned}$$

which can be used together with (6.14) to derive (6.7).

The boundary conditions

$$b_0 = \mathrm{p_l}, \quad m_n + b_n = \mathrm{p_r}$$

close the system.

6.2 Fracture Pressure as Input

Following the same steps as in section 6.1, but allowing $p_{\mathrm{f}} \neq \{\!\{ p_{\mathrm{m}} \}\!\}$, the full equation on the boundary becomes

$$\begin{aligned}\sum_{i=j-1}^{j} & \int_{\omega_i} k_{\mathrm{b},i} \, \nabla p_{\mathrm{b}} \cdot \, \nabla q_{\mathrm{b}} \, \mathrm{d}\boldsymbol{s} \\ & + \frac{k_{\mathrm{f,n}}}{d}\bigg|_j [\![p_{\mathrm{b}}]\!]_j [\![q_{\mathrm{b}}]\!]_j \\ & + \frac{4k_{\mathrm{f,n}}}{d}\bigg|_j \left(\{\!\{ p_{\mathrm{b}} \}\!\}_j - p_{\mathrm{f}\,j} \right) \{\!\{ q_{\mathrm{b}} \}\!\}_j \\ & = 0 \quad \text{for } j = 1, \ldots, n^{\mathrm{f}}. \end{aligned} \tag{6.15}$$

This equation includes the fracture pressure at every fracture intersecting the boundary and therefore needs this as input information, i.e., as a first step the PDE (6.15) is solved and used to define the boundary conditions for (2.6a).

6.3 Example 5: Solving the Complete System on the Boundary

In this example, the assumption that the average matrix pressure equals the fracture pressure is not made but instead the fracture pressure is an additional parameter which has to be set by the modeler. This example shows a single fracture system with different boundary values on the top and on the bottom of the domain. The left and right hand side of the domain get homogeneous Neumann boundary conditions. The left pressure is set to $p_{\mathrm{b,left}} = 1.0$, the right pressure to $p_{\mathrm{b,right}} = 2.0$ and the pressure in the fracture to $p_{\mathrm{f}} = 0.5$ at the bottom and to $p_{\mathrm{f}} = 1.8$ at the top.

The values for the Dirichlet boundaries are plotted in figure 6.3. There are three different cases, a constant value left and right of the fracture respectively, a linear interpolation from the left and right matrix pressure value to the fracture pressure

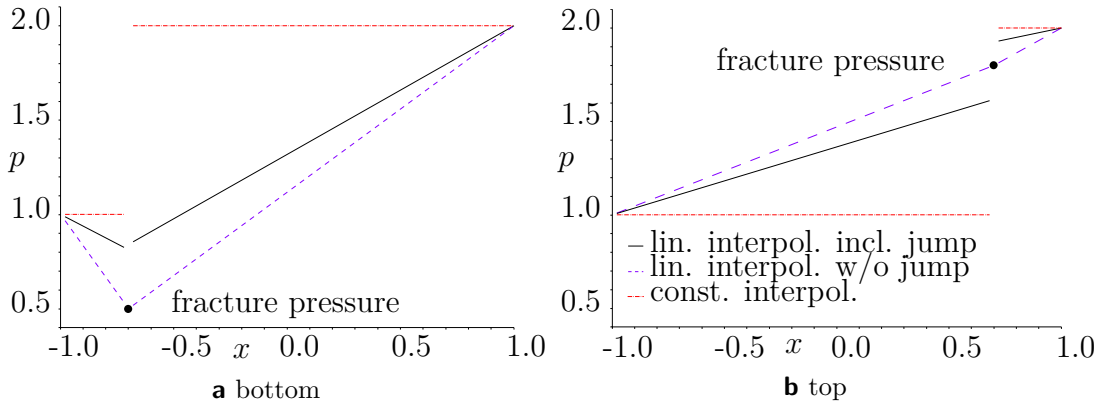

Figure 6.3: Pressure boundary condition on the bottom and on the top of the domain for three interpolation methods.

value without a jump and the linear interpolation which includes a pressure jump across the fracture as a solution of (6.15) on the boundary. Keep in mind that for that case the pressure in the fracture not necessarily is equal to the average pressure, this can clearly be seen at the bottom boundary.

The choice of the boundary values affects the solution in the matrix as well as in the fracture significantly. The pressure in the fracture for all three cases is plotted in figure 6.4. The piecewise constant pressure leads to a significantly different flow behavior in the fracture, very steep gradients close to the boundary and a pressure gradient in the domain which has the opposite direction than for the other cases. The linear interpolated pressure with and without a jump across the fracture show a similar behavior. The constant pressure on the boundary which does not account for the fracture pressure influence on the matrix, represents a physically totally different setup and is therefore neglected in the following discussion.

The pressure contour in the matrix for the linear interpolation without a jump and allowing a jump are shown in figure 6.5. The matrix pressure inside the domain looks similar, i.e., if the domain is large enough the influence of the different interpolation methods is negligible. However, there is a clearly visible jump across the fracture within the domain. The jump inside the domain can easily be seen in figure 6.6, where the jump is plotted along the fracture and in figure 6.7 where the matrix pressure is plotted for constant $y = 0.9$ (close to the boundary). The pressure

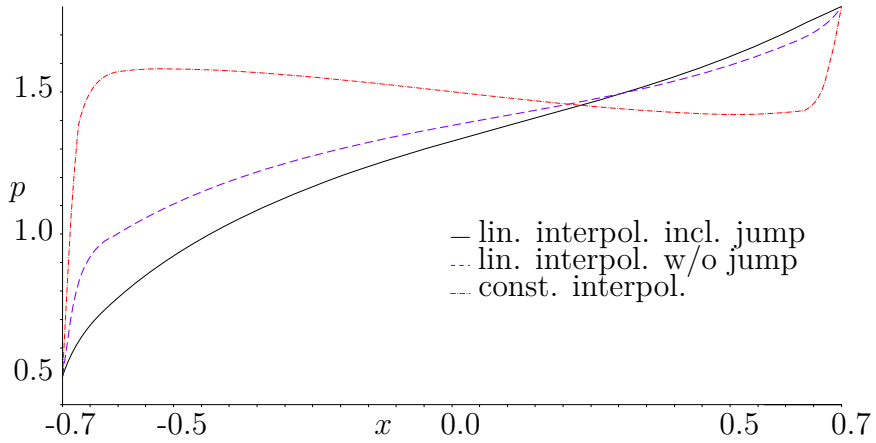

Figure 6.4: Pressure in the fracture for three different boundary conditions on the rock matrix boundaries

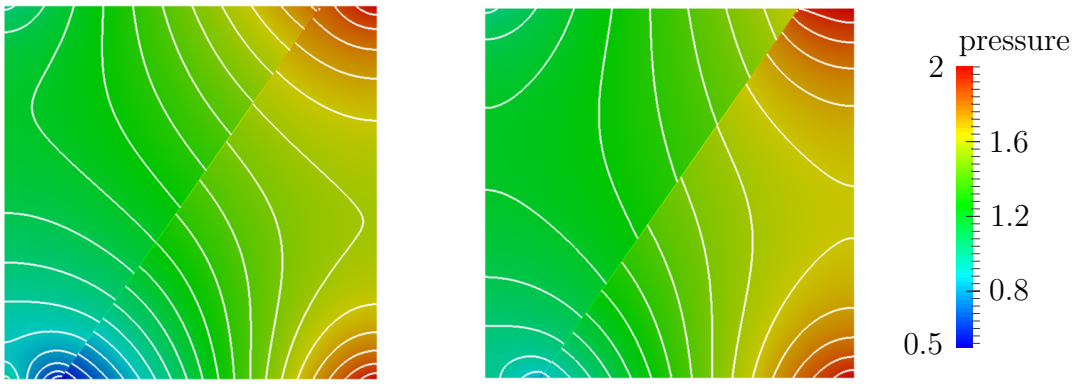

Figure 6.5: Contour plot: Linear interpolation on the boundary without a jump (left) and allowing a jump (right)

continuity at the boundary forces the pressure jump inside the domain to be smaller. Unless there is a physical reason to prohibit this jump at the boundary, allowing it certainly appears to be more justified.

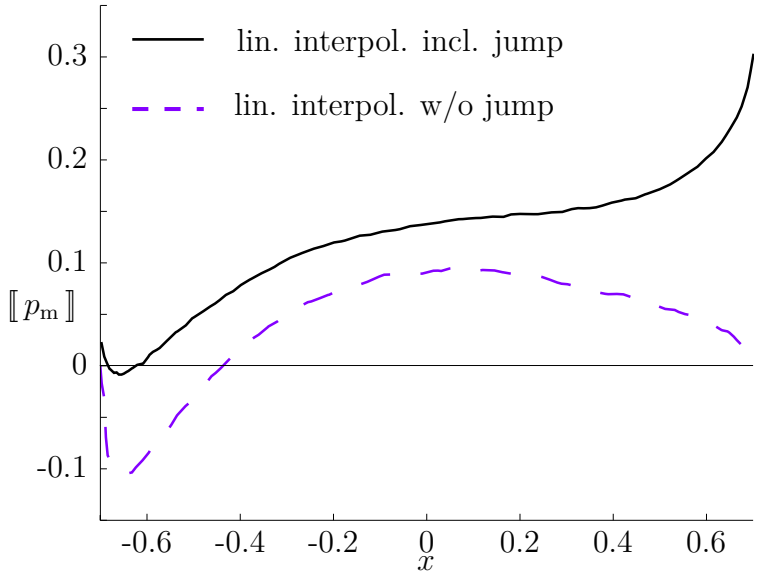

Figure 6.6: Matrix pressure jump plotted along the fracture for the boundary conditions allowing a jump and linear interpolation without a jump

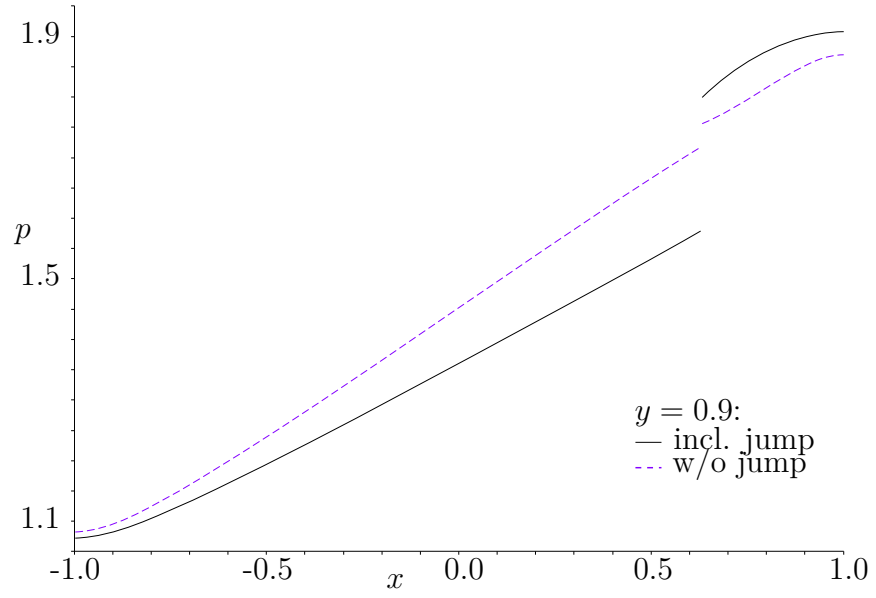

Figure 6.7: Matrix pressure vs. x-distance at constant y=0.9 for the boundary with and without a jump

6.4 Summary and Outlook

This chapter presents a novel method to interpolate pressure distributions on boundaries with fractures which then can be used as Dirichlet boundary condition values. Depending on the problem to simulate and the given data the interpolation can calculate the fracture pressures or take them as additional input to give an even better approximation of the pressure distribution on the boundaries. The presented example shows the influence of the boundary conditions and the advantage of the novel approach.

A validation against experimental data still has to show how much better the newly presented approach is and in which situations or problem setups the fracture pressure should better be chosen as input and in which as output.

7 Comparison of Lower- and Equidimensional, Discrete and Embedded Models

This section shows advantages and disadvantages of the model and implementation presented in this thesis and compares it against other model concepts including model specific implementations by means of different examples.

The reference solutions are computed on very fine grids with equidimensional models which use either a cell-centered finite volume method with a multipoint flux approximation (O-method) or a mimetic finite difference method. Both models are used as they are implemented in DuMu^{x} 2.6.

The lower-dimensional XFEM model competes against a classical, lower-dimensional (mixed-dimensional) discrete fracture-matrix model (DFM), which assumes that the flow occurs both in the fracture network and the surrounding rock matrix, e.g., (Helmig 1997, Monteagudo and Firoozabadi 2004, Reichenberger et al. 2006). The spatial discretization is performed with the box method (Helmig 1997) which combines the advantages of finite element and finite volume grids, allowing unstructured gridding and being locally conservative.

In the Master's thesis Köppel (2013), a novel co-dimension one approach was developed. It can handle non-conforming fracture and matrix grids. The coupling between fracture and matrix grids is carried out with a Lagrangian multiplier technique, similar to Mortar techniques. This approach (henceforth, LM) is used in addition to the aforementioned models for comparisons.

The first example shows a highly conductive regular fracture network. It is followed by an example which uses the same domain and boundary conditions, but the fractures are now less conductive than the matrix. As a third example a literature benchmark setup is used. The last example is a small, but complex fracture network with highly conductive and lower permeable fractures.

7.1 Example 6: Highly Conductive Regular Fracture Network

This test case is based on an article presenting a new dual continuum model, (Geiger et al. 2011), with slightly modified boundary conditions and soil properties. The results of the three different discrete models can be used as reference for future evaluation of multi continuum models. The domain of simulation is shown in figure 7.1a.

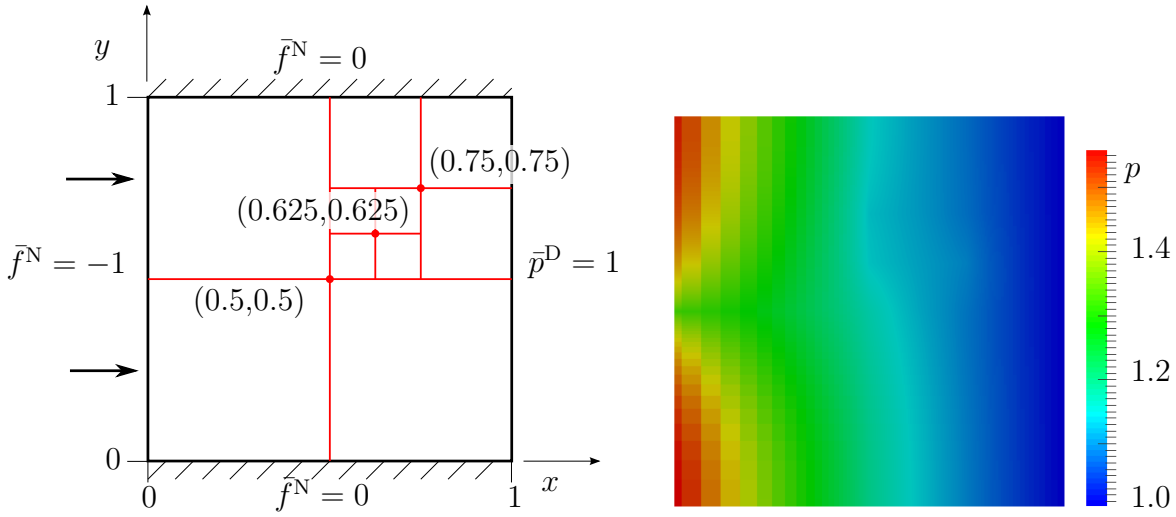

a $\boldsymbol{K}_{\mathrm{m}} = \mathbf{I}$, $k_{\mathrm{f,n}} = k_{\mathrm{f,t}} = 10^4$, $d = 10^{-4}$ **b** pressure reference solution

Figure 7.1: Example 6: Domain and boundary conditions and pressure reference solution

The reference solution is computed on a grid which resolves every fracture with 19 elements in normal direction and becomes coarser away from the fractures. It has a total of 1,354,896 control volumes.

The pressure distribution of the reference solution is shown in figure 7.1b. For comparison of the different models, figures 7.2a and 7.2b show the pressure in the matrix along a horizontal line at constant $y = 0.7$ and in a vertical fracture along a line at constant $x = 0.5$, respectively. The DFM model matches the reference solution best. The LM model seems to be incapable to capture the pressure accurately. The conform case performs a little better than the non-conform situation. The XFEM

Table 7.1: Example 6: Global and fracture error

	# DOFs	e $\cdot 10^{-3}$	e_f $\cdot 10^{-3}$
DFM	524	1.41	0.26
XFEM	536	8.11	6.09
	5072	1.75	1.02
LM conform	413	70.54	69.58
LM non-conform	484	935.24	122.57

model matches the matrix pressure quite well. The fracture pressure representation, however, is not accurate enough.

The advantage of independent grids and thus, independent refinement, is shown by means of an example in figure 7.3. The pressure of the vertical fracture at $x = 0.5$ is plotted for the reference solution and various refinement levels of the fracture grid in the XFEM reduced model. Convergence can easily be observed.

The pressure solution along a vertical line at constant $x = 0.7$ shows non-monotone behavior. A zoom is shown in figure 7.4. The LM model overestimates the pressure significantly. The lower-dimensional DFM model which resolves the fractures through the grid captures the non-monotone behavior more efficiently than the XFEM model. The XFEM model can capture the non-linear, non-monotone pressure solution only with a finer matrix grid (away from the fracture). A refinement of only the fracture grid leads to a significantly better approximation but the accuracy of the DFM model can only be reached if the matrix grid is also refined.

The global and the fracture error, in this case the difference between the reduced model and the reference solution in the $\mathcal{L}^2$ norm, for the different models is shown in table 7.1.

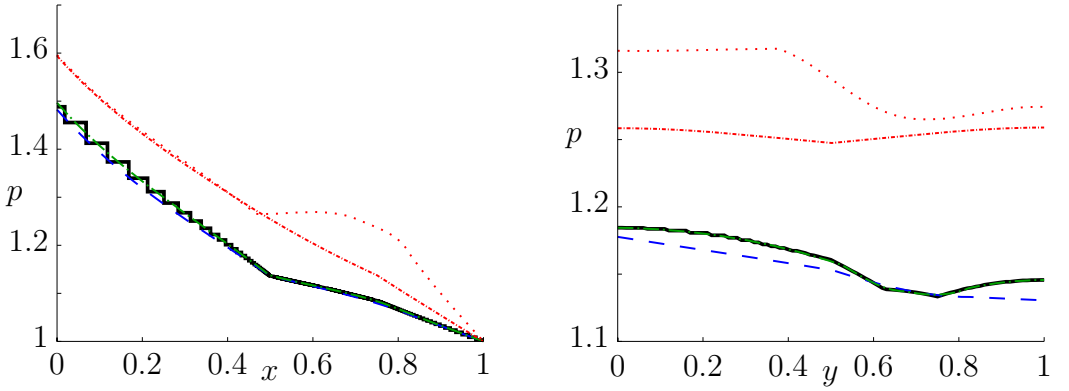

a matrix pressure along constant $y = 0.7$ **b** fracture pressure along constant $x = 0.5$

Figure 7.2: Example 6: Pressure in the matrix along a horizontal line at a constant $y = 0.7$ and in a vertical fracture along a line at a constant $x = 0.5$; black solid: Reference MPFA CCVF, dashed blue: XFEM, dash-dotted green: DFM, red dotted: Non-conform LM, dash-dotted red: Conform LM

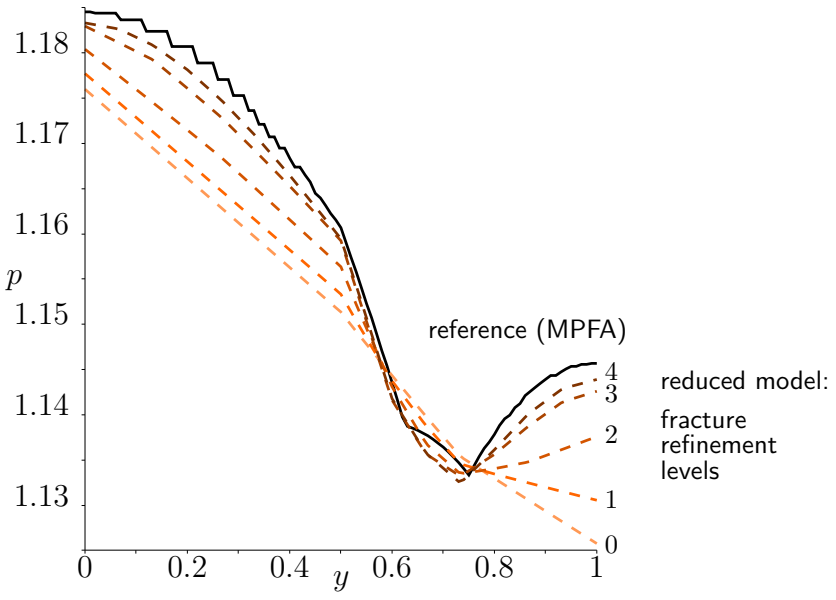

Figure 7.3: Pressure along vertical fracture $x = 0.5$; black solid: Reference MPFA CCVF, dashed yellow to brown: Reduced model fracture pressure for various refinement levels of only the fracture grid

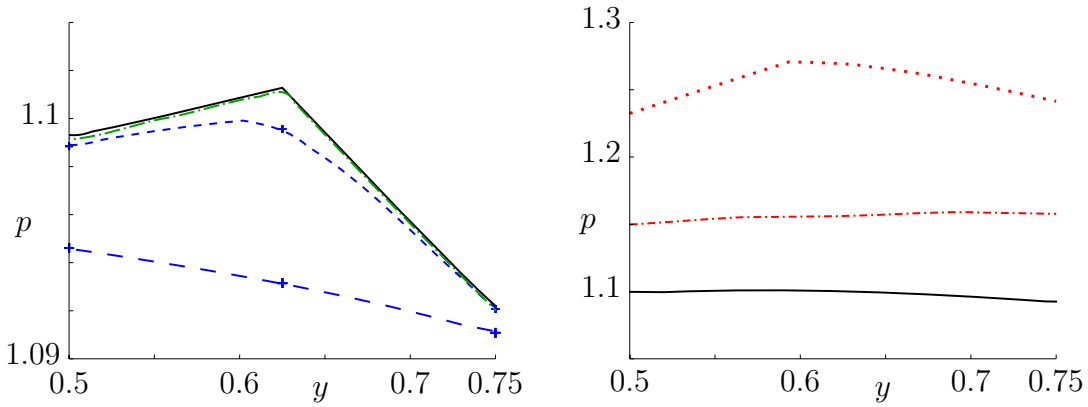

a DFM, XFEM and reference

b LM and reference

Figure 7.4: Example 6: Pressure in the matrix along a vertical line at a constant $x = 0.7$; black solid: Reference MPFA CCVF, dashed blue: XFEM with coarse and fine fracture grid, dash-dotted green: DFM, red dotted: Non-conform LM, dash-dotted red: Conform LM

7.2 Example 7: Impermeable Regular Fracture Network

The domain and the boundary conditions of this example are identical to the previous example, 7.1a, with only the fracture permeability changed to $k_{\mathrm{f,n}} = k_{\mathrm{f,t}} = 10^{-4}$, so that the fractures now act as barriers for the flow.

The XFEM pressure field on the matrix grid is shown in figure 7.5a. The DFM model is theoretically not able to represent this flow field correctly because the model averages the pressures at the heterogeneity interfaces and does not allow discontinuities. A plot along a diagonal line throughout the whole domain from $(0.0, 0.1) - (0.9, 1.0)$ shows the almost exact fit of the XFEM model and the reference solution and the inability of the DFM model to match the reference solution.

The performance of the LM is not shown in this example because it is in theory not able to handle almost impermeable fractures.

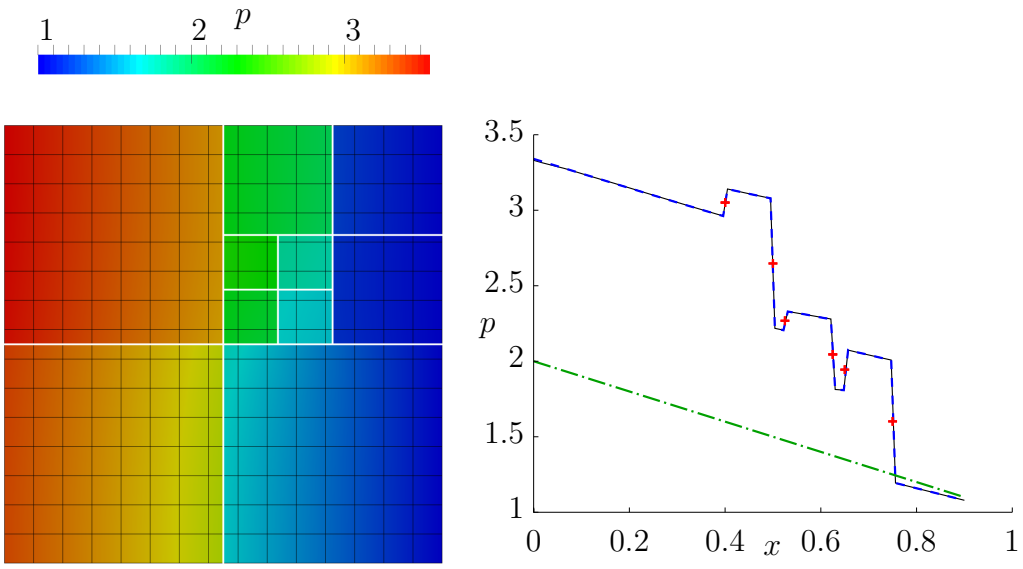

a XFEM contour plot with matrix grid and fractures

b plot along segment (0.0,0.1)–(0.9,1.0); black-solid: reference solution, blue-dashed and red-crossed: XFEM matrix and fracture pressures, green dash-dotted: DFM

Figure 7.5: Example 7: Pressure solution

7.3 Example 8: Hydrocoin Benchmark

This example is based on the international Hydrocoin project, (Swedish Nuclear Power Inspectorate (SKI) 1987), a benchmark for heterogeneous groundwater flow problems. The benchmark with domain, boundary conditions and soil properties is presented in section 5.4, figure 5.12. In this section the XFEM model is compared against two equidimensional models, one is calculated with a cell centered finite volume method with two-point flux approximation, the other with a mimetic finite difference approach. Also a co-dimension one solution of a DFM model based on a Box discretization is shown.

The two-point flux model, although equidimensional and on a very fine grid, is not able to capture the datum correctly but overestimates the pressure, figure 7.6. The DFM model and the XFEM model with roughly the same number of degrees of freedom match the reference solution quite well. The XFEM model underestimates the pressure in the right half slightly more than the DFM.

The advantage of two independent grids of the XFEM for this example is shown in figure 7.7, where the XFEM solution on a coarse grid, a fine grid and a coarse matrix grid with a fine fracture grid is plotted. By only refining the fracture grid, the increase in the total number of degrees of freedom is minimal but the solution improves significantly and almost matches the fine grid solution.

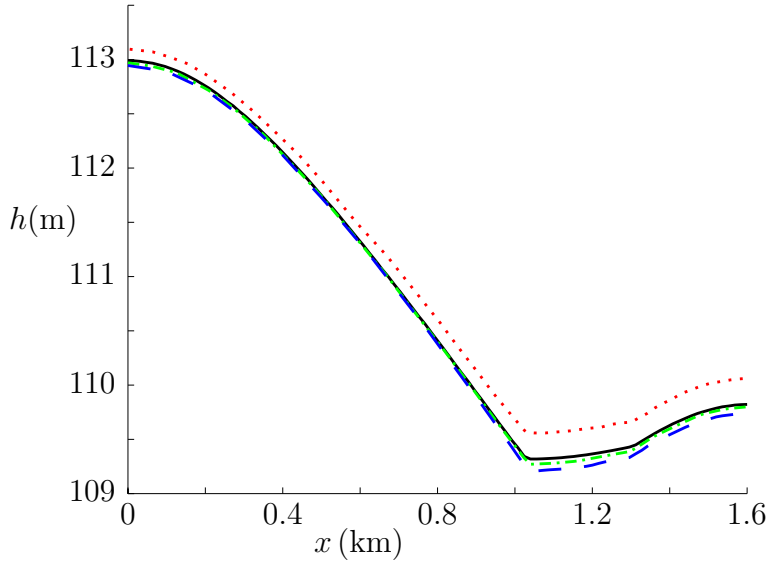

Figure 7.6: Pressure at constant depth −800 m; black solid: Reference MFD, dashed blue: XFEM with 373 degrees of freedom, green dash-dotted: DFM with 441 degrees of freedom, dotted red: Equidimensional Box model with TPFA on the same grid as reference solution ($\approx 1.5 \cdot 10^6$ dofs)

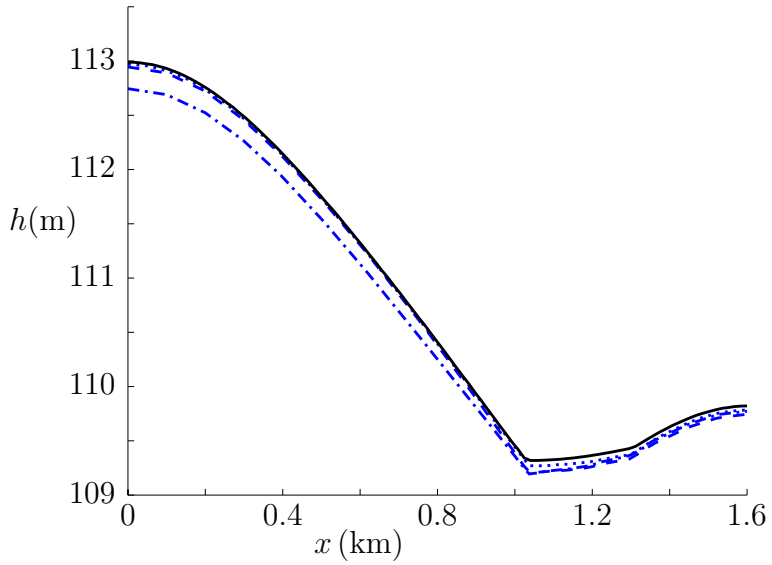

Figure 7.7: Pressure at constant depth −800 m; black solid: Reference MFD, blue dash-dotted: Coarse grid XFEM solution with 341 dofs, blue dotted, refined grid XFEM solution with 1049 dofs, blue dashed: Coarse matrix grid and refined fracture grid XFEM solution with 373 dofs

7.4 Example 9: Complex Fracture Network

This section concludes with a small, but complex fracture network example. The fracture network is chosen such that it includes all the important aspects for which conceptual models and implementations were developed in this thesis. The domain and boundary conditions are shown in figure 7.8. The exact coordinates for the fracture positions are listed in table 7.3. The fracture network contains a single, straight fracture ending inside the domain, which is almost impermeable, $k_{\mathrm{f,n}} = k_{\mathrm{f,t}} = 10^{-4}$. Furthermore, it contains a separated fracture network consisting of four fracture branches which share one crossing and end all within the domain. Those fractures are permeable, $k_{\mathrm{f,n}} = k_{\mathrm{f,t}} = 10^{4}$. Finally, there is a non-straight fracture connecting the upper and lower boundary, which has fracture branches ending inside the domain connected to it. This part of the fracture network has a Y-crossing and an X-crossing and is also permeable, $k_{\mathrm{f,n}} = k_{\mathrm{f,t}} = 10^{4}$. All fractures have the same aperture $d = 10^{-4}$.

The DFM model is not able to capture the influence of the almost impermeable fracture on the flow field correctly and also cannot compute the fracture pressure within the almost impermeable fracture correctly, figure 7.10. The reference solution is computed, due to the complexity of the fracture network, on an unstructured simplex grid. The cell-centered solution plot along a line shows thus oscillations which depend on the grid. To be able to better compare the reference solution to the solution of other models, also an interpolated (cubic spline) solution is plotted in figure 7.10b. The XFEM model, with only 899 degrees of freedom, matches the reference solution quite well, including the pressure jump across the fracture and the pressure within the fracture.

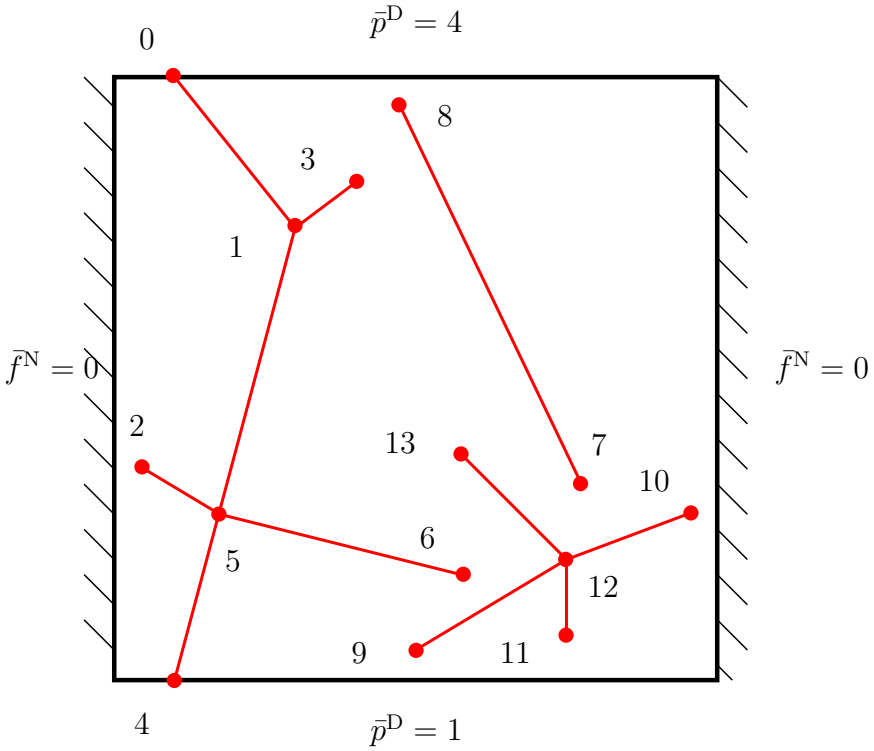

Figure 7.8: Example 9: Domain and boundary conditions

Table 7.3: Example 9: Domain coordinates

node	0	1	2	3	4	5	6
x	0.100	0.300	0.005	0.400	0.100	0.200	0.550
y	1.000	0.695	0.400	0.750	0.000	0.310	0.210
node	7	8	9	10	11	12	13
x	0.800	0.450	0.500	0.950	0.750	0.750	0.600
y	0.300	0.950	0.050	0.300	0.100	0.225	0.400

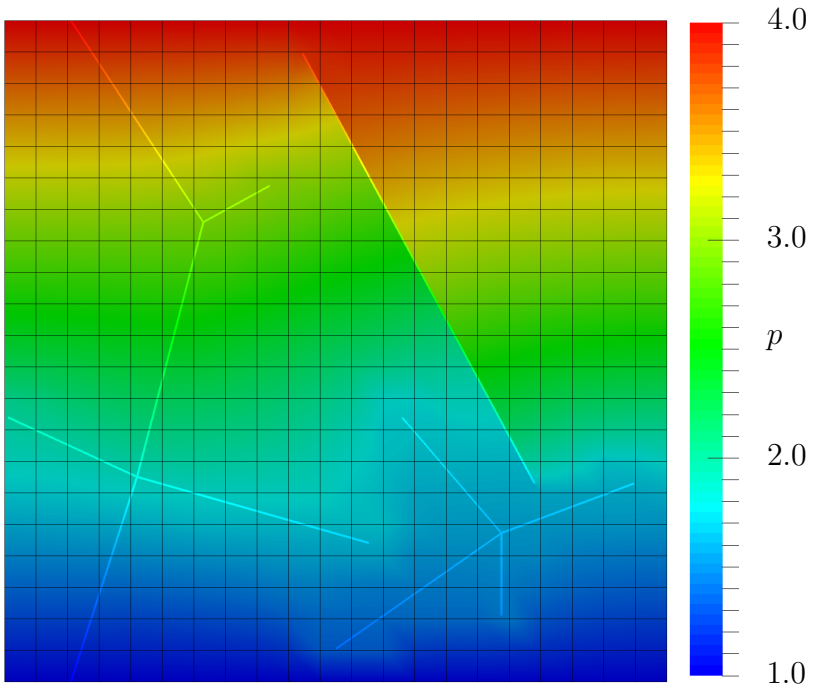

Figure 7.9: Example 9: XFEM pressure solutions, matrix and fractures

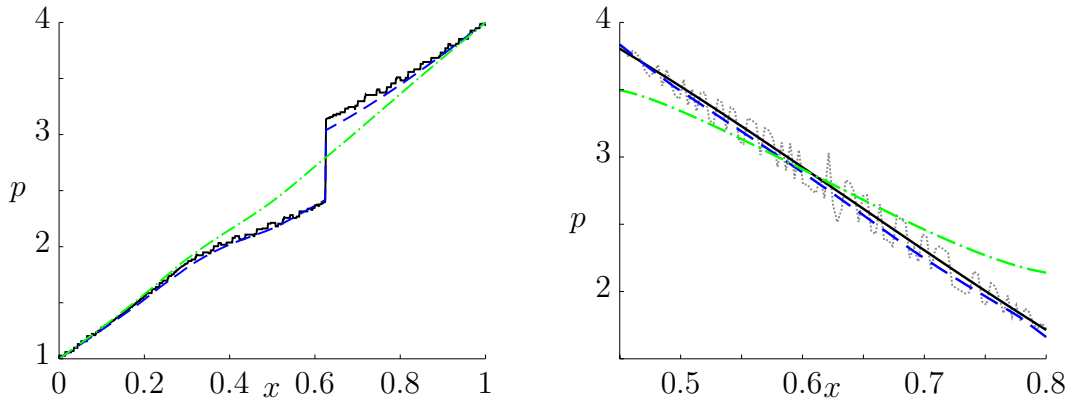

a matrix pressure **b** fracture pressure

Figure 7.10: Example 9: Pressure in the matrix along a diagonal line $(0,0)$–$(1,1)$ and in the upper right fracture $(0.45,0.95)$–$(0.8,0.3)$; black solid: Reference MFD interpolated, gray dotted: Cell centered MFD, dashed blue: XFEM, dash-dotted green: DFM

7.5 Summary

Several examples are presented and corresponding solutions of different models and numerical methods are compared. For highly conductive fractures and simple to grid fracture networks the DFM model shows its strengths. The XFEM model can match the reference solution, but in some cases it needs more degrees of freedom than the DFM to achieve comparable results. The advantage of independent fracture and matrix grids is clearly visible and leads in most cases to a huge advantage over a uniform refinement. The LM model does not show competitive results for the examples presented here. For fractures with a lower permeability than the matrix, the DFM model is not able to capture the flow field correctly and the XFEM model shows very accurate results on relatively coarse grids.

8 Final Remarks

In this work, a lower-dimensional model concept for porous media fractures embedded in a surrounding matrix is presented. It is implemented based on the XFEM which makes it possible to have grid-independent discontinuous solutions in the matrix and therefore, to have completely independent grids for fracture network and rock matrix. For three special cases, the standard model based on Martin et al. (2005), is extended.

Ending Fractures A coupling concept at the fracture tip and the XFEM implementation is presented. In a validation test case the XFEM model is able to reproduce the reference solution. It is computationally more effective than the established model, because the grid creation is carried out with almost no computational efforts and furthermore, a significant reduction in degrees of freedom is possible leading to visually the same results.

Fracture Crossings The conceptual model is extended to handle fracture crossings of arbitrary number, intersection angles, and arbitrary permeabilities. It shows robust behavior for the presented implementation. Different examples for highly conductive as well as almost impermeable fractures show numerical convergence and physical flow behavior. A comparison to a classical groundwater flow benchmark is conducted and shows the efficiency as well as accuracy of the presented conceptual model and its implementation.

Boundary Conditions Furthermore, a new method to interpolate pressure distributions on boundaries with fractures is presented. Those interpolated pressure distributions can be used as Dirichlet boundary condition values. Depending on the problem to simulate and the given data, the interpolation can calculate the fracture pressures or take them as additional input to give an even better approximation of the pressure distribution on the boundaries. The presented example shows the influence of the boundary conditions and the advantage of the novel approach.

The model developed in this work, combines the advantages of lower-dimensional models and non-matching grids while keeping the ability to represent the fracture geometry and its influence on the matrix flow field exactly. Therefore, it is an efficient alternative to established models for the simulation of fractured porous-media systems with complex fracture network geometries which require the explicit treatment of the fractures and the matrix flow.

Outlook

In general, the presented model shows a great potential for the simulation of complex fractured porous media systems. However, to become applicable to industry simulation problems, a lot more special cases of fractures intersecting matrix-grid elements and an extension to 3d has to be implemented. Based on the tests and validation approaches for the three aforementioned model extension, the following future work is possible.

So far, the system was always solved directly. For larger applications, however, iterative solvers become more efficient and thus interesting. In the current implementation they do not converge for all permeability ratios. There exists potential for improvement.

For fractures ending inside the domain, the case of fractures permeable in tangential and almost impermeable in normal direction shows significant differences between all the compared models and thus, there is space for improvement possibly in the conceptual but also in the tip treatment of the numerical (XFEM) model. The

case of a projected intersection edge neighboring a real intersection edge and the corresponding implementation can be investigated further and the error quantified. A possible enrichment alternative and coupling concept for the fracture tip is suggested but the implementation and validation remains future work.

For the validation of the boundary-condition interpolation method a comparison against experimental data is highly recommended.

Transport Simulations

In the presented work, the elliptic pressure equation is solved for heterogeneous, fractured porous media systems. For most applications, a transport simulation is of interest. To be able to conduct a meaningful transport simulation, e.g., of a conservative tracer, the fluxes and velocities have to be calculated. The implemented finite element approach does not give face velocities directly, because of the chosen bi-linear Lagrangian basis.

The easiest way to use the advantages of the newly developed pressure solver for transport simulations, is to apply it in the context of a decoupled, IMPET (implicit pressure explicit transport) method. The first idea is, to use the simulation toolbox DuMu^{x} to handle the velocity calculation and transport simulation. To couple the XFEM pressure solution to DuMu^{x}, a grid has to be defined which DuMu^{x} can use. This is of course not optimal, because the advantage of independent fracture and matrix grids and simulations for the pressure field is lost for the transport simulation. An ad-hoc implementation of this idea did not lead to success, because of the very small fracture elements which lead to a significant restriction of the time step size through the CFL criterion. An IMPSAT-based approach might be appropriate. The remaining restriction is then the restriction of decoupling the pressure and transport equation itself. A good overview of IMPSAT and IMPET is for example given in Haukås (2006). Another alternative to the DuMu^{x} compatible grid creation is the implementation of an extended Finite Volume Method, (Fumagalli and Scotti 2013).

Alternatively, the pressure field can be used to reconstruct a velocity field, which is locally mass conservative, e.g., (Cockburn et al. 2008). The difficulty lies here mainly in the matrix elements which are not cut by a fracture and the regular edges of cut elements. The fluxes and velocities between the fracture and matrix domain are implicitly given and the gradients of the basis is in general well defined at the interface of fracture and matrix. The reconstructed velocity field could then be used to apply an efficient grid independent transport solver, e.g., a Lagrangian based particle tracking algorithm.

Forchheimer Flow in the Fractures

If the fractures are highly conductive, the flow might not be considered anymore as Darcy flow, i.e., inertia effects are not to be neglected. This can occur in many applications in earth sciences. In most cases, the main interest still does not lie on a scale where (Navier-) Stokes equations are applicable. Because of computational efficiency, the standard way to simulate inertia effects on the Darcy scale, is the extension of Darcy's law which is called Forchheimer equation. Due to the high modularity and grid independence of the model presented here it is relatively easy to include Forchheimer's equation into the current implementation. The theoretical change in the coupling conditions was carried out in Crawford-Jones (2013).

Iterative Coupling of Fracture and Rock Matrix Flow

The separation of the fracture problem matrix problem suggests to solve the global problem not monolithically but iteratively instead. A first step towards iterative coupling was carried out in Oueslati (2013). Unfortunately, at the time of that thesis, the main implementation was not correct and the results found, should be re-evaluated. The decoupled problem might lead to interesting preconditioners for large scale applications.

Bibliography

Abdelaziz, Y. and Hamouine, A. (2008). A survey of the extended finite element. *Computers & structures*, 86(11-12):1141–1151.

Acosta, M., Merten, C., Eigenberger, G., Class, H., Helmig, R., Thoben, B., and Müller-Steinhagen, H. (2006). Modeling non-isothermal two-phase multi-component flow in the cathode of PEM fuel cells. *Journal of power sources*, 159(2):1123–1141.

Agnarsson, G. (2007). *Graph theory: modeling, applications, and algorithms*. Pearson, Prentice Hall, Upper Saddle River, NJ, international edition.

Alboin, C., Jaffré, J., Roberts, J. E., and Serres, C. (1999). Domain decomposition for flow in porous media with fractures. Citeseer.

Alboin, C., Jaffré, J., Roberts, J. E., and Serres, C. (2002). Modeling fractures as interfaces for flow and transport in porous media. In *Fluid Flow and Transport in Porous Media, Mathematical and Numerical Treatment: Proceedings of an AMS-IMS-SIAM Joint Summer Research Conference on Fluid Flow and Transport in Porous Media, Mathematical and Numerical Treatment, June 17-21, 2001, Mount Holyoke College, South Hadley, Massachusetts*, volume 295, pages 13–25. American Mathematical Soc.

Angot, P. (2003). A model of fracture for elliptic problems with flux and solution jumps. *Comptes Rendus Mathematique*, 337(6):425–430.

Angot, P., Boyer, F., Hubert, F., et al. (2009). Asymptotic and numerical modelling of flows in fractured porous media. *Modelisation Mathématique et Analyse Numérique*, 23(2):239–275.

Assteerawatt, A. (2008). *Flow and transport modelling of fractured aquifers based on a geostatistical approach*. PhD thesis, Universität Stuttgart.

Barthélémy, J.-F. (2009). Effective permeability of media with a dense network of long and micro fractures. *Transport in Porous Media*, 76(1):153–178.

Basquet, R., Cohen, C. E., and Bourbiaux, B. (Bahrain, March 12-15, 2005). Fracture Flow Property Identification: An Optimized Implementation of Discrete Fracture Network Models. *14th SPE Middle East Oil and Gas Show and Conference*.

Bastian, P., Birken, K., Johannsen, K., Lang, S., Neuß, N., Rentz-Reichert, H., and Wieners, C. (1997). UG – A flexible software toolbox for solving partial differential equations. *Computing and Visualization in Science*, 1(1):27–40.

Bastian, P., Blatt, M., Dedner, A., Engwer, C., Klöfkorn, R., Kornhuber, R., Ohlberger, M., and Sander, O. (2008a). A generic grid interface for parallel and adaptive scientific computing. Part II: Implementation and tests in DUNE. *Computing*, 82(2-3):121–138.

Bastian, P., Blatt, M., Dedner, A., Engwer, C., Klöfkorn, R., Ohlberger, M., and Sander, O. (2008b). A generic grid interface for parallel and adaptive scientific computing. Part I: Abstract framework. *Computing*, 82(2-3):103–119.

Bastian, P., Buse, G., and Sander, O. (2010a). Infrastructure for the coupling of DUNE grids. In *Numerical Mathematics and Advanced Applications 2009*, pages 107–114. Springer.

Bastian, P., Heimann, F., and Marnach, S. (2010b). Generic implementation of finite element methods in the distributed and unified numerics environment (DUNE). *Kybernetika*, 46(2):294–315.

Bathe, K.-J. (2006). *Finite element procedures*. Klaus-Jürgen Bathe.

Bear, J. (1988). *Dynamics of fluids in porous media*. Dover publications.

Bear, J., Tsang, C. F., and Marsily, G. (1993). *Flow and contaminant transport in fractured rocks*. Academic Press, San Diego, CA (United States).

Belayneh, M., Geiger, S., and Matthäi, S. (2006). Numerical simulation of water injection into layered fractured carbonate reservoir analogs. *AAPG bulletin*, 90(10):1473.

Berkowitz, B. (2002). Characterizing flow and transport in fractured geological media: A review. *Advances in Water Resources*, 25(8-12):861–884.

Berrone, S., Pieraccini, S., and Scialò, S. (2013). On simulations of discrete fracture network flows with an optimization-based extended finite element method. *SIAM Journal on Scientific Computing*, 35(2):A908–A935.

Blatt, M. and Bastian, P. (2007). The iterative solver template library. In B. Kåström, E. Elmroth, J. D. and Wasniewski, J., editors, *Applied Parallel Computing. State of the Art in Scientific Computing*, pages 666–675. Springer.

Borgia, A., Pruess, K., Kneafsey, T. J., Oldenburg, C. M., and Pan, L. (2012). Numerical simulation of salt precipitation in the fractures of a CO_2-enhanced geothermal system. *Geothermics*, 44:13–22.

Bourbiaux, B., Basquet, R., Cacas, M. C., Daniel, J. M., and Sarda, S. (2002). An integrated workflow to account for multi-scale fractures in reservoir simulation models: implementation and benefits. In *Abu Dhabi International Petroleum Exhibition and Conference*.

Braess, D. (2007). *Finite elements: Theory, fast solvers, and applications in solid mechanics*. Cambridge University Press.

Burman, E. and Hansbo, P. (2012). Fictitious domain finite element methods using cut elements: II. A stabilized Nitsche method. *Applied Numerical Mathematics*, 62(4):328–341.

Cockburn, B., Gopalakrishnan, J., and Wang, H. (2008). Locally conservative fluxes for the continuous galerkin method. *SIAM Journal on Numerical Analysis*, 45(4):1742–1776.

Crawford-Jones, W. (2013). Extending a fracture-matrix model towards Forchheimer flow in the fracture network. Independent study, Department of Hydromechanics and Modelling of Hydrosystems, University of Stuttgart.

D'Angelo, C. and Scotti, A. (2012). A mixed finite element method for darcy flow in fractured porous media with non-matching grids. *ESAIM: Mathematical Modelling and Numerical Analysis*, 46(02):465–489.

Darcy, H. (1856). *Les fontaines publiques de la ville de Dijon. Exposition et application des principes à suivre et des formules à employer dans les questions de distribution d'eau: ouvrage terminé par un appendice relatif aux fournitures d'eau de plusieurs villes au filtrage des eaux et à la fabrication des tuyaux de fonte, de plomb, de tole et de bitume*. Dalmont.

Dietrich, P., Helmig, R., Sauter, M., Hötzl, H., Köngeter, J., and Teutsch, G. (2005). *Flow and transport in fractured porous media*. Springer.

Dogan, M. O., Class, H., and Helmig, R. (2009). Different concepts for the coupling of porous-media flow with lower-dimensional pipe flow. *CMES: Computer Modeling in Engineering & Sciences*, 53(3):207–234.

Dolbow, J. (1999). *An extended finite element method with discontinuous enrichment for applied mechanics*. PhD thesis, Northwestern University.

Dolbow, J., Moës, N., and Belytschko, T. (2000). Discontinuous enrichment in finite elements with a partition of unity method. *Finite Elements in Analysis and Design*, 36(3-4):235–260.

Erbertseder, K., Reichold, J., Helmig, R., Jenny, P., and Flemisch, B. (2012). A coupled discrete/continuum model for describing cancer therapeutic transport in the lung. *PLoS ONE*, 7(3):e31966.

Ern, A. (2004). *Theory and practice of finite elements*, volume 159. Springer.

Evans, L. C. (1998). Partial differential equations. Graduate studies in mathematics. *American mathematical society*, 2.

Flemisch, B. (2013). Tackling coupled problems in porous media: Development of numerical models and an open source simulator. Habilitation.

Flemisch, B., Darcis, M., Erbertseder, K., Faigle, B., Lauser, A., Mosthaf, K., Müthing, S., Nuske, P., Tatomir, A., Wolff, M., and Helmig, R. (2011). DuMu^{x}: DUNE for multi-{phase, component, scale, physics, ...} flow and transport in porous media. *Advances in Water Resources*.

Formaggia, L., Fumagalli, A., Scotti, A., and Ruffo, P. (2012). A reduced model for Darcy's problem in networks of fractures. *MOX report 32*.

Fox, D. B., Sutter, D., Beckers, K. F., Lukawski, M. Z., Koch, D. L., Anderson, B. J., and Tester, J. W. (2013). Sustainable heat farming: Modeling extraction and recovery in discretely fractured geothermal reservoirs. *Geothermics*, 46:42–54.

Fries, T. (2008). A corrected XFEM approximation without problems in blending elements. *International Journal for Numerical Methods in Engineering*, 75(5):503–532.

Fumagalli, A. and Scotti, A. (2012). An efficient XFEM approximation of Darcy flows in fractured porous media. *MOX report 53*.

Fumagalli, A. and Scotti, A. (2013). A numerical method for two-phase flow in fractured porous media with non-matching grids. *Advances in Water Resources*, 62:454–464.

Gebauer, S., Neunhäuserer, L., Kornhuber, R., Ochs, S., Hinkelmann, R., and Helmig, R. (2002). Equidimensional modelling of flow and transport processes in fractured porous systems I. *Developments in Water Science*, 47:335–342.

Geiger, S., Dentz, M., and Neuweiler, I. (2011). A novel multi-rate dual-porosity model for improved simulation of fractured and multi-porosity reservoirs. In *SPE Reservoir Characterisation and Simulation Conference and Exhibition*.

Hackbusch, W. and Sauter, S. A. (1997). Composite finite elements for the approximation of PDEs on domains with complicated micro-structures. *Numerische Mathematik*, 75(4):447–472.

Hægland, H., Assteerawatt, A., Dahle, H. K., Eigestad, G. T., and Helmig, R. (2009). Comparison of cell- and vertex-centered discretization methods for flow in a two-dimensional discrete-fracture-matrix system. *Advances in Water Resources*, 32(12):1740–1755.

Hansbo, A. and Hansbo, P. (2002). An unfitted finite element method, based on Nitsche's method, for elliptic interface problems. *Computer methods in applied mechanics and engineering*, 191(47-48):5537–5552.

Hansbo, A. and Hansbo, P. (2004). A finite element method for the simulation of strong and weak discontinuities in solid mechanics. *Computer methods in applied mechanics and engineering*, 193(33):3523–3540.

Hansbo, P. (2005). Nitsche's method for interface problems in computational mechanics. *GAMM-Mitteilungen*, 28(2):183–206.

Haukås, J. (2006). *Compositional reservoir simulation with emphasis on the IMPSAT formulation.* PhD thesis, University of Bergen.

Helmig, R. (1997). *Multiphase flow and transport processes in the subsurface: A contribution to the modeling of hydrosystems.* Springer.

Hou, T. Y. and Wu, X. H. (1997). A multiscale finite element method for elliptic problems in composite materials and porous media. *Journal of computational physics*, 134(1):169–189.

Huang, H., Long, T. A., Wan, J., and Brown, W. P. (2011). On the use of enriched finite element method to model subsurface features in porous media flow problems. *Computational Geosciences*, 15(4):721–736.

Hubbert, M. K. (1957). Darcy's law and the field equations of the flow of underground fluids. *Hydrological Sciences Journal*, 2(1):23–59.

Hughes, T. J. R., Feijóo, G. R., Mazzei, L., and Quincy, J. B. (1998). The variational multiscale method – a paradigm for computational mechanics. *Computer methods in applied mechanics and engineering*, 166(1-2):3–24.

Jenny, P., Lee, S. H., and Tchelepi, H. A. (2005). Adaptive multiscale finite-volume method for multiphase flow and transport in porous media. *Multiscale Modeling and Simulation*, 3(1):50–64.

Joyce, S., Hartley, L., Applegate, D., Hoek, J., and Jackson, P. (2014). Multi-scale groundwater flow modeling during temperate climate conditions for the safety assessment of the proposed high-level nuclear waste repository site at Forsmark, Sweden. *Hydrogeology Journal*, 22(6):1233–1249.

Karimi-Fard, M., Gong, B., and Durlofsky, L. J. (2006). Generation of coarse-scale continuum flow models from detailed fracture characterizations. *Water Resources Research*, 42(10):10423.

Köppel, M. (2013). Flow modelling of coupled fracture-matrix porous media systems with a two mesh concept. Master's thesis, Pomdapi INRIA Rocquencourt.

Lee, S. H., Lough, M. F., and Jensen, C. L. (2001). Hierarchical modeling of flow in naturally fractured formations with multiple length scales. *Water Resources Research*, 37(3):443–455.

Leeuwen, J. V., Meyer, A., Nival, M., et al. (1990). *Handbook of theoretical computer science: Algorithms and complexity*. MIT Press.

Li, X., Demmel, J., Gilbert, J., iL. Grigori, Shao, M., and Yamazaki, I. (1999). SuperLU Users' Guide. Technical Report LBNL-44289, Lawrence Berkeley National Laboratory. `http://crd.lbl.gov/~xiaoye/SuperLU/`. Last update: August 2011.

Li, X. S. (2005). An overview of SuperLU: Algorithms, implementation, and user interface. *ACM Transactions on Mathematical Software*, 31(3):302–325.

Liu, J., Chen, Z., Elsworth, D., Qu, H., and Chen, D. (2011). Interactions of multiple processes during CBM extraction: A critical review. *International Journal of Coal Geology*, 87(3):175–189.

Martin, V., Jaffré, J., and Roberts, J. E. (2005). Modeling fractures and barriers as interfaces for flow in porous media. *SIAM Journal on Scientific Computing*, 26(5):1667–1691.

Matthäi, S. K. and Belayneh, M. (2004). Fluid flow partitioning between fractures and a permeable rock matrix. *Geophysical Research Letters*, 31(7):7602–6.

Meyer, T. (2014). Comparison of models for fracture tips. Bachelor's Thesis, Department of Hydromechanics and Modelling of Hydrosystems, University of Stuttgart.

Misra, J. and Gries, D. (1992). A constructive proof of Vizing's theorem. *Information Processing Letters*, 41(3):131–133.

Mohammadi, S. (2008). *Extended finite element method*. John Wiley & Sons.

Monteagudo, J. and Firoozabadi, A. (2004). Control-volume method for numerical simulation of two-phase immiscible flow in two- and three-dimensional discrete-fractured media. *Water Resources Research*, 40:W07405.

Müthing, S. (2014). DUNE-MULTIDOMAIN. `https://gitorious.org/dune-multidomain`. Last accessed: August 2014.

Müthing, S. and Bastian, P. (2012). DUNE-MULTIDOMAINGRID: A metagrid approach to subdomain modeling. In *Advances in DUNE*, pages 59–73. Springer.

Neunhäuserer, L. (2003). *Diskretisierungsansätze zur Modellierung von Strömungs- und Transportprozessen in geklüftet-porösen Medien*. PhD thesis, Universität Stuttgart.

Nield, D. A. and Bejan, A. (2006). *Convection in porous media*. Springer, New York, N.Y., 3. ed. edition.

Nordbotten, J. M. (2009). Adaptive variational multiscale methods for multiphase flow in porous media. *Multiscale Modeling & Simulation*, 7:1455.

Nordbotten, J. M. and Bjørstad, P. E. (2008). On the relationship between the multiscale finite-volume method and domain decomposition preconditioners. *Computational Geosciences*, 12(3):367–376.

Oueslati, M. (2013). Comparison of monolithic and iterative solvers for coupled fracture-network rock-matrix porous media problems. Bachelor's Thesis, Department of Hydromechanics and Modelling of Hydrosystems and Institute of Aerodynamics and Gas Dynamics, Universität Stuttgart.

Pruess, K. (1992). Brief guide to the MINC-method for modeling flow and transport in fractured media. Technical report, Lawrence Berkeley Lab., CA (United States).

Qian, J., Zhou, X., Zhan, H., Dong, H., and Ma, L. (2014). Numerical simulation and evaluation of groundwater resources in a fractured chalk aquifer: A case study in Zinder well field, Niger. *Environmental Earth Sciences*, pages 1–13.

Rechard, R. P., Birkholzer, J. T., Wu, Y.-S., Stein, J. S., and Houseworth, J. E. (2014). Unsaturated flow modeling in performance assessments for the Yucca Mountain disposal system for spent nuclear fuel and high-level radioactive waste. *Reliability Engineering & System Safety*, 122:124–144.

Reichenberger, V., Jakobs, H., Bastian, P., and Helmig, R. (2006). A mixed-dimensional finite volume method for two-phase flow in fractured porous media. *Advances in Water Resources*, 29(7):1020–1036.

Roth, K. (2007). Soil physics lecture notes. Technical Report 1.2, University of Heidelberg, Institute of Environmental Physics, D-69120 Heidelberg, Germany.

Sandve, T. H., Berre, I., and Nordbotten, J. M. (2012). An efficient multi-point flux approximation method for discrete fracture–matrix simulations. *Journal of Computational Physics*.

Schmid, K. and Geiger, S. (2012). Universal scaling of spontaneous imbibition for water-wet systems. *Water Resources Research*, 48(3).

Schmidt, A. and Siebert, K. G. (2005). *Design of adaptive finite element software*, volume 42. Springer.

Schott, B. (2010). Enforcing interface conditions with Nitsche's method in the XFEM. Master's thesis, Technische Universität München.

Schwenck, N., Flemisch, B., Helmig, R., and Wohlmuth, B. I. (2014). Dimensionally reduced flow models in fractured porous media: Crossings and boundaries. *Submitted and NUPUS preprint 2014/5*.

Schwenck, N., Tatomir, A., Köppel, M., Flemisch, B., and Helmig, R. (2015). Comparison of lower- and equidimensional, discrete and embedded models for fractured porous media flow. *In preparation*.

Silberhorn-Hemminger, A. (2002). *Modellierung von Kluftaquifersystemen: Geostatistische Analyse und deterministisch-stochastische Kluftgenerierung*. PhD thesis.

Süß, M. (2005). *Analysis of the influence of structures and boundaries on flow and transport processes in fractured porous media*. PhD thesis, Universität Stuttgart.

Swedish Nuclear Power Inspectorate (SKI) (1987). The international hydrocoin project–background and results. *Paris, France: Organization for Economic Co-operation and Development*.

Tatomir, A. B., Szymkiewicz, A., Class, H., and Helmig, R. (2011). Modeling two phase flow in large scale fractured porous media with an extended multiple interacting continua method. *Computer Modeling in Engineering and Sciences*, 77(2):81–112.

Torabi, F., Qazvini Firouz, A., Kavousi, A., and Asghari, K. (2012). Comparative evaluation of immiscible, near miscible and miscible CO_2 huff-n-puff to enhance oil recovery from a single matrix–fracture system (experimental and simulation studies). *Fuel*, 93:443–453.

Tunc, X., Faille, I., Gallouët, T., Cacas, M. C., and Havé, P. (2012). A model for conductive faults with non-matching grids. *Computational Geosciences*, 16(2):277–296.

Vitel, S. and Souche, L. (Houston, Texas, USA, February 26-28, 2007). Unstructured Upgridding and Transmissibility Upscaling for Preferential Flow Paths in 3D Fractured Reservoirs. *SPE Reservoir Simulation Symposium*.

Weatherill, D., Graf, T., Simmons, C. T., Cook, P. G., Therrien, R., and Reynolds, D. A. (2008). Discretizing the fracture-matrix interface to simulate solute transport. *Ground Water*, 46(4):606–615.

Wen, X., Durlofsky, L., and Edwards, M. (2003). Use of border regions for improved permeability upscaling. *Mathematical Geology*, 35(5):521–547.

Wolff, M. (2013). *Multi-scale modeling of two-phase flow in porous media including capillary pressure effects*. PhD thesis, Universität Stuttgart, Holzgartenstr. 16, 70174 Stuttgart.

Wu, Y. S., Zhang, K., Ding, C., Pruess, K., Elmroth, E., and Bodvarsson, G. S. (2002). An efficient parallel-computing method for modeling nonisothermal multiphase flow and multicomponent transport in porous and fractured media. *Advances in Water Resources*, 25(3):243–261.

A Equations

A.1 Navier-Stokes Equations

$$-\frac{1}{\mu}\nabla p = \frac{1}{\nu}\boldsymbol{u}\cdot\nabla\boldsymbol{u} - \nabla\cdot(\,\nabla\boldsymbol{u}\,)$$

A.2 Hele-Shaw Flow

$$u_x^{\mathrm{HS}} = -\frac{1}{8\mu}(d^2 - 4y^2)\,\nabla\, p$$

$$Q = -\ell_z\frac{d^3}{12\mu}\,\nabla\, p \qquad \text{so that } k_x = \frac{d^2}{12}$$

B Lower Dimensional Operators and Equations

B.1 Tangential Operators

The tangential Laplacian on any rational function $f \in \mathbb{R}$ can be evaluated as:

$$\begin{aligned}\Delta_{\mathrm{t}} f = \nabla_{\mathrm{t}} \cdot (\ \nabla_{\mathrm{t}} f\ ) =& \nabla_{\mathrm{t}} \cdot (\ \nabla f - (\nabla f \cdot \boldsymbol{n})\boldsymbol{n}\ ) \\ =& \nabla_{\mathrm{t}} \cdot (\ \nabla f\ ) - \nabla_{\mathrm{t}} \cdot (\ (\nabla f \cdot \boldsymbol{n})\boldsymbol{n}\ ) \\ =& \nabla \cdot (\ \nabla f\ ) - \underbrace{[[\nabla \otimes (\ \nabla f\ )]_{\mathcal{J}} \cdot \boldsymbol{n}] \cdot \boldsymbol{n}}_{2} \\ & - \underbrace{\nabla \cdot (\ (\nabla f \cdot \boldsymbol{n})\boldsymbol{n}\ )}_{3} + \underbrace{[[\nabla \otimes (\ (\nabla f \cdot \boldsymbol{n})\boldsymbol{n}\ )]_{\mathcal{J}} \cdot \boldsymbol{n}] \cdot \boldsymbol{n}}_{4},\end{aligned}$$

where $[\nabla \otimes (\ \cdot\ )]_{\mathcal{J}}$ symbolizes the result of the operation inside is a matrix which results from a Dyadic product. Term 4 can be rewritten:

$$[[\nabla \otimes (\ (\nabla f \cdot \boldsymbol{n})\boldsymbol{n}\ )]_{\mathcal{J}} \cdot \boldsymbol{n}] \cdot \boldsymbol{n} = \nabla \cdot (\ ((\boldsymbol{n} \otimes \boldsymbol{n})(\boldsymbol{n} \cdot \boldsymbol{n}))\, \nabla f\ ),$$

so that follows terms two, three and four are equal, because $\boldsymbol{n}$ is the unit normal vector, so that always $\boldsymbol{n} \cdot \boldsymbol{n} = 1$.

In summary, that leads to

$$\Delta_{\mathrm{t}} f = \Delta f - \nabla \cdot (\ (\nabla f \cdot \boldsymbol{n})\boldsymbol{n}\ ).$$

B.2 Rotated Permeabilities

The rotation matrix is given as:

$$\boldsymbol{R} = \begin{pmatrix} \cos\theta & -\sin\theta \\ \sin\theta & \cos\theta \end{pmatrix}, \quad \boldsymbol{R}^{-1} = \begin{pmatrix} \cos\theta & \sin\theta \\ -\sin\theta & \cos\theta \end{pmatrix},$$

with $0 < \theta < 2\pi$.

The general permeability matrix is given as:

$$\boldsymbol{K} = \begin{pmatrix} k_{11} & k_{12} \\ k_{21} & k_{22} \end{pmatrix}.$$

Darcy's law and the continuity equation for incompressible flow leads to

$$\nabla \cdot \Big(\boldsymbol{R}(\theta)\, \boldsymbol{K}\, \boldsymbol{R}^{-1}(\theta)\, \nabla\, p \Big) = 0.$$

This can requires the rotated permeability matrix, which can be written as:

$$\boldsymbol{R}(\theta)\, \boldsymbol{K}\, \boldsymbol{R}^{-1}(\theta) = \begin{pmatrix} k_{11}\cos^2 + k_{22}\sin^2 - (k_{12}+k_{21})\sin\cos & (k_{11}-k_{22})\cos\sin + k_{12}\cos^2 - k_{21}\sin^2 \\ (k_{11}-k_{22})\cos\sin - k_{12}\sin^2 + k_{21}\cos^2 & k_{11}\sin^2 + k_{22}\cos^2 + (k_{12}+k_{21})\sin\cos \end{pmatrix},$$

or for the inverse rotation operation:

$$\boldsymbol{R}^{-1}(\theta)\, \boldsymbol{K}\, \boldsymbol{R}(\theta) = \begin{pmatrix} k_{11}\cos^2 + k_{22}\sin^2 + (k_{12}+k_{21})\sin\cos & -(k_{11}-k_{22})\cos\sin + k_{12}\cos^2 - k_{21}\sin^2 \\ -(k_{11}-k_{22})\cos\sin - k_{12}\sin^2 + k_{21}\cos^2 & k_{11}\sin^2 + k_{22}\cos^2 - (k_{12}+k_{21})\sin\cos \end{pmatrix}.$$

Assuming a symmetric matrix $k_{12} = k_{21}$ that reduces to:

$$\boldsymbol{R}(\theta)\,\boldsymbol{K}\,\boldsymbol{R}^{-1}(\theta) = \begin{pmatrix} k_{11}\cos^2 + k_{22}\sin^2 - 2k_{12}\sin\cos & (k_{11}-k_{22})\cos\sin + k_{12}(\cos^2-\sin^2) \\ (k_{11}-k_{22})\cos\sin + k_{12}(\cos^2-\sin^2) & k_{11}\sin^2 + k_{22}\cos^2 + 2k_{12}\sin\cos \end{pmatrix},$$

and for the inverse rotation operation:

$$\boldsymbol{R}^{-1}(\theta)\,\boldsymbol{K}\,\boldsymbol{R}(\theta) = \begin{pmatrix} k_{11}\cos^2 + k_{22}\sin^2 + 2k_{12}\sin\cos & -(k_{11}-k_{22})\cos\sin + k_{12}(\cos^2-\sin^2) \\ -(k_{11}-k_{22})\cos\sin + k_{12}(\cos^2-\sin^2) & k_{11}\sin^2 + k_{22}\cos^2 - 2k_{12}\sin\cos \end{pmatrix}.$$

Further assuming a diagonal matrix, $k_{12} = k_{21} = 0$, this leads to:

$$\boldsymbol{R}(\theta)\,\boldsymbol{K}\,\boldsymbol{R}^{-1}(\theta) = \begin{pmatrix} k_{11}\cos^2\theta + k_{22}\sin^2\theta & (k_{11}-k_{22})\cos\theta\sin\theta \\ (k_{11}-k_{22})\cos\theta\sin\theta & k_{11}\sin^2\theta + k_{22}\cos^2\theta \end{pmatrix},$$

and for the inverse rotation operation:

$$\boldsymbol{R}^{-1}(\theta)\,\boldsymbol{K}\,\boldsymbol{R}(\theta) = \begin{pmatrix} k_{11}\cos^2\theta + k_{22}\sin^2\theta & -(k_{11}-k_{22})\cos\theta\sin\theta \\ -(k_{11}-k_{22})\cos\theta\sin\theta & k_{11}\sin^2\theta + k_{22}\cos^2\theta \end{pmatrix}.$$

For an isotropic permeability, $k_{11} = k_{22} = k$, this condenses to:

$$\boldsymbol{R}(\theta)\,\boldsymbol{K}\,\boldsymbol{R}^{-1}(\theta) = \boldsymbol{R}^{-1}(\theta)\,\boldsymbol{K}\,\boldsymbol{R}(\theta) = k \cdot \mathbf{I},$$

so that p and $\boldsymbol{u}$ are not dependent on the rotation of the permeability matrix. However, for a diagonal, but anisotropic permeability, $k_{11} \neq k_{22}$, this shows that the velocities

$$u_x = -(k_{11}\cos^2\theta + k_{22}\sin^2\theta)\frac{\partial p}{\partial x} - (k_{11}\cos\theta\sin\theta - k_{22}\cos\theta\sin\theta)\frac{\partial p}{\partial y},$$

$$u_y = -(k_{11}\cos\theta\sin\theta - k_{22}\cos\theta\sin\theta)\frac{\partial p}{\partial x} - (k_{11}\sin^2\theta + k_{22}\cos^2\theta)\frac{\partial p}{\partial y},$$

as well as the pressure depends on the inclination θ

$$\begin{aligned} -(k_{11}\cos^2\theta + k_{22}\sin^2\theta)\frac{\partial^2 p}{\partial x^2} - 2(k_{11}\cos\theta\sin\theta - k_{22}\cos\theta\sin\theta)\frac{\partial^2 p}{\partial x \partial y} \\ -(k_{11}\sin^2\theta + k_{22}\cos^2\theta)\frac{\partial^2 p}{\partial y^2} = 0. \end{aligned} \tag{B.1}$$

For the case of $\theta = 0$ this condenses to the well known potential flow situation for incompressible flow in the plane, where the pressure is the potential, with the permeabilities as additional factors:

$$u_x = -k_{11}\frac{\partial p}{\partial x},$$

$$u_y = -k_{22}\frac{\partial p}{\partial y},$$

and:

$$k_{11}\frac{\partial^2 p}{\partial x^2} + k_{22}\frac{\partial^2 p}{\partial y^2} = 0.$$

B.3 Absolute Velocity

The absolute velocity in a rotated setting is given as:

$$\begin{aligned}\|\boldsymbol{u}\|^2 = u_x^2 + u_y^2 = \frac{\partial p}{\partial x}\frac{\partial p}{\partial y} 2\cos\theta\sin\theta(k_{11}^2 - k_{22}^2) \\ + \left(\frac{\partial p}{\partial x}\right)^2 (k_{11}^2\cos^2\theta + k_{22}^2\sin^2\theta) \\ + \left(\frac{\partial p}{\partial y}\right)^2 (k_{11}^2\sin^2\theta + k_{22}^2\cos^2\theta).\end{aligned}$$

The case of $\theta = 0$ leads to

$$\|\boldsymbol{u}\| = \sqrt{\left(k_{11}\frac{\partial p}{\partial x}\right)^2 + \left(k_{22}\frac{\partial p}{\partial y}\right)^2}.$$

B.4 Rotation of the Flow

A solution for (B.1) is

$$p = \mathrm{e}^{\alpha x + \beta y} \quad \text{with}$$

$$\alpha^2(k_{11}\cos^2\theta + k_{22}\sin^2\theta) + \beta^2(k_{11}\sin^2\theta + k_{22}\cos^2\theta) + 2\alpha\beta\cos\theta\sin\theta(k_{11} - k_{22}) = 0 \tag{B.2}$$

The assumption of an irrotational flow $\nabla \times \boldsymbol{u} = \frac{\partial u_y}{\partial x} - \frac{\partial u_x}{\partial y} \stackrel{!}{=} 0$ gives

$$\begin{aligned}\Big((k_{11} - k_{22})\cos^2\theta - (k_{11} - k_{22})\sin^2\theta\Big)\frac{\partial^2 p}{\partial x \partial y} \\ - (k_{11} - k_{22})\cos\theta\sin\theta\left(\frac{\partial^2 p}{\partial x^2} - \frac{\partial^2 p}{\partial y^2}\right) \stackrel{?}{=} 0,\end{aligned}$$

which is of course true for every θ if $k_{11} = k_{22}$.

For $k_{11} \neq k_{22}$

$$(\cos^2\theta - \sin^2\theta)\frac{\partial^2 p}{\partial x \partial y} - \cos\theta\sin\theta\left(\frac{\partial^2 p}{\partial x^2} - \frac{\partial^2 p}{\partial y^2}\right) \stackrel{!}{=} 0,$$

with

$$\frac{\partial^2 p}{\partial x^2} = \alpha^2 \mathrm{e}^{\alpha x+\beta y}, \quad \frac{\partial^2 p}{\partial y^2} = \beta^2 \mathrm{e}^{\alpha x+\beta y}, \quad \frac{\partial^2 p}{\partial x \partial y} = \alpha\beta \mathrm{e}^{\alpha x+\beta y},$$

that leads to:

$$\alpha\beta(\cos^2\theta - \sin^2\theta) - \cos\theta\sin\theta\left(\alpha^2 - \beta^2\right) \stackrel{!}{=} 0.$$

So that $\alpha = \cos\theta$ and $\beta = \sin\theta$. But inserting this into (B.2) leads to:

$$k_{11}\cos^4\theta + k_{22}\sin^2\theta\cos^2\theta + k_{11}\sin^4\theta + k_{22}\sin^2\theta\cos^2\theta + 2\cos^2\theta\sin^2\theta(k_{11} - k_{22}) \stackrel{!}{=} 0,$$

and

$$k_{11}(\cos^4\theta + \sin^4\theta) + 2k_{11}\cos^2\theta\sin^2\theta = 1 \neq 0.$$

This shows, that for an anisotropic diagonal permeability tensor the rotation is always not zero independent of theta.

For $\theta = 0$ this leads to:

$$p = \mathrm{e}^{\alpha x+\beta y} \quad \text{with } k_{11}\alpha^2 + k_{22}\beta^2 = 0,$$

so that

$$-k_{22}\frac{\partial^2 p}{\partial x \partial y} + k_{11}\frac{\partial^2 p}{\partial x \partial y} = (-k_{22} + k_{11})\alpha\beta \mathrm{e}^{\alpha x+\beta y} \stackrel{!}{=} 0,$$

with $\alpha \neq 0$ and $\beta \neq 0$ this is only true for $k_{11} = k_{22}$.

C Theorems and Algorithms

C.1 Theorems

Theorem C.1 (Vizing's)**.** *Let G be a simple graph, then*

$$\Delta(G) \leq \chi'(G) \leq \Delta(G) + 1$$

where $\chi'(G)$ is the edge cromatic number, which is the smallest number of different colors which are needed to colorize the edges in a way that only different colored edges share the same vertex. The maximum degree of all vertices in the graph is denoted by ΔG.

The problem to determine when $\Delta(G)$ colors are sufficient is not yet solved, (Agnarsson 2007).

C.2 Algorithms

```
function EdgeColoring(V, E, C) // V: set of vertices, E: set of edges, C: set of colors
    for all v_i ∈ V do
        exclude every v_i with Δ(v_i) ≤ 2 from V          // Δ(v_i): degree of v_i
        and combine the e_j adjacent to this v_i
    end for
    sort V by Δ(v_i) descending
    for all v_i ∈ V do
        C_i ← C                                   // C_i: set of colors available at v_i
        for all adjacent e_j do
            get c_j and remove it from C_i
        end for
        for all adjacent e_j do
            if e_j has no c_j then
                C_ij ← C_i                        // C_ij: set of colors available at v_i for e_j
                get v_j,op        // v_j,op: second vertex associated to e_j other than v_i
                for all e_k adjacent to v_j,op do
                    remove its c_k from C_ij
                end for
                set one c_j to e_j from available colors in C_ij
                remove c_j from C_i
            end if
        end for
    end for
end function
```

Algorithm C.2: edge coloring algorithm

```
function EdgeColoringGrid(V, E, C, Q_m^h)                    // Q_m^h: XFEM grid
    for all v_i ∈ V do
        exclude every v_i with Δ(v_i) ≤ 2 from V
        and combine the e_j adjacent to this v_i
    end for
    sort V by Δ(v_i) descending
    for all v_i ∈ V do
        C_i ← C
        for all adjacent e_j do
            get c_j and remove it from C_i
        end for
        for all adjacent e_j do
            if e_j has no c_j then
                C_ij ← C_i
                get v_j,op
                for all e_k adjacent to v_j,op do
                    remove its c_k from C_ij
                end for
                for all Q_m,k^h containing e_j do
                    if another e_l is contained then
                        remove its c_l from C_ij
                    end if
                end for
                set one c_j to e_j from available colors in C_ij
                remove c_j from C_i
            end if
        end for
    end for
end function
```

Algorithm C.3: grid dependent edge coloring algorithm

D Code Documentation

D.1 XFEM

For the modification of the matrix XFEM basis functions a map is stored which associates the matrix element id with geometrical information of the fractures cutting through that element. There are six different cases, cf. figure D.1. Case a and b are treated in the same way by adding a geometrical midpoint node for case a, so that one entry and one exit point and the midpoint is stored. In case c the ending point and the entry point is stored. For case d two entry and two exit points are stored. Cases e and f store one midpoint and three respectively four entry/exit points.

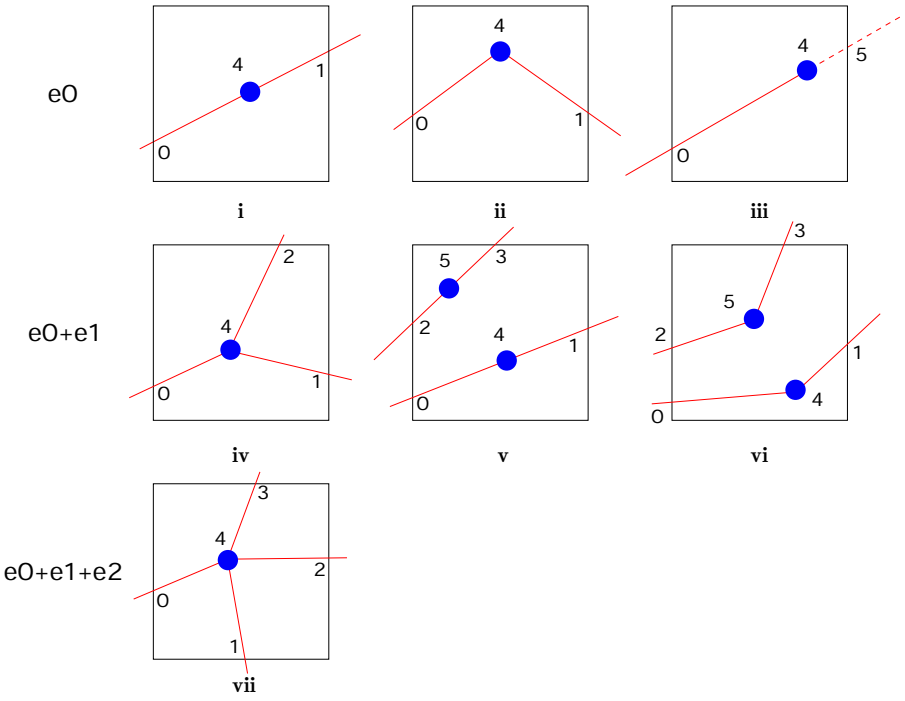

Figure D.1: Different intersection cases. The blue dots are not fracture grid nodes, but fracture nodes from the ART file. Except in the cases i, iii and v. In case i the entry in the position four, in case iii the entry in position five and in case v both entries in position four and five come from virtually added nodes, which are only there for an easier subtriangulation for the numerical integration. The roman numbers indicate the different cases (as in table D.1).

Table D.1: Zero to five indicate the index in intersectionPoints vector, roman one to six denote the different intersection cases as shown in figure D.1. The numbers in the table show at which iteration over the that matrix element the respective entry is written into the intersectionPoints vector.

	0	1	2	3	4	5
i	0	0			0	
ii	0	1			0	
iii	0				0	e
iv	0	1	2		0	
v	0	0	1	1	0	1
vi	0	1 or 2 or 3	1 or 2	2 or 3	0	1 or 2
vii	0	1	2	3	0	

D.2 Repository and Used DUNE Versions

The model concept code and all examples are publicly available (under a GPL license) in dumux-pub/Schwenck2015a, revision 14380.

Table D.2: Repository and used DUNE versions

module	revision
dune-common	073167e61070a5e952c738c02d85c3f946717e40
dune-geometry	f4a7f1d0f1ff8b3ed24af4e6366ca59216f158ae
dune-grid	995998a4e09c390ed32eb321685fc588be33e683
dune-istl	6c1bb5f7d89b555cab846305f784ee2a1b324eb6
dune-localfunctions	0f7ddb5b4955eefd346766de99f7779aa6801ecc
dune-multidomain	58257c38bb21046188aa8f2ca5b5578d8d568a92
dune-multidomaingrid	2cbed41f213ec52c666a569b18f0b057262ece00
dune-pdelab	23ba0444da18f048e7fc841516133a54917fec34
dune-typetree	9c2e89d9039bb6fb78b87805d98e3e9585b97509
dumux-devel	13665

Lebenslauf

Persönliche Daten

Name	Nicolas Schwenck
Geburtsdatum	15. Oktober 1983
Geburtsort	Hildesheim, Niedersachsen
Familienstand	ledig

Schulbildung

08/1996 – 06/2003 **Gymnasium Sophienschule Hannover**.

Studium

09/2004 **Beginn des Studiums der Luft- und Raumfahrttechnik (Diplom)**.

09/2006 **Vordiplom**, *danach Vertiefungsrichtungen „Statik und Dynamik“ und „Strömungslehre“*.

08/2008 – 12/2008 **Studienarbeit**, *„OpenSim – Evaluating an Open Source Simulation Software for Human Movements“*, KTH Stockholm, Prof. Dr. Techn. A. Eriksson.

08/2009– 02/2010 **Diplomarbeit**, *im Bereich „Direkte Numerische Simulation von Grenzschichtproblemen“*, am Institut für Aero- und Gasdynamik der Luft- und Raumfahrttechnik, Universität Stuttgart in Zusammenarbeit mit TU Wien, Apl. Prof. Dr.-Ing. U. Rist, Ao.Univ.Prof. Dipl.-Ing. Dr.techn. S. Braun.

Berufserfahrung

seit 03/2010 **Wissenschaftlicher Mitarbeiter**, *Institut für Wasse- und Umweltsystemmodellierung, Universität Stuttgart*, Mitglied in der „International Research Training Group NUPUS“, Thema: Numerische Methoden für geklüftete poröse Medien.

Institut für Wasser- und Umweltsystemmodellierung
Universität Stuttgart

Pfaffenwaldring 61
70569 Stuttgart (Vaihingen)
Telefon (0711) 685 - 64717/64749/64752/64679
Telefax (0711) 685 - 67020 o. 64746 o. 64681
E-Mail: iws@iws.uni-stuttgart.de
http://www.iws.uni-stuttgart.de

Direktoren
Prof. Dr. rer. nat. Dr.-Ing. András Bárdossy
Prof. Dr.-Ing. Rainer Helmig
Prof. Dr.-Ing. Silke Wieprecht

Vorstand *(Stand 03.11.2014)*
Prof. Dr. rer. nat. Dr.-Ing. A. Bárdossy
Prof. Dr.-Ing. R. Helmig
Prof. Dr.-Ing. S. Wieprecht
Prof. Dr. J.A. Sander Huisman
Jürgen Braun, PhD
apl. Prof. Dr.-Ing. H. Class
Dr.-Ing. H.-P. Koschitzky
Dr.-Ing. M. Noack
Prof. Dr.-Ing. W. Nowak
Dr. rer. nat. J. Seidel
Dr.-Ing. K. Terheiden
Dr.-Ing. habil. Sergey Oladyshkin

Emeriti
Prof. Dr.-Ing. habil. Dr.-Ing. E.h. Jürgen Giesecke
Prof. Dr.h.c. Dr.-Ing. E.h. Helmut Kobus, PhD

Lehrstuhl für Wasserbau und Wassermengenwirtschaft
Leiter: Prof. Dr.-Ing. Silke Wieprecht
Stellv.: Dr.-Ing. Kristina Terheiden
Versuchsanstalt für Wasserbau
Leiter: Dr.-Ing. Markus Noack

Lehrstuhl für Hydromechanik und Hydrosystemmodellierung
Leiter: Prof. Dr.-Ing. Rainer Helmig
Stellv.: apl. Prof. Dr.-Ing. Holger Class

Lehrstuhl für Hydrologie und Geohydrologie
Leiter: Prof. Dr. rer. nat. Dr.-Ing. András Bárdossy
Stellv.: Dr. rer. nat. Jochen Seidel
Hydrogeophysik der Vadosen Zone
(mit Forschungszentrum Jülich)
Leiter: Prof. Dr. J.A. Sander Huisman

Lehrstuhl für Stochastische Simulation und Sicherheitsforschung für Hydrosysteme
Leiter: Prof. Dr.-Ing. Wolfgang Nowak
Stellv.: Dr.-Ing. habil. Sergey Oladyshkin

***VEGAS,* Versuchseinrichtung zur Grundwasser- und Altlastensanierung**
Leitung: Jürgen Braun, PhD, AD
Dr.-Ing. Hans-Peter Koschitzky, AD

Verzeichnis der Mitteilungshefte

1 Röhnisch, Arthur: *Die Bemühungen um eine Wasserbauliche Versuchsanstalt an der Technischen Hochschule Stuttgart*, und
Fattah Abouleid, Abdel: *Beitrag zur Berechnung einer in lockeren Sand gerammten, zweifach verankerten Spundwand*, 1963

2 Marotz, Günter: *Beitrag zur Frage der Standfestigkeit von dichten Asphaltbelägen im Großwasserbau*, 1964

3 Gurr, Siegfried: *Beitrag zur Berechnung zusammengesetzter ebener Flächentragwerke unter besonderer Berücksichtigung ebener Stauwände, mit Hilfe von Randwert- und Lastwertmatrizen*, 1965

4 Plica, Peter: *Ein Beitrag zur Anwendung von Schalenkonstruktionen im Stahlwasserbau*, und Petrikat, Kurt: *Möglichkeiten und Grenzen des wasserbaulichen Versuchswesens*, 1966

5 Plate, Erich: *Beitrag zur Bestimmung der Windgeschwindigkeitsverteilung in der durch eine Wand gestörten bodennahen Luftschicht*,
und
Röhnisch, Arthur; Marotz, Günter: *Neue Baustoffe und Bauausführungen für den Schutz der Böschungen und der Sohle von Kanälen, Flüssen und Häfen; Gestehungskosten und jeweilige Vorteile*, sowie Unny, T.E.: *Schwingungsuntersuchungen am Kegelstrahlschieber*, 1967

6 Seiler, Erich: *Die Ermittlung des Anlagenwertes der bundeseigenen Binnenschiffahrtsstraßen und Talsperren und des Anteils der Binnenschiffahrt an diesem Wert*, 1967

7 *Sonderheft anläßlich des 65. Geburtstages von Prof. Arthur Röhnisch mit Beiträgen von* Benk, Dieter; Breitling, J.; Gurr, Siegfried; Haberhauer, Robert; Honekamp, Hermann; Kuz, Klaus Dieter; Marotz, Günter; Mayer-Vorfelder, Hans-Jörg; Miller, Rudolf; Plate, Erich J.; Radomski, Helge; Schwarz, Helmut; Vollmer, Ernst; Wildenhahn, Eberhard; 1967

8 Jumikis, Alfred: *Beitrag zur experimentellen Untersuchung des Wassernachschubs in einem gefrierenden Boden und die Beurteilung der Ergebnisse*, 1968

9 Marotz, Günter: *Technische Grundlagen einer Wasserspeicherung im natürlichen Untergrund*, 1968

10 Radomski, Helge: *Untersuchungen über den Einfluß der Querschnittsform wellenförmiger Spundwände auf die statischen und rammtechnischen Eigenschaften*, 1968

11 Schwarz, Helmut: *Die Grenztragfähigkeit des Baugrundes bei Einwirkung vertikal gezogener Ankerplatten als zweidimensionales Bruchproblem*, 1969

12 Erbel, Klaus: *Ein Beitrag zur Untersuchung der Metamorphose von Mittelgebirgsschneedecken unter besonderer Berücksichtigung eines Verfahrens zur Bestimmung der thermischen Schneequalität*, 1969

13 Westhaus, Karl-Heinz: *Der Strukturwandel in der Binnenschiffahrt und sein Einfluß auf den Ausbau der Binnenschiffskanäle*, 1969

14 Mayer-Vorfelder, Hans-Jörg: *Ein Beitrag zur Berechnung des Erdwiderstandes unter Ansatz der logarithmischen Spirale als Gleitflächenfunktion*, 1970

15 Schulz, Manfred: *Berechnung des räumlichen Erddruckes auf die Wandung kreiszylindrischer Körper*, 1970

16 Mobasseri, Manoutschehr: *Die Rippenstützmauer. Konstruktion und Grenzen ihrer Standsicherheit*, 1970

17 Benk, Dieter: *Ein Beitrag zum Betrieb und zur Bemessung von Hochwasserrückhaltebecken*, 1970

18 Gàl, Attila: *Bestimmung der mitschwingenden Wassermasse bei überströmten Fischbauchklappen mit kreiszylindrischem Staublech*, 1971, vergriffen

19 Kuz, Klaus Dieter: *Ein Beitrag zur Frage des Einsetzens von Kavitationserscheinungen in einer Düsenströmung bei Berücksichtigung der im Wasser gelösten Gase*, 1971, vergriffen

20 Schaak, Hartmut: *Verteilleitungen von Wasserkraftanlagen*, 1971

21 *Sonderheft zur Eröffnung der neuen Versuchsanstalt des Instituts für Wasserbau der Universität Stuttgart mit Beiträgen von* Brombach, Hansjörg; Dirksen, Wolfram; Gàl, Attila; Gerlach, Reinhard; Giesecke, Jürgen; Holthoff, Franz-Josef; Kuz, Klaus Dieter; Marotz, Günter; Minor, Hans-Erwin; Petrikat, Kurt; Röhnisch, Arthur; Rueff, Helge; Schwarz, Helmut; Vollmer, Ernst; Wildenhahn, Eberhard; 1972

22 Wang, Chung-su: *Ein Beitrag zur Berechnung der Schwingungen an Kegelstrahlschiebern*, 1972

23 Mayer-Vorfelder, Hans-Jörg: *Erdwiderstandsbeiwerte nach dem Ohde-Variationsverfahren*, 1972

24 Minor, Hans-Erwin: *Beitrag zur Bestimmung der Schwingungsanfachungsfunktionen überströmter Stauklappen*, 1972, vergriffen

25 Brombach, Hansjörg: *Untersuchung strömungsmechanischer Elemente (Fluidik) und die Möglichkeit der Anwendung von Wirbelkammerelementen im Wasserbau*, 1972, vergriffen

26 Wildenhahn, Eberhard: *Beitrag zur Berechnung von Horizontalfilterbrunnen*, 1972

27 Steinlein, Helmut: *Die Eliminierung der Schwebstoffe aus Flußwasser zum Zweck der unterirdischen Wasserspeicherung, gezeigt am Beispiel der Iller*, 1972

28 Holthoff, Franz Josef: *Die Überwindung großer Hubhöhen in der Binnenschiffahrt durch Schwimmerhebewerke*, 1973

29 Röder, Karl: *Einwirkungen aus Baugrundbewegungen auf trog- und kastenförmige Konstruktionen des Wasser- und Tunnelbaues*, 1973

30 Kretschmer, Heinz: *Die Bemessung von Bogenstaumauern in Abhängigkeit von der Talform*, 1973

31 Honekamp, Hermann: *Beitrag zur Berechnung der Montage von Unterwasserpipelines*, 1973

32 Giesecke, Jürgen: *Die Wirbelkammertriode als neuartiges Steuerorgan im Wasserbau*, und Brombach, Hansjörg: *Entwicklung, Bauformen, Wirkungsweise und Steuereigenschaften von Wirbelkammerverstärkern*, 1974

33 Rueff, Helge: *Untersuchung der schwingungserregenden Kräfte an zwei hintereinander angeordneten Tiefschützen unter besonderer Berücksichtigung von Kavitation*, 1974

34 Röhnisch, Arthur: *Einpreßversuche mit Zementmörtel für Spannbeton - Vergleich der Ergebnisse von Modellversuchen mit Ausführungen in Hüllwellrohren*, 1975

35 *Sonderheft anläßlich des 65. Geburtstages von Prof. Dr.-Ing. Kurt Petrikat mit Beiträgen von*: Brombach, Hansjörg; Erbel, Klaus; Flinspach, Dieter; Fischer jr., Richard; Gàl, Attila; Gerlach, Reinhard; Giesecke, Jürgen; Haberhauer, Robert; Hafner Edzard; Hausenblas, Bernhard; Horlacher, Hans-Burkhard; Hutarew, Andreas; Knoll, Manfred; Krummet, Ralph; Marotz, Günter; Merkle, Theodor; Miller, Christoph; Minor, Hans-Erwin; Neumayer, Hans; Rao, Syamala; Rath, Paul; Rueff, Helge; Ruppert, Jürgen; Schwarz, Wolfgang; Topal-Gökceli, Mehmet; Vollmer, Ernst; Wang, Chung-su; Weber, Hans-Georg; 1975

36 Berger, Jochum: *Beitrag zur Berechnung des Spannungszustandes in rotationssymmetrisch belasteten Kugelschalen veränderlicher Wandstärke unter Gas- und Flüssigkeitsdruck durch Integration schwach singulärer Differentialgleichungen*, 1975

37 Dirksen, Wolfram: *Berechnung instationärer Abflußvorgänge in gestauten Gerinnen mittels Differenzenverfahren und die Anwendung auf Hochwasserrückhaltebecken*, 1976

38 Horlacher, Hans-Burkhard: *Berechnung instationärer Temperatur- und Wärmespannungsfelder in langen mehrschichtigen Hohlzylindern*, 1976

39 Hafner, Edzard: *Untersuchung der hydrodynamischen Kräfte auf Baukörper im Tiefwasserbereich des Meeres*, 1977, ISBN 3-921694-39-6

40 Ruppert, Jürgen: *Über den Axialwirbelkammerverstärker für den Einsatz im Wasserbau*, 1977, ISBN 3-921694-40-X

41 Hutarew, Andreas: *Beitrag zur Beeinflußbarkeit des Sauerstoffgehalts in Fließgewässern an Abstürzen und Wehren*, 1977, ISBN 3-921694-41-8, vergriffen

42 Miller, Christoph: *Ein Beitrag zur Bestimmung der schwingungserregenden Kräfte an unterströmten Wehren*, 1977, ISBN 3-921694-42-6

43 Schwarz, Wolfgang: *Druckstoßberechnung unter Berücksichtigung der Radial- und Längsverschiebungen der Rohrwandung*, 1978, ISBN 3-921694-43-4

44 Kinzelbach, Wolfgang: *Numerische Untersuchungen über den optimalen Einsatz variabler Kühlsysteme einer Kraftwerkskette am Beispiel Oberrhein*, 1978, ISBN 3-921694-44-2

45 Barczewski, Baldur: *Neue Meßmethoden für Wasser-Luftgemische und deren Anwendung auf zweiphasige Auftriebsstrahlen*, 1979, ISBN 3-921694-45-0

46 Neumayer, Hans: *Untersuchung der Strömungsvorgänge in radialen Wirbelkammerverstärkern*, 1979, ISBN 3-921694-46-9

47 Elalfy, Youssef-Elhassan: *Untersuchung der Strömungsvorgänge in Wirbelkammerdioden und -drosseln*, 1979, ISBN 3-921694-47-7

48 Brombach, Hansjörg: *Automatisierung der Bewirtschaftung von Wasserspeichern*, 1981, ISBN 3-921694-48-5

49 Geldner, Peter: *Deterministische und stochastische Methoden zur Bestimmung der Selbstdichtung von Gewässern*, 1981, ISBN 3-921694-49-3, vergriffen

50 Mehlhorn, Hans: *Temperaturveränderungen im Grundwasser durch Brauchwassereinleitungen*, 1982, ISBN 3-921694-50-7, vergriffen

51 Hafner, Edzard: *Rohrleitungen und Behälter im Meer*, 1983, ISBN 3-921694-51-5

52 Rinnert, Bernd: *Hydrodynamische Dispersion in porösen Medien: Einfluß von Dichteunterschieden auf die Vertikalvermischung in horizontaler Strömung*, 1983, ISBN 3-921694-52-3, vergriffen

53 Lindner, Wulf: *Steuerung von Grundwasserentnahmen unter Einhaltung ökologischer Kriterien*, 1983, ISBN 3-921694-53-1, vergriffen

54 Herr, Michael; Herzer, Jörg; Kinzelbach, Wolfgang; Kobus, Helmut; Rinnert, Bernd: *Methoden zur rechnerischen Erfassung und hydraulischen Sanierung von Grundwasserkontaminationen*, 1983, ISBN 3-921694-54-X

55 Schmitt, Paul: *Wege zur Automatisierung der Niederschlagsermittlung*, 1984, ISBN 3-921694-55-8, vergriffen

56 Müller, Peter: *Transport und selektive Sedimentation von Schwebstoffen bei gestautem Abfluß*, 1985, ISBN 3-921694-56-6

57 El-Qawasmeh, Fuad: *Möglichkeiten und Grenzen der Tropfbewässerung unter besonderer Berücksichtigung der Verstopfungsanfälligkeit der Tropfelemente*, 1985, ISBN 3-921694-57-4, vergriffen

58 Kirchenbaur, Klaus: *Mikroprozessorgesteuerte Erfassung instationärer Druckfelder am Beispiel seegangsbelasteter Baukörper*, 1985, ISBN 3-921694-58-2

59 Kobus, Helmut (Hrsg.): *Modellierung des großräumigen Wärme- und Schadstofftransports im Grundwasser*, Tätigkeitsbericht 1984/85 (DFG-Forschergruppe an den Universitäten Hohenheim, Karlsruhe und Stuttgart), 1985, ISBN 3-921694-59-0, vergriffen

60 Spitz, Karlheinz: *Dispersion in porösen Medien: Einfluß von Inhomogenitäten und Dichteunterschieden*, 1985, ISBN 3-921694-60-4, vergriffen

61 Kobus, Helmut: *An Introduction to Air-Water Flows in Hydraulics*, 1985, ISBN 3-921694-61-2

62 Kaleris, Vassilios: *Erfassung des Austausches von Oberflächen- und Grundwasser in horizontalebenen Grundwassermodellen*, 1986, ISBN 3-921694-62-0

63 Herr, Michael: *Grundlagen der hydraulischen Sanierung verunreinigter Porengrundwasserleiter*, 1987, ISBN 3-921694-63-9

64 Marx, Walter: *Berechnung von Temperatur und Spannung in Massenbeton infolge Hydratation*, 1987, ISBN 3-921694-64-7

65 Koschitzky, Hans-Peter: *Dimensionierungskonzept für Sohlbelüfter in Schußrinnen zur Vermeidung von Kavitationsschäden*, 1987, ISBN 3-921694-65-5

66 Kobus, Helmut (Hrsg.): *Modellierung des großräumigen Wärme- und Schadstofftransports im Grundwasser*, Tätigkeitsbericht 1986/87 (DFG-Forschergruppe an den Universitäten Hohenheim, Karlsruhe und Stuttgart) 1987, ISBN 3-921694-66-3

67 Söll, Thomas: *Berechnungsverfahren zur Abschätzung anthropogener Temperaturanomalien im Grundwasser*, 1988, ISBN 3-921694-67-1

68 Dittrich, Andreas; Westrich, Bernd: *Bodenseeufererosion, Bestandsaufnahme und Bewertung*, 1988, ISBN 3-921694-68-X, vergriffen

69 Huwe, Bernd; van der Ploeg, Rienk R.: *Modelle zur Simulation des Stickstoffhaushaltes von Standorten mit unterschiedlicher landwirtschaftlicher Nutzung*, 1988, ISBN 3-921694-69-8, vergriffen

70 Stephan, Karl: *Integration elliptischer Funktionen*, 1988, ISBN 3-921694-70-1

71 Kobus, Helmut; Zilliox, Lothaire (Hrsg.): *Nitratbelastung des Grundwassers, Auswirkungen der Landwirtschaft auf die Grundwasser- und Rohwasserbeschaffenheit und Maßnahmen zum Schutz des Grundwassers*. Vorträge des deutsch-französischen Kolloquiums am 6. Oktober 1988, Universitäten Stuttgart und Louis Pasteur Strasbourg (Vorträge in deutsch oder französisch, Kurzfassungen zweisprachig), 1988, ISBN 3-921694-71-X

72 Soyeaux, Renald: *Unterströmung von Stauanlagen auf klüftigem Untergrund unter Berücksichtigung laminarer und turbulenter Fließzustände*,1991, ISBN 3-921694-72-8

73 Kohane, Roberto: *Berechnungsmethoden für Hochwasserabfluß in Fließgewässern mit überströmten Vorländern*, 1991, ISBN 3-921694-73-6

74 Hassinger, Reinhard: *Beitrag zur Hydraulik und Bemessung von Blocksteinrampen in flexibler Bauweise*, 1991, ISBN 3-921694-74-4, vergriffen

75 Schäfer, Gerhard: *Einfluß von Schichtenstrukturen und lokalen Einlagerungen auf die Längsdispersion in Porengrundwasserleitern*, 1991, ISBN 3-921694-75-2

76 Giesecke, Jürgen: *Vorträge, Wasserwirtschaft in stark besiedelten Regionen; Umweltforschung mit Schwerpunkt Wasserwirtschaft*, 1991, ISBN 3-921694-76-0

77 Huwe, Bernd: *Deterministische und stochastische Ansätze zur Modellierung des Stickstoffhaushalts landwirtschaftlich genutzter Flächen auf unterschiedlichem Skalenniveau*, 1992, ISBN 3-921694-77-9, vergriffen

78 Rommel, Michael: *Verwendung von Kluftdaten zur realitätsnahen Generierung von Kluftnetzen mit anschließender laminar-turbulenter Strömungsberechnung*, 1993, ISBN 3-92 1694-78-7

79 Marschall, Paul: *Die Ermittlung lokaler Stofffrachten im Grundwasser mit Hilfe von Einbohrloch-Meßverfahren*, 1993, ISBN 3-921694-79-5, vergriffen

80 Ptak, Thomas: *Stofftransport in heterogenen Porenaquiferen: Felduntersuchungen und stochastische Modellierung*, 1993, ISBN 3-921694-80-9, vergriffen

81 Haakh, Frieder: *Transientes Strömungsverhalten in Wirbelkammern,* 1993, ISBN 3-921694-81-7

82 Kobus, Helmut; Cirpka, Olaf; Barczewski, Baldur; Koschitzky, Hans-Peter: *Versucheinrichtung zur Grundwasser und Altlastensanierung VEGAS, Konzeption und Programmrahmen*, 1993, ISBN 3-921694-82-5

83 Zang, Weidong: *Optimaler Echtzeit-Betrieb eines Speichers mit aktueller Abflußregenerierung*, 1994, ISBN 3-921694-83-3, vergriffen

84 Franke, Hans-Jörg: *Stochastische Modellierung eines flächenhaften Stoffeintrages und Transports in Grundwasser am Beispiel der Pflanzenschutzmittelproblematik*, 1995, ISBN 3-921694-84-1

85 Lang, Ulrich: *Simulation regionaler Strömungs- und Transportvorgänge in Karstaquiferen mit Hilfe des Doppelkontinuum-Ansatzes: Methodenentwicklung und Parameteridentifikation*, 1995, ISBN 3-921694-85-X, vergriffen

86 Helmig, Rainer: *Einführung in die Numerischen Methoden der Hydromechanik*, 1996, ISBN 3-921694-86-8, vergriffen

87 Cirpka, Olaf: *CONTRACT: A Numerical Tool for Contaminant Transport and Chemical Transformations - Theory and Program Documentation* -, 1996, ISBN 3-921694-87-6

88 Haberlandt, Uwe: *Stochastische Synthese und Regionalisierung des Niederschlages für Schmutzfrachtberechnungen*, 1996, ISBN 3-921694-88-4

89 Croisé, Jean: *Extraktion von flüchtigen Chemikalien aus natürlichen Lockergesteinen mittels erzwungener Luftströmung*, 1996, ISBN 3-921694-89-2, vergriffen

90 Jorde, Klaus: *Ökologisch begründete, dynamische Mindestwasserregelungen bei Ausleitungskraftwerken*, 1997, ISBN 3-921694-90-6, vergriffen

91 Helmig, Rainer: *Gekoppelte Strömungs- und Transportprozesse im Untergrund - Ein Beitrag zur Hydrosystemmodellierung*-, 1998, ISBN 3-921694-91-4, vergriffen

92 Emmert, Martin: *Numerische Modellierung nichtisothermer Gas-Wasser Systeme in porösen Medien,* 1997, ISBN 3-921694-92-2

93 Kern, Ulrich: *Transport von Schweb- und Schadstoffen in staugeregelten Fließgewässern am Beispiel des Neckars*, 1997, ISBN 3-921694-93-0, vergriffen

94 Förster, Georg: *Druckstoßdämpfung durch große Luftblasen in Hochpunkten von Rohrleitungen 1997*, ISBN 3-921694-94-9

95 Cirpka, Olaf: *Numerische Methoden zur Simulation des reaktiven Mehrkomponententransports im Grundwasser*, 1997, ISBN 3-921694-95-7, vergriffen

96 Färber, Arne: *Wärmetransport in der ungesättigten Bodenzone: Entwicklung einer thermischen In-situ-Sanierungstechnologie*, 1997, ISBN 3-921694-96-5

97 Betz, Christoph: *Wasserdampfdestillation von Schadstoffen im porösen Medium: Entwicklung einer thermischen In-situ-Sanierungstechnologie*, 1998, ISBN 3-921694-97-3

98 Xu, Yichun: *Numerical Modeling of Suspended Sediment Transport in Rivers*, 1998, ISBN 3-921694-98-1, vergriffen

99 Wüst, Wolfgang: *Geochemische Untersuchungen zur Sanierung CKW-kontaminierter Aquifere mit Fe(0)-Reaktionswänden,* 2000, ISBN 3-933761-02-2

100 Sheta, Hussam: *Simulation von Mehrphasenvorgängen in porösen Medien unter Einbeziehung von Hysterese-Effekten*, 2000, ISBN 3-933761-03-4

101 Ayros, Edwin: *Regionalisierung extremer Abflüsse auf der Grundlage statistischer Verfahren*, 2000, ISBN 3-933761-04-2, vergriffen

102 Huber, Ralf: *Compositional Multiphase Flow and Transport in Heterogeneous Porous Media*, 2000, ISBN 3-933761-05-0

103 Braun, Christopherus: *Ein Upscaling-Verfahren für Mehrphasenströmungen in porösen Medien*, 2000, ISBN 3-933761-06-9

104 Hofmann, Bernd: *Entwicklung eines rechnergestützten Managementsystems zur Beurteilung von Grundwasserschadensfällen*, 2000, ISBN 3-933761-07-7

105 Class, Holger: *Theorie und numerische Modellierung nichtisothermer Mehrphasenprozesse in NAPL-kontaminierten porösen Medien,* 2001, ISBN 3-933761-08-5

106 Schmidt, Reinhard: *Wasserdampf- und Heißluftinjektion zur thermischen Sanierung kontaminierter Standorte*, 2001, ISBN 3-933761-09-3

107 Josef, Reinhold:, *Schadstoffextraktion mit hydraulischen Sanierungsverfahren unter Anwendung von grenzflächenaktiven Stoffen*, 2001, ISBN 3-933761-10-7

108 Schneider, Matthias: *Habitat- und Abflussmodellierung für Fließgewässer mit unscharfen Berechnungsansätzen*, 2001, ISBN 3-933761-11-5

109 Rathgeb, Andreas: *Hydrodynamische Bemessungsgrundlagen für Lockerdeckwerke an überströmbaren Erddämmen*, 2001, ISBN 3-933761-12-3

110 Lang, Stefan: *Parallele numerische Simulation instätionärer Probleme mit adaptiven Methoden auf unstrukturierten Gittern*, 2001, ISBN 3-933761-13-1

111 Appt, Jochen; Stumpp Simone: *Die Bodensee-Messkampagne 2001, IWS/CWR Lake Constance Measurement Program 2001*, 2002, ISBN 3-933761-14-X

112 Heimerl, Stephan: *Systematische Beurteilung von Wasserkraftprojekten,* 2002, ISBN 3-933761-15-8, vergriffen

113 Iqbal, Amin: *On the Management and Salinity Control of Drip Irrigation,* 2002, ISBN 3-933761-16-6

114 Silberhorn-Hemminger, Annette: *Modellierung von Kluftaquifersystemen: Geostatistische Analyse und deterministisch-stochastische Kluftgenerierung,* 2002, ISBN 3-933761-17-4

115 Winkler, Angela: *Prozesse des Wärme- und Stofftransports bei der In-situ-Sanierung mit festen Wärmequellen,* 2003, ISBN 3-933761-18-2

116 Marx, Walter: *Wasserkraft, Bewässerung, Umwelt - Planungs- und Bewertungsschwerpunkte der Wasserbewirtschaftung,* 2003, ISBN 3-933761-19-0

117 Hinkelmann, Reinhard: *Efficient Numerical Methods and Information-Processing Techniques in Environment Water,* 2003, ISBN 3-933761-20-4

118 Samaniego-Eguiguren, Luis Eduardo: *Hydrological Consequences of Land Use / Land Cover and Climatic Changes in Mesoscale Catchments*, 2003, ISBN 3-933761-21-2

119 Neunhäuserer, Lina: *Diskretisierungsansätze zur Modellierung von Strömungs- und Transportprozessen in geklüftet-porösen Medien*, 2003, ISBN 3-933761-22-0

120 Paul, Maren: *Simulation of Two-Phase Flow in Heterogeneous Poros Media with Adaptive Methods*, 2003, ISBN 3-933761-23-9

121 Ehret, Uwe: *Rainfall and Flood Nowcasting in Small Catchments using Weather Radar*, 2003, ISBN 3-933761-24-7

122 Haag, Ingo: *Der Sauerstoffhaushalt staugeregelter Flüsse am Beispiel des Neckars - Analysen, Experimente, Simulationen -,* 2003, ISBN 3-933761-25-5

123 Appt, Jochen: *Analysis of Basin-Scale Internal Waves in Upper Lake Constance,* 2003, ISBN 3-933761-26-3

124 Hrsg.: Schrenk, Volker; Batereau, Katrin; Barczewski, Baldur; Weber, Karolin und Koschitzky, Hans-Peter: *Symposium Ressource Fläche und VEGAS - Statuskolloquium 2003, 30. September und 1. Oktober 2003,* 2003, ISBN 3-933761-27-1

125 Omar Khalil Ouda: *Optimisation of Agricultural Water Use: A Decision Support System for the Gaza Strip,* 2003, ISBN 3-933761-28-0

126 Batereau, Katrin: *Sensorbasierte Bodenluftmessung zur Vor-Ort-Erkundung von Schadensherden im Untergrund*, 2004, ISBN 3-933761-29-8

127 Witt, Oliver: *Erosionsstabilität von Gewässersedimenten mit Auswirkung auf den Stofftransport bei Hochwasser am Beispiel ausgewählter Stauhaltungen des Oberrheins*, 2004, ISBN 3-933761-30-1

128 Jakobs, Hartmut: *Simulation nicht-isothermer Gas-Wasser-Prozesse in komplexen Kluft-Matrix-Systemen*, 2004, ISBN 3-933761-31-X

129 Li, Chen-Chien: *Deterministisch-stochastisches Berechnungskonzept zur Beurteilung der Auswirkungen erosiver Hochwasserereignisse in Flussstauhaltungen,* 2004, ISBN 3-933761-32-8

130 Reichenberger, Volker; Helmig, Rainer; Jakobs, Hartmut; Bastian, Peter; Niessner, Jennifer: *Complex Gas-Water Processes in Discrete Fracture-Matrix Systems: Upscaling, Mass-Conservative Discretization and Efficient Multilevel Solution,* 2004, ISBN 3-933761-33-6

131 Hrsg.: Barczewski, Baldur; Koschitzky, Hans-Peter; Weber, Karolin; Wege, Ralf: *VEGAS - Statuskolloquium 2004,* Tagungsband zur Veranstaltung am 05. Oktober 2004 an der Universität Stuttgart, Campus Stuttgart-Vaihingen, 2004, ISBN 3-933761-34-4

132 Asie, Kemal Jabir: *Finite Volume Models for Multiphase Multicomponent Flow through Porous Media*. 2005, ISBN 3-933761-35-2

133 Jacoub, George: *Development of a 2-D Numerical Module for Particulate Contaminant Transport in Flood Retention Reservoirs and Impounded Rivers,* 2004, ISBN 3-933761-36-0

134 Nowak, Wolfgang: *Geostatistical Methods for the Identification of Flow and Transport Parameters in the Subsurface,* 2005, ISBN 3-933761-37-9

135 Süß, Mia: *Analysis of the influence of structures and boundaries on flow and transport processes in fractured porous media*, 2005, ISBN 3-933761-38-7

136 Jose, Surabhin Chackiath: *Experimental Investigations on Longitudinal Dispersive Mixing in Heterogeneous Aquifers,* 2005, ISBN: 3-933761-39-5

137 Filiz, Fulya: *Linking Large-Scale Meteorological Conditions to Floods in Mesoscale Catchments,* 2005, ISBN 3-933761-40-9

138 Qin, Minghao: *Wirklichkeitsnahe und recheneffiziente Ermittlung von Temperatur und Spannungen bei großen RCC-Staumauern*, 2005, ISBN 3-933761-41-7

139 Kobayashi, Kenichiro: *Optimization Methods for Multiphase Systems in the Subsurface - Application to Methane Migration in Coal Mining Areas*, 2005, ISBN 3-933761-42-5

140 Rahman, Md. Arifur: *Experimental Investigations on Transverse Dispersive Mixing in Heterogeneous Porous Media,* 2005, ISBN 3-933761-43-3

141 Schrenk, Volker: *Ökobilanzen zur Bewertung von Altlastensanierungsmaßnahmen,* 2005, ISBN 3-933761-44-1

142 Hundecha, Hirpa Yeshewatesfa: *Regionalization of Parameters of a Conceptual Rainfall-Runoff Model*, 2005, ISBN: 3-933761-45-X

143 Wege, Ralf: *Untersuchungs- und Überwachungsmethoden für die Beurteilung natürlicher Selbstreinigungsprozesse im Grundwasser,* 2005, ISBN 3-933761-46-8

144 Breiting, Thomas: *Techniken und Methoden der Hydroinformatik - Modellierung von komplexen Hydrosystemen im Untergrund*, 2006, 3-933761-47-6

145 Hrsg.: Braun, Jürgen; Koschitzky, Hans-Peter; Müller, Martin: *Ressource Untergrund: 10 Jahre VEGAS: Forschung und Technologieentwicklung zum Schutz von Grundwasser und Boden,* Tagungsband zur Veranstaltung am 28. und 29. September 2005 an der Universität Stuttgart, Campus Stuttgart-Vaihingen, 2005, ISBN 3-933761-48-4

146 Rojanschi, Vlad: *Abflusskonzentration in mesoskaligen Einzugsgebieten unter Berücksichtigung des Sickerraumes,* 2006, ISBN 3-933761-49-2

147 Winkler, Nina Simone: *Optimierung der Steuerung von Hochwasserrückhaltebecken-systemen,* 2006, ISBN 3-933761-50-6

148 Wolf, Jens: *Räumlich differenzierte Modellierung der Grundwasserströmung alluvialer Aquifere für mesoskalige Einzugsgebiete*, 2006, ISBN: 3-933761-51-4

149 Kohler, Beate: *Externe Effekte der Laufwasserkraftnutzung*, 2006, ISBN 3-933761-52-2

150 Hrsg.: Braun, Jürgen; Koschitzky, Hans-Peter; Stuhrmann, Matthias: *VEGAS-Statuskolloquium 2006,* Tagungsband zur Veranstaltung am 28. September 2006 an der Universität Stuttgart, Campus Stuttgart-Vaihingen, 2006, ISBN 3-933761-53-0

151 Niessner, Jennifer: *Multi-Scale Modeling of Multi-Phase - Multi-Component Processes in Heterogeneous Porous Media*, 2006, ISBN 3-933761-54-9

152 Fischer, Markus: *Beanspruchung eingeerdeter Rohrleitungen infolge Austrocknung bindiger Böden,* 2006, ISBN 3-933761-55-7

153 Schneck, Alexander: *Optimierung der Grundwasserbewirtschaftung unter Berücksichtigung der Belange der Wasserversorgung, der Landwirtschaft und des Naturschutzes*, 2006, ISBN 3-933761-56-5

154 Das, Tapash: *The Impact of Spatial Variability of Precipitation on the Predictive Uncertainty of Hydrological Models,* 2006, ISBN 3-933761-57-3

155 Bielinski, Andreas: *Numerical Simulation of CO_2 sequestration in geological formations*, 2007, ISBN 3-933761-58-1

156 Mödinger, Jens: *Entwicklung eines Bewertungs- und Entscheidungsunterstützungssystems für eine nachhaltige regionale Grundwasserbewirtschaftung*, 2006, ISBN 3-933761-60-3

157 Manthey, Sabine: *Two-phase flow processes with dynamic effects in porous media - parameter estimation and simulation,* 2007, ISBN 3-933761-61-1

158 Pozos Estrada, Oscar: *Investigation on the Effects of Entrained Air in Pipelines,* 2007, ISBN 3-933761-62-X

159 Ochs, Steffen Oliver: *Steam injection into saturated porous media – process analysis including experimental and numerical investigations*, 2007, ISBN 3-933761-63-8

160 Marx, Andreas: *Einsatz gekoppelter Modelle und Wetterradar zur Abschätzung von Niederschlagsintensitäten und zur Abflussvorhersage, 2007,* ISBN 3-933761-64-6

161 Hartmann, Gabriele Maria: *Investigation of Evapotranspiration Concepts in Hydrological Modelling for Climate Change Impact Assessment*, 2007, ISBN 3-933761-65-4

162 Kebede Gurmessa, Tesfaye: *Numerical Investigation on Flow and Transport Characteristics to Improve Long-Term Simulation of Reservoir Sedimentation*, 2007, ISBN 3-933761-66-2

163 Trifković, Aleksandar: *Multi-objective and Risk-based Modelling Methodology for Planning, Design and Operation of Water Supply Systems*, 2007, ISBN 3-933761-67-0

164 Götzinger, Jens: *Distributed Conceptual Hydrological Modelling - Simulation of Climate, Land Use Change Impact and Uncertainty Analysis*, 2007, ISBN 3-933761-68-9

165 Hrsg.: Braun, Jürgen; Koschitzky, Hans-Peter; Stuhrmann, Matthias: *VEGAS – Kolloquium 2007,* Tagungsband zur Veranstaltung am 26. September 2007 an der Universität Stuttgart, Campus Stuttgart-Vaihingen, 2007, ISBN 3-933761-69-7

166 Freeman, Beau: *Modernization Criteria Assessment for Water Resources Planning; Klamath Irrigation Project, U.S.*, 2008, ISBN 3-933761-70-0

167 Dreher, Thomas: *Selektive Sedimentation von Feinstschwebstoffen in Wechselwirkung mit wandnahen turbulenten Strömungsbedingungen*, 2008, ISBN 3-933761-71-9

168 Yang, Wei: *Discrete-Continuous Downscaling Model for Generating Daily Precipitation Time Series*, 2008, ISBN 3-933761-72-7

169 Kopecki, Ianina: *Calculational Approach to FST-Hemispheres for Multiparametrical Benthos Habitat Modelling,* 2008*,* ISBN 3-933761-73-5

170 Brommundt, Jürgen: *Stochastische Generierung räumlich zusammenhängender Niederschlagszeitreihen*, 2008, ISBN 3-933761-74-3

171 Papafotiou, *Alexandros: Numerical Investigations of the Role of Hysteresis in Heterogeneous Two-Phase Flow Systems*, 2008, ISBN 3-933761-75-1

172 He, Yi: *Application of a Non-Parametric Classification Scheme to Catchment Hydrology*, 2008, ISBN 978-3-933761-76-7

173 Wagner, Sven: *Water Balance in a Poorly Gauged Basin in West Africa Using Atmospheric Modelling and Remote Sensing Information*, 2008, ISBN 978-3-933761-77-4

174 Hrsg.: Braun, Jürgen; Koschitzky, Hans-Peter; Stuhrmann, Matthias; Schrenk, Volker: *VEGAS-Kolloquium 2008 Ressource Fläche III*, Tagungsband zur Veranstaltung am 01. Oktober 2008 an der Universität Stuttgart, Campus Stuttgart-Vaihingen, 2008, ISBN 978-3-933761-78-1

175 Patil, Sachin: *Regionalization of an Event Based Nash Cascade Model for Flood Predictions in Ungauged Basins*, 2008, ISBN 978-3-933761-79-8

176 Assteerawatt, Anongnart: *Flow and Transport Modelling of Fractured Aquifers based on a Geostatistical Approach,* 2008, ISBN 978-3-933761-80-4

177 Karnahl, Joachim Alexander: *2D numerische Modellierung von multifraktionalem Schwebstoff- und Schadstofftransport in Flüssen*, 2008, ISBN 978-3-933761-81-1

178 Hiester, Uwe: *Technologieentwicklung zur In-situ-Sanierung der ungesättigten Bodenzone mit festen Wärmequellen,* 2009, ISBN 978-3-933761-82-8

179 Laux, Patrick: *Statistical Modeling of Precipitation for Agricultural Planning in the Volta Basin of West Africa,* 2009, ISBN 978-3-933761-83-5

180 Ehsan, Saqib: *Evaluation of Life Safety Risks Related to Severe Flooding,* 2009, ISBN 978-3-933761-84-2

181 Prohaska, Sandra: *Development and Application of a 1D Multi-Strip Fine Sediment Transport Model for Regulated Rivers,* 2009, ISBN 978-3-933761-85-9

182 Kopp, Andreas: *Evaluation of CO_2 Injection Processes in Geological Formations for Site Screening,* 2009, ISBN 978-3-933761-86-6

183 Ebigbo, Anozie: *Modelling of biofilm growth and its influence on CO_2 and water (two-phase) flow in porous media,* 2009, ISBN 978-3-933761-87-3

184 Freiboth, Sandra: *A phenomenological model for the numerical simulation of multiphase multicomponent processes considering structural alterations of porous media*, 2009, ISBN 978-3-933761-88-0

185 Zöllner, Frank: *Implementierung und Anwendung netzfreier Methoden im Konstruktiven Wasserbau und in der Hydromechanik*, 2009, ISBN 978-3-933761-89-7

186 Vasin, Milos: *Influence of the soil structure and property contrast on flow and transport in the unsaturated zone*, 2010, ISBN 978-3-933761-90-3

187 Li, Jing: *Application of Copulas as a New Geostatistical Tool*, 2010, ISBN 978-3-933761-91-0

188 AghaKouchak, Amir: *Simulation of Remotely Sensed Rainfall Fields Using Copulas*, 2010, ISBN 978-3-933761-92-7

189 Thapa, Pawan Kumar: *Physically-based spatially distributed rainfall runoff modelling for soil erosion estimation*, 2010, ISBN 978-3-933761-93-4

190 Wurms, Sven: *Numerische Modellierung der Sedimentationsprozesse in Retentionsanlagen zur Steuerung von Stoffströmen bei extremen Hochwasserabflussereignissen*, 2011, ISBN 978-3-933761-94-1

191 Merkel, Uwe: *Unsicherheitsanalyse hydraulischer Einwirkungen auf Hochwasserschutzdeiche und Steigerung der Leistungsfähigkeit durch adaptive Strömungsmodellierung*, 2011, ISBN 978-3-933761-95-8

192 Fritz, Jochen: *A Decoupled Model for Compositional Non-Isothermal Multiphase Flow in Porous Media and Multiphysics Approaches for Two-Phase Flow*, 2010, ISBN 978-3-933761-96-5

193 Weber, Karolin (Hrsg.): *12. Treffen junger WissenschaftlerInnen an Wasserbauinstituten*, 2010, ISBN 978-3-933761-97-2

194 Bliefernicht, Jan-Geert: *Probability Forecasts of Daily Areal Precipitation for Small River Basins,* 2011, ISBN 978-3-933761-98-9

195 Hrsg.: Koschitzky, Hans-Peter; Braun, Jürgen: *VEGAS-Kolloquium 2010 In-situ-Sanierung - Stand und Entwicklung Nano und ISCO -,* Tagungsband zur Veranstaltung am 07. Oktober 2010 an der Universität Stuttgart, Campus Stuttgart-Vaihingen*,* 2010*,* ISBN 978-3-933761-99-6

196 Gafurov, Abror: *Water Balance Modeling Using Remote Sensing Information - Focus on Central Asia,* 2010, ISBN 978-3-942036-00-9

197 Mackenberg, Sylvia: *Die Quellstärke in der Sickerwasserprognose: Möglichkeiten und Grenzen von Labor- und Freilanduntersuchungen,* 2010, ISBN 978-3-942036-01-6

198 Singh, Shailesh Kumar: *Robust Parameter Estimation in Gauged and Ungauged Basins,* 2010, ISBN 978-3-942036-02-3

199 Doğan, Mehmet Onur: *Coupling of porous media flow with pipe flow,* 2011, ISBN 978-3-942036-03-0

200 Liu, Min: *Study of Topographic Effects on Hydrological Patterns and the Implication on Hydrological Modeling and Data Interpolation,* 2011, ISBN 978-3-942036-04-7

201 Geleta, Habtamu Itefa: *Watershed Sediment Yield Modeling for Data Scarce Areas,* 2011, ISBN 978-3-942036-05-4

202 Franke, Jörg: *Einfluss der Überwachung auf die Versagenswahrscheinlichkeit von Staustufen,* 2011, ISBN 978-3-942036-06-1

203 Bakimchandra, Oinam: *Integrated Fuzzy-GIS approach for assessing regional soil erosion risks,* 2011, ISBN 978-3-942036-07-8

204 Alam, Muhammad Mahboob: *Statistical Downscaling of Extremes of Precipitation in Mesoscale Catchments from Different RCMs and Their Effects on Local Hydrology,* 2011, ISBN 978-3-942036-08-5

205 Hrsg.: Koschitzky, Hans-Peter; Braun, Jürgen: *VEGAS-Kolloquium 2011 Flache Geothermie - Perspektiven und Risiken,* Tagungsband zur Veranstaltung am 06. Oktober 2011 an der Universität Stuttgart, Campus Stuttgart-Vaihingen, 2011, ISBN 978-3-933761-09-2

206 Haslauer, Claus: *Analysis of Real-World Spatial Dependence of Subsurface Hydraulic Properties Using Copulas with a Focus on Solute Transport Behaviour,* 2011, ISBN 978-3-942036-10-8

207 Dung, Nguyen Viet: *Multi-objective automatic calibration of hydrodynamic models – development of the concept and an application in the Mekong Delta,* 2011, ISBN 978-3-942036-11-5

208 Hung, Nguyen Nghia: *Sediment dynamics in the floodplain of the Mekong Delta, Vietnam,* 2011, ISBN 978-3-942036-12-2

209 Kuhlmann, Anna: *Influence of soil structure and root water uptake on flow in the unsaturated zone,* 2012, ISBN 978-3-942036-13-9

210 Tuhtan, Jeffrey Andrew: *Including the Second Law Inequality in Aquatic Ecodynamics: A Modeling Approach for Alpine Rivers Impacted by Hydropeaking,* 2012, ISBN 978-3-942036-14-6

211 Tolossa, Habtamu: *Sediment Transport Computation Using a Data-Driven Adaptive Neuro-Fuzzy Modelling Approach,* 2012, ISBN 978-3-942036-15-3

212 Tatomir, Alexandru-Bodgan: *From Discrete to Continuum Concepts of Flow in Fractured Porous Media,* 2012, ISBN 978-3-942036-16-0

213 Erbertseder, Karin: *A Multi-Scale Model for Describing Cancer-Therapeutic Transport in the Human Lung,* 2012, ISBN 978-3-942036-17-7

214 Noack, Markus: *Modelling Approach for Interstitial Sediment Dynamics and Reproduction of Gravel Spawning Fish,* 2012, ISBN 978-3-942036-18-4

215 De Boer, Cjestmir Volkert: *Transport of Nano Sized Zero Valent Iron Colloids during Injection into the Subsurface*, 2012, ISBN 978-3-942036-19-1

216 Pfaff, Thomas: *Processing and Analysis of Weather Radar Data for Use in Hydrology*, 2013, ISBN 978-3-942036-20-7

217 Lebrenz, Hans-Henning: *Addressing the Input Uncertainty for Hydrological Modeling by a New Geostatistical Method*, 2013, ISBN 978-3-942036-21-4

218 Darcis, Melanie Yvonne: *Coupling Models of Different Complexity for the Simulation of CO_2 Storage in Deep Saline Aquifers*, 2013, ISBN 978-3-942036-22-1

219 Beck, Ferdinand: *Generation of Spatially Correlated Synthetic Rainfall Time Series in High Temporal Resolution - A Data Driven Approach*, 2013, ISBN 978-3-942036-23-8

220 Guthke, Philipp: *Non-multi-Gaussian spatial structures: Process-driven natural genesis, manifestation, modeling approaches, and influences on dependent processes*, 2013, ISBN 978-3-942036-24-5

221 Walter, Lena: *Uncertainty studies and risk assessment for CO_2 storage in geological formations*, 2013, ISBN 978-3-942036-25-2

222 Wolff, Markus: *Multi-scale modeling of two-phase flow in porous media including capillary pressure effects,* 2013, ISBN 978-3-942036-26-9

223 Mosthaf, Klaus Roland: *Modeling and analysis of coupled porous-medium and free flow with application to evaporation processes,* 2014, ISBN 978-3-942036-27-6

224 Leube, Philipp Christoph: *Methods for Physically-Based Model Reduction in Time: Analysis, Comparison of Methods and Application*, 2013, ISBN 978-3-942036-28-3

225 Rodríguez Fernández, Jhan Ignacio: *High Order Interactions among environmental variables: Diagnostics and initial steps towards modeling*, 2013, ISBN 978-3-942036-29-0

226 Eder, Maria Magdalena: *Climate Sensitivity of a Large Lake*, 2013, ISBN 978-3-942036-30-6

227 Greiner, Philipp: *Alkoholinjektion zur In-situ-Sanierung von CKW Schadensherden in Grundwasserleitern: Charakterisierung der relevanten Prozesse auf unterschiedlichen Skalen*, 2014, ISBN 978-3-942036-31-3

228 Lauser, Andreas: *Theory and Numerical Applications of Compositional Multi-Phase Flow in Porous Media*, 2014, ISBN 978-3-942036-32-0

229 Enzenhöfer, Rainer: *Risk Quantification and Management in Water Production and Supply Systems*, 2014, ISBN 978-3-942036-33-7

230 Faigle, Benjamin: *Adaptive modelling of compositional multi-phase flow with capillary pressure*, 2014, ISBN 978-3-942036-34-4

231 Oladyshkin, Sergey: *Efficient modeling of environmental systems in the face of complexity and uncertainty*, 2014, ISBN 978-3-942036-35-1

232 Sugimoto, Takayuki: *Copula based Stochastic Analysis of Discharge Time Series*, 2014, ISBN 978-3-942036-36-8

233 Koch, Jonas: *Simulation, Identification and Characterization of Contaminant Source Architectures in the Subsurface*, 2014, ISBN 978-3-942036-37-5

234 Zhang, Jin: *Investigations on Urban River Regulation and Ecological Rehabilitation Measures, Case of Shenzhen in China*, 2014, ISBN 978-3-942036-38-2

235 Siebel, Rüdiger: *Experimentelle Untersuchungen zur hydrodynamischen Belastung und Standsicherheit von Deckwerken an überströmbaren Erddämmen,* 2014, ISBN 978-3-942036-39-9

236 Baber, Katherina: *Coupling free flow and flow in porous media in biological and technical applications: From a simple to a complex interface description,* 2014, ISBN 978-3-942036-40-5

237 Nuske, Klaus Philipp: *Beyond Local Equilibrium — Relaxing local equilibrium assumptions in multiphase flow in porous media,* 2014, ISBN 978-3-942036-41-2

238 Geiges, Andreas: *Efficient concepts for optimal experimental design in nonlinear environmental systems*, 2014, ISBN 978-3-942036-42-9

239 Schwenck, Nicolas: *An XFEM-Based Model for Fluid Flow in Fractured Porous Media*, 2014, ISBN 978-3-942036-43-6

Die Mitteilungshefte ab der Nr. 134 (Jg. 2005) stehen als pdf-Datei über die Homepage des Instituts: www.iws.uni-stuttgart.de zur Verfügung.